DISSERTATION

Anomalous temperature effects in superlattices and novel material systems for quantum cascade detectors

ausgeführt zum Zwecke der Erlangung des akademischen Grades eines Doktors der technischen Wissenschaften

unter der Leitung von

Assoc.-Prof. Aaron Maxwell Andrews, PhD
Institut für Festkörperelektronik

eingereicht an der

TECHNISCHEN UNIVERSITÄT WIEN
FAKULTÄT FÜR ELEKTROTECHNIK UND INFORMATIONSTECHNIK

von

Dipl.-Ing. Miriam Giparakis, BSc

Mat.Nr. 01227015

Wien, im September 2023

Betreuer: Assoc.-Prof. Aaron Maxwell Andrews, PhD

Zweitbetreuer: Prof. Dr. Gottfried Strasser

1. Gutachter: Prof. Dr. Alexander Bergmann

2. Gutachter: Prof. Jean-Michel Chauveau, PhD

Tag der mündlichen Prüfung: 25. Oktober 2023

""Since we cannot change reality, let us change the eyes which see reality," says one of my favorite Byzantine mystics. I did this when a child; I do it now as well in the most creative moments of my life." — Nikos Kazantzakis, Report to Greco

Abstract

Molecular beam epitaxy (MBE) is a versatile tool that allows both fundamental research at universities and the production of devices by industry. In the present thesis, zinc-blende III-V semiconductors are grown with MBE, where the emphasis lies in mid-infrared (MIR) to THz optoelectronics, centered on the growth related to THz quantum cascade lasers (QCLs) and short- to mid-infrared quantum cascade detectors (QCDs). Devices in this spectral region find applications in spectroscopy, telecommunication, and imaging.

This thesis encompasses the design, growth, analysis, fabrication, and optical characterization of QCDs expanded to the promising InAs/Al(As)Sb material system grown on InAs or GaSb substrates. This material system offers beneficial intrinsic properties like one of the lowest effective electron masses, which increases the optical absorption strength, and one of the highest conduction band offsets (CBOs), allowing for transition energies up to wavelengths in the near-infrared. To grow InAs/Al(As)Sb, growth parameters, like group-V fluxes, oxide removal, or growth temperatures are optimized. To minimize unwanted group-V intermixing or As-for-Sb exchange, shutter sequences are implemented that result in sharp interfaces. QCDs with absorption wavelengths ranging from 2.7–5.5 μm are designed, grown, fabricated, and characterized. Thus, demonstrating the material systems' wide wavelength range and, in this process, increasing the maturity of InAs/Al(As)Sb QCDs. In particular, a top-side illuminated (surface normal) InAs/AlAs$_{0.16}$Sb$_{0.84}$ QCD, grown lattice matched to InAs, is produced and realized with a diffraction grating. The absorption wavelength of 2.7 μm lies in the center of a CO_2 absorption line and corresponds to energies above the bandgap energy of InAs. On GaSb substrates, InAs/AlSb QCDs are grown strain-balanced with an InAs:AlSb ratio three times higher than the ratio required for strain-compensated growth. This is achieved by including sub-monolayer InSb layers and is a necessary measure for regaining the freedom lattice-matched materials have in optimizing the design.

Due to the type-II band alignment of the InAs/Al(As)Sb material system, the effective bandgap for interband transitions reduces to the near-infrared region resulting in the observation of strong broadband interband signals from 1.2–3 μm, which lie directly next to the QCD signal. Preliminary measurements resulted in an interesting bias dependency of the interband signal.

MBE also enables research on material and structural properties. In particular, an anomalous temperature behavior of the threshold current of some THz QCLs is investigated — the threshold current first decreases before it increases with temperature. For the study, a comprehensive series of superlattice structures, which are easier to

interpret, are grown with similar characteristics to low-doped THz QCLs: low-doped active regions, and comparable contact layers. The temperature-dependent current-voltage (IV) characteristics show, in some cases, the same anomalous temperature effect. Based on experimental and simulation results the origin and the temperature dependence of the effect is explained.

Kurzfassung

Molekularstrahlepitaxie (MBE) ist ein vielseitiges Werkzeug das sowohl Grundlagenforschung an Universitäten als auch die Produktion von Bauelementen in der Industrie erlaubt. In der vorliegenden Arbeit wurden Zinkblende III-V Halbleiter mit MBE gewachsen, wobei der Schwerpunkt bei der mittleren-Infrarot (MIR) bis THz Optoelektronik liegt. Genauer gesagt, beim Wachstum in Beziehung zu THz Quantenkaskadenlasern (QCLs) und kurz- bis mittel- Infrarot Quantenkaskadendetektoren (QCDs). Bauelemente in diesem Spektralbereich finden Anwendung in der Spektroskopie, der Telekommunikation, und der Bildgebung.

Die Doktorarbeit umfasst das Design, das Wachstum, die Analyse, die Herstellung, und die optische Charakterisierung von QCDs, die auf das vielversprechende InAs/Al(As)Sb Materialsystem erweitert wurden und auf InAs oder GaSb Substraten gewachsen wurden. Dieses Materialsystem bietet vorteilhafte intrinsische Eigenschaften wie eine der niedrigsten effektiven Elektronenmassen, welche die optische Absorptionsstärke erhöht, als auch einen der höchsten Leitungsband-Versätze (CBO), der Übergangsenergien bis zu Wellenlängen im nahen Infrarot erlaubt. Um InAs/Al(As)Sb zu wachsen wurden Wachstumsparameter, wie Gruppe-V Flüsse, Oxid-Entfernungstemperaturen, sowie Wachstumstemperaturen optimiert. Um ungewollte Gruppe-V Durchmischung oder As-für-Sb Austausch zu minimieren, wurden Shutter-Sequenzen implementiert, die in scharfen Grenzflächenübergängen resultieren. Es wurden QCDs mit Absorptionswellenlängen, die von 2.7—5.5 µm reichen designt, gewachsen, hergestellt, und charakterisiert und somit die weite Wellenlängenbandbreite dieses Materialsystems demonstriert, und, in diesem Prozess, die Reife von InAs/Al(As)Sb QCDs verbessert.

Im Besonderen wurde ein Oberseiten-beleuchteter (normal auf die Oberfläche) InAs/AlAs$_{0.16}$Sb$_{0.84}$ QCD gitterangepasst auf InAs gewachsen, produziert und mit einem Beugungsgitter verwirklicht. Die Absorptionswellenlänge von 2.7 µm liegt im Zentrum einer CO_2 Absorptionslinie und entspricht Energien über der Bandlückenenergie von InAs.

Auf GaSb Substraten wurden InAs/AlSb QCDs spannungsausgeglichen gewachsen mit einem InAs:AlSb Verhältnis drei Mal größer als das Verhältnis, das man benötigen würde um spannungsausgeglichen zu wachsen. Das wurde mit inkludierten sub-Monolagen InSb Lagen erreicht und ist notwendig, um die Freiheit zurückzugewinnen, die man mit gitterangepassten Materialien hat, das Design zu optimieren.

Wegen der Typ-II Bandausrichtung des InAs/Al(As)Sb Materialsystems ist die effektive Bandlücke für Interbandübergänge in den nahen Infrarotbereich reduziert. Das resultiert in der Beobachtung von starken breitbandigen Interbandsignalen von

1.2–3 µm, die direkt neben dem QCD Signal liegen.

MBE erlaubt es auch an material- und strukturellen Eigenschaften zu forschen. Im Speziellen wurde ein anormales Temperaturverhalten im Schwellenstrom von THz QCLs untersucht – wobei der Schwellenstrom zuerst mit der Temperatur niedriger wird bevor er sich erhöht. Für diese Studie wurde eine umfassende Serie von Übergitter-Strukturen, die einfacher zu interpretieren sind, mit ähnlichen Charakteristiken zu niedrig gedopten aktiven Zonen von THz QCLs gewachsen, die auch vergleichbare Kontaktlagen aufweisen. Die temperaturabhängigen Strom-Spannungskennlinien weisen in manchen Fällen, den gleichen anomalen Temperatureffekt auf. Basierend auf experimentellen Resultaten und Resultaten von Simulationen, wird der Ursprung der Temperaturabhängigkeit dieses Effektes erklärt.

Acknowledgements

Working on this Ph.D. thesis not only widened, and, at the same time, humbled my perception of my scientific knowledge, but it also influenced me on a deeply personal level. I am incredibly grateful for the support I received during this time.

I am truthfully thankful to my supervisor, Prof. Aaron Maxwell Andrews, for his guidance, immense knowledge, support, good ideas, and helpful advice. I am thankful for the freedom he gave me to follow my own ideas. Additionally, he was always available when needed, in the MBE lab, or for scientific discussions, which I do not take for granted.

I am very grateful to my co-supervisor Prof. Gottfried Strasser, firstly for offering me an opportunity to start my Ph.D. in his group, for his refreshing view on topics, and humor, but also for sharing his immense experience and invaluable knowledge.

I want to thank Prof. Karl Unterrainer for letting me participate in his group meetings countless times, for sharing his group's knowledge, and for his valuable feedback on my presentations.

Thank you to Prof. Gérald Bastard for listening to my presentations in many meetings and for sharing his great mind and scientific knowledge, also his kindness was not overlooked.

I am thankful to Prof. Benedikt Schwarz for sharing his invaluable knowledge on simulations and his experience in the optical lab with me. The CLAUS device simulation tool he developed allowed for this thesis to be in its current form.

My gratitude goes to Dr. Werner Schrenk for sharing his incredible scientific insight. He is truly irreplaceable as a cleanroom director. I am very impressed by the amount of knowledge he has not only on scientific topics but also on the technologies used in the cleanroom.

Thank you to Prof. Erich Gornik, Dr. Hermann Detz, and Dr. Borislav Hinkov for sharing their scientific knowledge with me.

A big thank you goes to my group members not only for the regular supply of cake and cookies but also for bringing enthusiasm into the workspace, and for freely given helpful discussions and hands when needed. Thank you Anna Lardschneider, Andreas Windischhofer, Mikolaj Piotrowski, Sandro Dal Cin, Florian Pilat, Nikola Opačak, Mauro David, Georg Marschick, Elena Arigliani, Rolf Szedlak, Lukas Fischer, Stefania Isceri, and Maximilian Beiser. Thanks to Sandro Dal Cin, Florian Pilat, and Georg Marschick for helping with MBE openings! Thank you to Andreas Windischhofer for always helping with problems with simulations and to Mikolaj Piotrowski for always bringing a good mood to the office. Thank you, Florian Pilat, for your support on questions regarding the optical lab. Thank you, Marie Ertl, for your support in the

cleanroom and the lab. Thank you to Michael Jaidl for being the fastest THz QCL processor and characterizer I know of, giving fast feedback to the MBE, and lending hands for MBE openings. This enthusiasm for fresh material contributed significantly to my motivation. Thank you to Martin Kainz and Hedwig Knötig for introducing me to the fabrication of devices in the cleanroom as a fresh Ph.D. student.

There are many more people at the institute who helped me with scientific input, manufacturing components, and administrative work. For this, I want to thank Andreas Linzer, Markus Schinnerl, Anton Tsenov, and Christine Brendt.

Thank you, Petr Ourednik, for your always open ears regardless of the topic, and your always thought-out advice. Thank you for caring about me, and for your ongoing support.

I want to thank my parents. They selflessly gave me everything, while they were here. I hope they planted good values in me. Hearing stories of how deeply valued they were by the people around them fills me with pride.

I am deeply grateful to my Greek aunt and uncle, although not really related treat me like their own daughter. I want to thank my twin brother for sharing the path with me.

Finally, I would like to thank the state of Austria for providing me with an excellent and completely free education up to the doctoral degree.

I do not take any of this for granted.

Contents

CHAPTER 1

Introduction

1.1 Motivation

Semiconductor technology includes some of the most important inventions of our time, tremendously impacting our everyday lives. Among its countless application fields is photonics, which involves the generation, detection, and transmission of light, with applications in information technology, life sciences, and consumer entertainment, mainly utilizing the near-infrared (NIR) and visible (VIS) light spectral range.

Most recently, the field of mid-infrared (MIR) photonics emerged. In this region, many important molecules have characteristic absorption lines, therefore this region was named the "molecular fingerprint region", see Fig. 1.1. This allows for applications in spectroscopy for environmental purposes [1, 2], where for example greenhouse gases can be monitored [3, 4], medical purposes [5], like performing breath analysis [6], in security [7], but also in imaging [8]. Furthermore, atmospheric windows of low absorption are found, which enable applications in free space optical telecommunication [9, 10].

With these unique properties, MIR photonics positions itself as an important complementary technology next to NIR and VIS photonics.

Many modern MIR devices are produced from III-V materials. The evolution of MIR photonics is therefore closely tied to the development of III-V semiconductor technology. With this knowledge of material parameters and the effects occurring in quantum-mechanical III-V heterostructures, scientists and engineers design, grow, and fabricate complex MIR devices that find applications in research and industry.
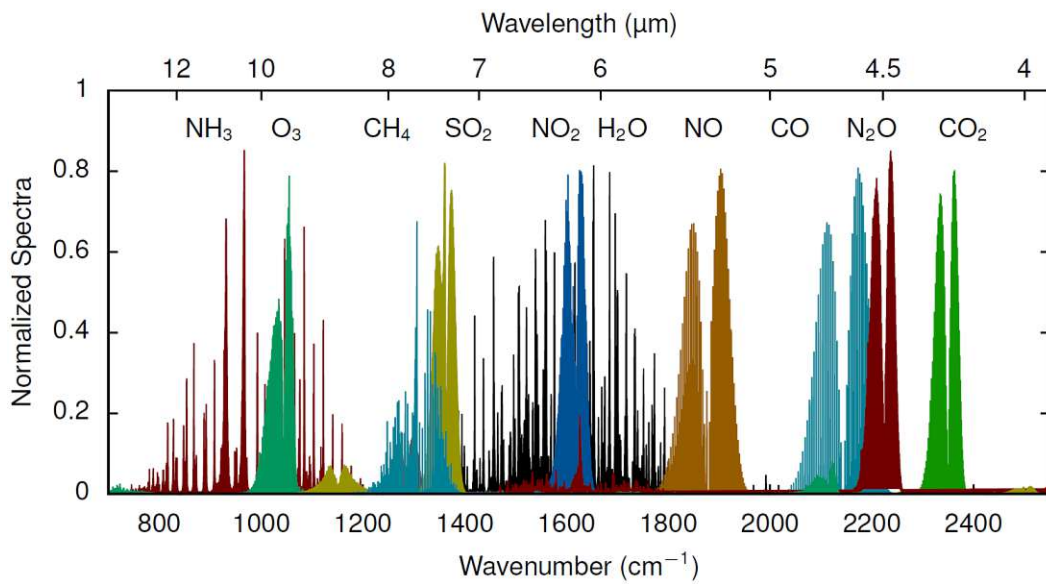
Figure 1.1: Absorption lines in the mid-infrared region of several important molecules. (Reprinted with permission from [11].)

III-V semiconductors lasers and detectors are often composed out of heterostructures, utilizing a quantum-mechanical working principle. Those devices work from the NIR over the MIR, the far-infrared (FIR) to the THz region, and are reduced in size to the microchip level. Recent developments have enabled monolithically integrated (single-chip) solutions for MIR lasers and detectors, allowing spectroscopy on a chip level [12]. This was achieved with quantum cascade lasers (QCLs), which are one of the most important compact, powerful, coherent, light sources in the MIR and THz regimes [13, 14]. Quantum cascade detectors (QCDs) are their detector counterpart with a broadly designable absorption range [15, 16].

Over the years, a multitude of other classes of MIR lasers and detectors were developed. To those belong interband cascade lasers (ICLs), quantum well-infrared photodetectors (QWIP), and interband detectors, including type-II or superlattice detectors, like P-i-N double heterostructures [17], p-B-p barrier detectors [18], or cascade infrared detectors [19], just to name a few. Not belonging to the III-V semiconductors, but mentioned due to their significance in the MIR regime are II-VI detectors, like HgCdTe (MCTs) [20]. Many of these lasers and detectors have been made commercially available [21–23].

This thesis concentrated on THz QCLs and MIR QCDs. The latter set themselves apart from the magnitude of photodetectors invented over the years by a narrow absorption spectrum, low noise at room temperature, due to photovoltaic operation, and high-speed intersubband detection [15, 16].

Due to the development of III-V semiconductor technology, materials like GaAs/Al-

GaAs or InGaAs/InAlAs have reached high maturity and are grown industrially. This thesis attempts to widen the selection and increase the maturity of the materials utilized for QCDs and also expand the QCDs to shorter wavelengths. Especially, the InAs/Al(As)Sb material system is promising for QCDs, because of its beneficial intrinsic properties. It offers one of the lowest effective electron masses, increasing the optical absorption strength, resulting in higher responsivities. This material system additionally provides one of the broadest designable absorption-wavelength ranges, due to its large conduction band offset (CBO) of $2.1\,\text{eV}$ ($1.2\,\text{eV}$ indirect), meaning that detection regimes can be expanded to the NIR. By doing this, the application range of QCDs can be extended.

With MBE, not just new material systems can be developed, but also for mature materials like GaAs/AlGaAs MBE has proven itself as a valuable tool in research over the years, not just to create devices, but also to investigate the underlying physics. In the quest for high-temperature THz QCLs, much effort is put into optimizing the heterostructure. Superlattice structures, which are arguably easier to analyze can help with this task because of their simplicity and similarity to device components and the vast literature knowledge of device physics.

1.2 Thesis outline

This thesis consists of six chapters. It is organized in a way that first, theoretical and basic knowledge that is needed is introduced, before the achievements and results of this thesis are presented: The fundamentals for the understanding of the physics of intersubband zinc-blende III-V devices, models, carrier scattering mechanisms, and devices are discussed in Chapter 2. In particular, the functioning principles of QCDs are explained, as well as the figures or merit. The state-of-the-art for QCD is presented, and a comparison to competing detectors is made.

Chapter 3 introduces crystals, the building blocks of heterostructures, and the doping of materials before the basics of epitaxy and MBE technology are discussed. After introducing growth mechanisms and surface effects, the growth optimization of the InAs/Al(As)Sb material system for QCDs grown either on InAs or GaSb substrates is discussed. Then, an overview of non-invasive and powerful analysis methods is given.

Chapter 4 presents the results of the grown InAs/Al(As)Sb QCDs lattice-matched to InAs and strain-balanced on GaSb substrates. A deep dive into the bandstructure design is done before the growth quality is analyzed. The fabrications for top-illumination and the 45° side-faced double-pass are illustrated. Finally, the results of

the optical characterization are presented.

In Chapter 5, an anomalous temperature effect occurring in the threshold current of some THz QCLs is investigated with a series of grown superlattice structures, and, with the help of multi-scattering Büttiker (MSB) simulations, it is attempted to give an explanation to the source of the behavior.

Finally, in Chapter 6, the thesis conclusions and outlook are presented.

Fundamentals of intersubband devices

In this chapter, mathematical models [24–27] for the description of III-V heterostructures are introduced. Carrier transport mechanisms, like interband, intersubband, and optical transitions as well as scattering processes are discussed. Band alignments of heterostructures are explained.

Vertical transport in superlattices, and transport effects occurring in superlattice structures in electric fields are discussed. The working principle of quantum cascade lasers (QCLs) is introduced.

A closer look is taken at quantum cascade detectors (QCDs). Their functioning principle, the figures of merit, optical coupling approaches, and the characterization are discussed. The state-of-the-art is reviewed and competing detectors are introduced.

2.1 Band structure of zinc-blende III-V heterostructures

The bandstructure, or the structure of electronic states, of III-V semiconductors is strongly determined by their crystal structure, which is either zinc-blende for P-, As-, and Sb- compounds, or wurtzite for III-Nitride semiconductors, as discussed in section 3.1 [25]. Depending on the individual atoms, the distance between single atoms can vary for the same crystal system, changing the lattice parameters.

The electrons, that contribute to chemical bonds and to transport or optical properties within a crystal are the outer electrons, of which there are eight for III-V
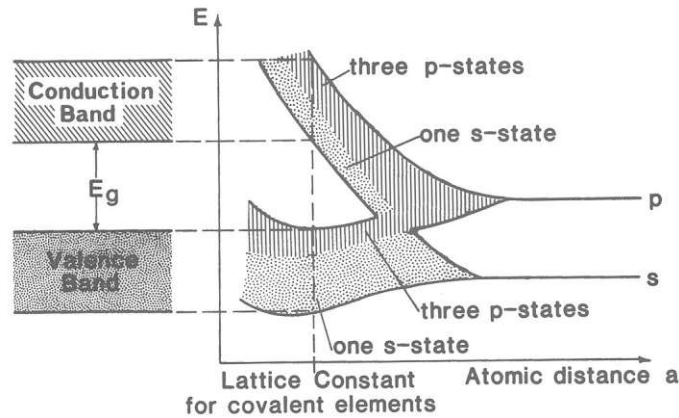
Figure 2.1: Illustration of the formation of bands depending on the interatomic distance of atoms in a crystal. With decreasing interatomic distance the orbitals hybridize and form bands. With increasingly smaller distances initially conduction- and valence band overlap, materials in this region are metallic. Further decrease leads again to a separation, materials are first semiconductors before they become insulators. ([28] Reproduced with permission from Springer Nature.)

binary compounds [24]. The atoms in face-centered cubic or hexagonal closest packed crystal lattices (see section 3.1) hybridize with an orbital of a neighboring atom while bonding- and anti-bonding states are formed with the s- and p- orbitals. These states form bands due to the high number of unit cells in a crystal. The bonding s and p bands are completely filled, while the anti-bonding bands are empty, where the lowest lying one forms the conduction band edge. This band is separated by an energy gap from the lower bands. A connection between the lattice parameters and the band gap exists, see Fig. 2.1. The smaller the lattice parameters, the larger the band gap. Or in other words, denser packed materials exhibit a larger band gap. In section 3.1 it is discussed that zinc-blende and wurtzite crystal structures, which are formed from face-centered cubic and hexagonal closest packed crystal lattices with a basis of two different atoms exhibit the highest achievable packing density of 0.74. III-Nitride semiconductors have smaller lattice constants, see Fig.3.4, and hence larger band gaps and stronger covalent bonds.

Fig. 2.2 shows the calculated band structures of bulk GaAs and bulk InAs. The structures look quite complicated, it is visible that more than one valence band band or conduction band band exists. Because we are focused on semiconductors, the conduction band is almost empty and the valence band is almost full. In the conduction band, electrons would accumulate at the minima, and in the valence band holes at the maxima. For the considerations of III-V semiconductor mid-infrared devices, the bandstructure close to the Γ-point is of importance, because the relevant states are there.
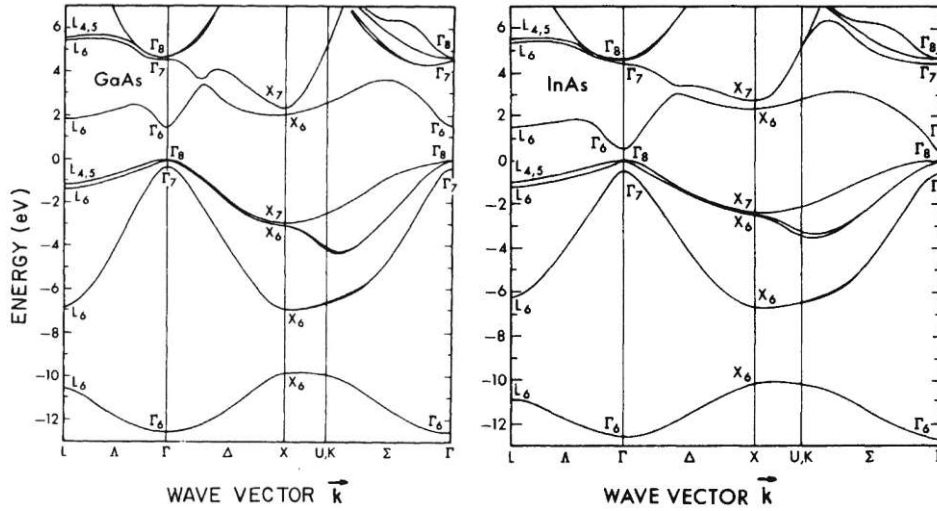
Figure 2.2: Calculated band structures for GaAs and InAs. (Reprinted with permission from [29]. Copyright 1976, American Physical Society (APS).)

2.1.1 Modelling of band structures

In the following, mathematical models used for the description of III-V semiconductors are introduced.

Bloch's theorem

As discussed in section 3.1, III-V semiconductor crystals are periodic structures, where translation symmetry holds. Due to this, the potential in such a crystal is periodic, with $V(\mathbf{r} + \mathbf{T}) = V(\mathbf{r})$, where $\mathbf{r}$ is the coordinate vector, $\mathbf{T} = n_1\mathbf{a}_1 + n_2\mathbf{a}_2 + n_3\mathbf{a}_3$ is the translation vector, with n_i being integers and a_i the lattice vectors. The motion of electrons in such a potential is described by the following wave function [26]:

$$\psi_{\mathbf{k}}(\mathbf{r}) = u_{\mathbf{k}}(\mathbf{r})e^{i\mathbf{k}\mathbf{r}}. \tag{2.1}$$

These are the Bloch waves, which are plain waves modulated by the lattice periodic factor $u_{\mathbf{k}}(\mathbf{r} + \mathbf{T}) = u_{\mathbf{k}}(\mathbf{r})$, called the Bloch function, the Bloch waves are therefore also periodic.

The k·p approximation

The k·p theory gives a model for the computation of the band structure and wave functions close to the Γ-point, near the Fermi energy, in bulk semiconductors. For most applications, the relevant states are found there.

Following [24, 26], in a crystal, the Schrödinger equation can be written as

$$\left(\frac{p^2}{2m_0} + V(\mathbf{r}))\psi(\mathbf{r}) = E\psi(\mathbf{r})\right) \tag{2.2}$$

where p is the momentum, m_0 is the free electron mass, $V(\mathbf{r})$ the crystal potential, E the energy and $\psi(\mathbf{r})$ the wavefunction at the coordinate vector $\mathbf{r}$. In this equation, terms stemming from spin-orbit coupling, the mass-velocity, and Darwin terms (only important for heavy atoms), are neglected.

Using the wave function in the Bloch form from above, see eq. 2.1 and $\mathbf{p} = -i\hbar\nabla$ the Schrödinger equation is

$$\left(\frac{p^2}{2m_0} + \frac{\hbar}{m_0}\mathbf{k}\cdot\mathbf{p} + \frac{\hbar^2 k^2}{2m_0} + V(\mathbf{r})\right) u_{n,\mathbf{k}}(\mathbf{r}) = E_{n,\mathbf{k}} u_{n,\mathbf{k}}(\mathbf{r}) \tag{2.3}$$

where $\mathbf{k}$ is the wavevector, $\hbar$ the reduced Planck constant, and the index n denotes the band. With this, one can split the Hamiltonian into a $\mathbf{k}$-dependent and independent term $H = H_0 + W(\mathbf{k})$, and use the perturbation theory, with

$$H_0 = \frac{p^2}{2m_0} + V(\mathbf{r}), \tag{2.4}$$

and

$$W(\mathbf{k}) = \frac{\hbar^2 k^2}{2m_0} + \frac{\hbar}{m_0}\mathbf{k}\cdot\mathbf{p}. \tag{2.5}$$

The solutions of the energies of the band structure are then calculated using only the unperturbed part of the Hamiltonian:

$$H_0 u_{n,0}(\mathbf{r}) = E_{n,0} u_{n,0}(\mathbf{r}), \tag{2.6}$$

The energy is then expanded to the vicinity of the Γ-point using second-order corrections stemming from the perturbed part of the Hamiltonian, with the Bloch functions as a basis.

Materials with a low effective electron mass m_e^* (see section 2.1.2) have larger kinetic energy, and a higher order perturbation is necessary. The Kane model (refer to [24]) then results in a non-parabolicity coefficient, more accurately describing the bands of these materials.

To increase accuracy, models that are used in practice include four bands, one conduction band, and three valence bands, which stem from the spin-orbit coupling term in the Schrödinger equation, or eight bands if their degeneracy is accounted for. Fig. 2.3 depicts the band model. The conduction band (CB) is formed from an s-like orbital. The three valence bands (VB), the heavy hole (HH), the light hole (LH), and the split-off (SO) band are formed from p-like orbitals. Δ is the split-off energy.
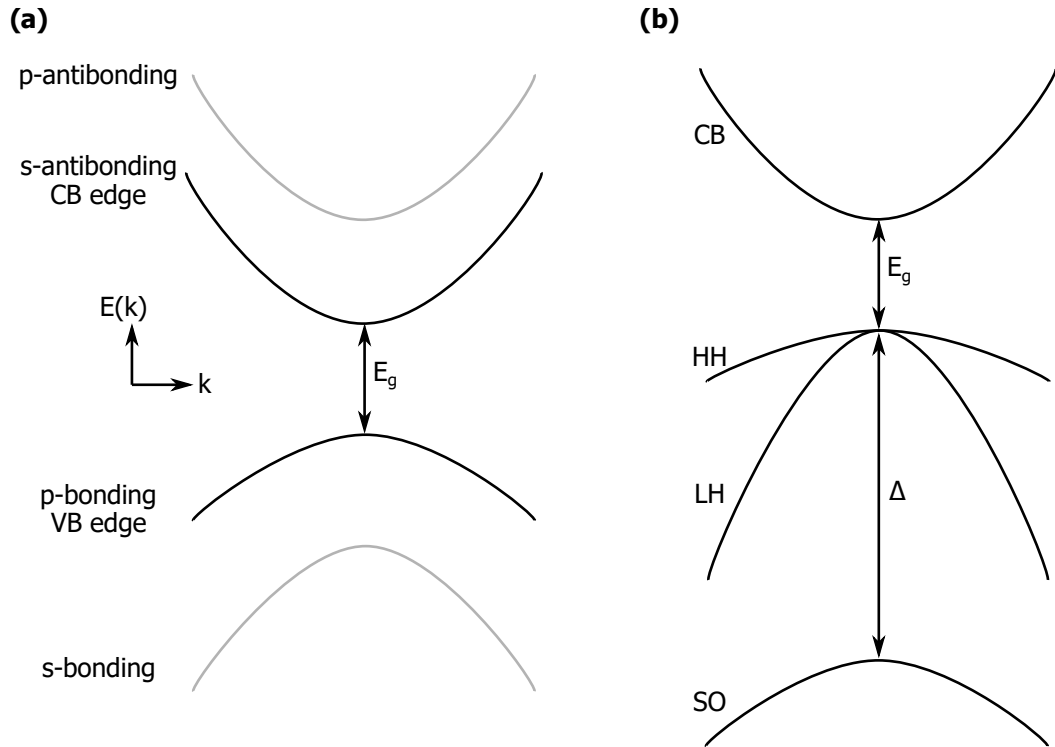
Figure 2.3: a) Formation of the conduction band (CB) and valence band (VB) from s-like and p-like states, respectively. The valence band splits into the heavy hole (HH), light hole (LH), and split-off (SO) bands if spin-orbit coupling is considered. (Reprinted with permission from [30].)

The envelope function approximation

With the envelope function approximation, it is stepped away from crystalline bulk materials and heterostructures are now considered [24, 26]. For these structures, at least two different semiconductors are alternated, see subsection 2.1.2 for the band alignment. The thicknesses of the single layers are on the order of magnitude where quantum confinement occurs for the electrons, and quantum wells form. Therefore, the solution now needs to be spatially defined.

Now the Bloch functions, which are assumed to be the same for the different materials, are multiplied by a slowly changing spatially dependent function. One now obtains the following wavefunctions [26]:

$$\Psi(\mathbf{r}) = \sum_l f_l^{A,B} u_{l,0}(\mathbf{r}) \tag{2.7}$$

where the envelope function $f_l^{A,B} u_{l,0}$, for materials A and B, can be written, due to the in-plane translational invariance as

$$f_l(r_{||}, z) = \frac{1}{\sqrt{S}} \exp(i(k_x x + k_y y))\chi_n(z) \tag{2.8}$$

where $r_{||}$ is the in-plane coordinate vector, S is the in-plane surface area, and $\chi_n(z)$ the wavefunction. Fig. 2.4 shows a sketch of the envelope function for a heterostructure of material A and material B. It is visible that the difference in crystal potentials leads to the formation of a quantum well. Most of the probability of the envelope function is in material B, because the electron is confined there.
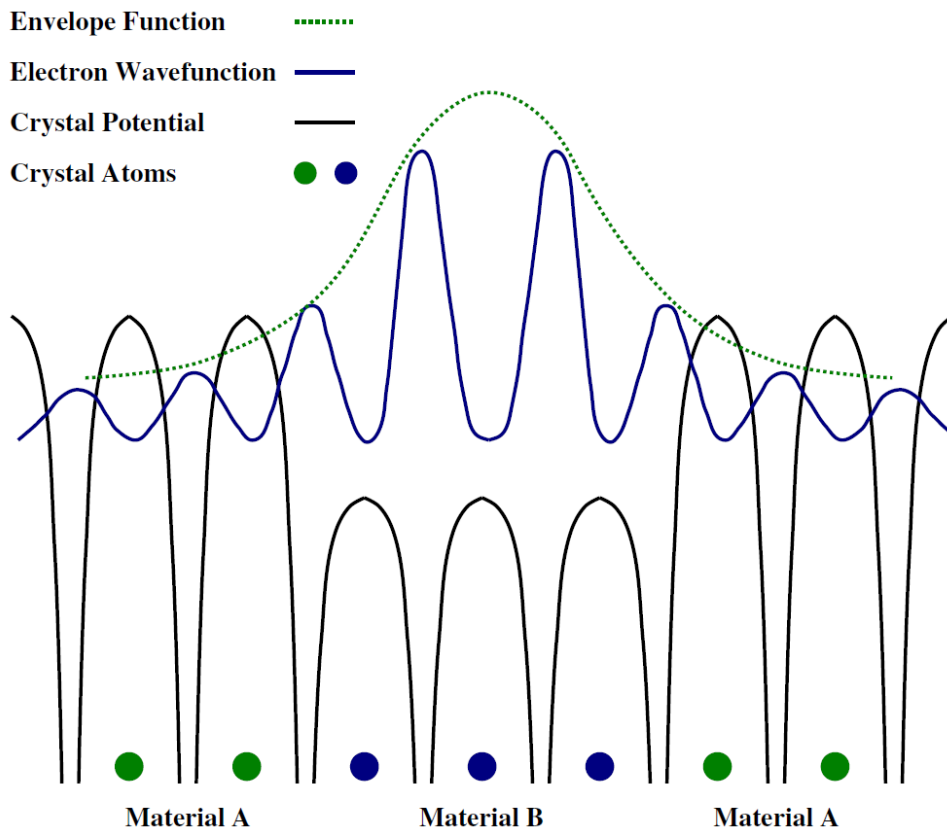
Figure 2.4: The envelope function and the single electron wave function are sketched for one quantum well. (Reprinted with permission from [31].)

2.1.2 Bands of heterostructures

In the following, important parameters for the full description of real devices are discussed.

The effective electron mass - semiclassical model:

Electrons have a parabolic energy dispersion in the first approximation, of $E = \frac{\hbar^2 k^2}{2m}$.

In the bands discussed, electrons do not behave like free electrons. In the following, the movement of electrons in bands is covered in a semiclassical approach [32].

Band electrons experience a force $\mathbf{F}$ that during a time interval dt performs the work $dE = \mathbf{F}\mathbf{v}dt$, whereas $\mathbf{v}$ is the velocity of electrons in the band, and $dE = \nabla_k E d\mathbf{k}$. $d\mathbf{k}$ is the change of the wave vector with time. With this, one can write for the group velocity

$$\hbar\frac{d\mathbf{k}}{dt} = \mathbf{F} \tag{2.9}$$

With the above relations, the change in velocity is

$$\frac{dv}{dt} = \frac{1}{\hbar}\frac{d^2E}{dk^2}\frac{dk}{dt} \tag{2.10}$$

and thus

$$\frac{\hbar^2}{\frac{d^2E}{dk^2}}\frac{dv}{dt} = F = m_e^*\frac{dv}{dt} \tag{2.11}$$

where m_e^* is the effective electron mass describing the movement of electrons in bands

$$m_e^* = \frac{\hbar^2}{d^2E/dk^2} \tag{2.12}$$

Now the mass of the electrons is given by the trend of $E(\mathbf{k})$ and is thus energy-dependent. It describes how the periodic potential of the crystal lattice modifies their movement.

From the $\mathbf{k}\cdot\mathbf{p}$ theory, the following equation for the effective mass is obtained [26]:

$$(m_e^*)^{-1} = (m_0)^{-1}(1 + \frac{E_p}{E_g}), \tag{2.13}$$

where E_p is the Kane energy parameter, a material constant, E_g is the band gap, and $E_p >> E_g$. Therefore, the effective mass is approx. proportional to E_g. This means that materials with a small effective mass also have a small band gap.

Band alignment of heterostructures:

For heterostructures, the knowledge of the alignment of the conduction and valence band for the different materials involved is important. Fig. 2.5 shows the band alignment for important III-V binary semiconductors at the Γ-point. It is visible that discontinuities between the semiconductors exist. The conduction band offset (CBO) is the difference in alignment of two semiconductors.

The alignment of semiconductors to each other has been categorized into different
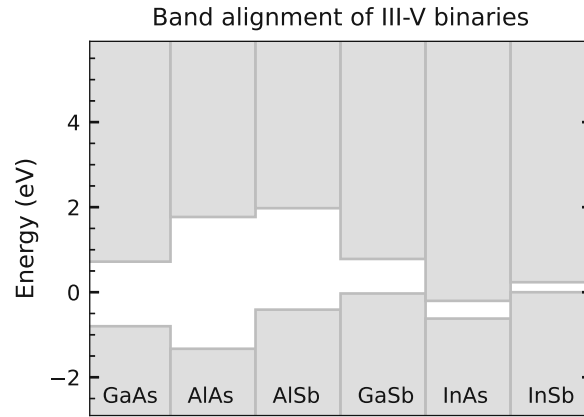
Figure 2.5: The alignment at the Γ-point of the valence band maximum and the conduction band minimum at 300 K is sketched. Data from [25].
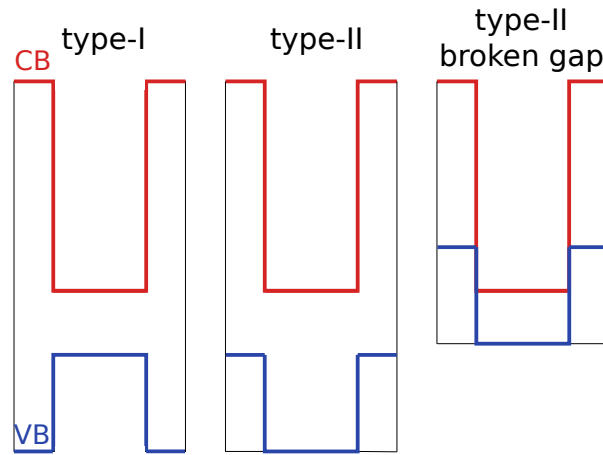
Figure 2.6: Sketch of the different types of band alignment in III-V heterostructures. For type-I structures the bandgaps overlap, for type-II structures, the bandgap of one material is below the valence band edge of the other material, and for type-II broken gap the conduction band edge of one material is below the valence band of the other material.

categories [33]. Type-I heterostructures align in a way that the bandgaps overlap, see Fig. 2.6. This happens, for example, for GaAs/AlGaAs heterostructures. For type-II heterostructures, the bandgap of one material is aligned below the valence band edge of the second material, which is the case for the InAs/AlSb material system. For type-II broken gap heterostructures, the bandgap and the conduction band edge fall below the valence band of the other material. This happens for example for InAs/GaSb and is utilized in interband cascade lasers (ICL), where it is referred to as a semimetallic interface.

Band bending:

Band bending is the deformation of the band structure as a result of its electronic properties. Heterostructures often experience band bending at the material interface region due to differences in doping. A difference in doping can also occur in two layers of the same material, for example, grown contacts, that then cause band bending through the introduction of space charge effects [27, 34].

The band alignment of two semiconductors can be constructed in a simplified approach by the Anderson rule, which assumes that the two semiconductors, when brought together, behave as they would in a vacuum. The Anderson rule states that when two semiconductors are brought together, their vacuum levels given by the magnitude of the electron affinity χ (defined as the energy needed to release an electron from a simply charged anion to form a neutral atom) must line up. Additionally, when brought together in equilibrium conditions, the Fermi levels E_F must align, because charge neutrality exists, see Fig. 2.7, where E_C denotes the conduction band edge, and E_V the valence band edge.

Fig. 2.7 a) depicts the case of the same material with different doping, as it is often the case when a contact layer is grown. The electron affinities are the same magnitude and the band bending resembles the case of a p-n junction, with the difference that the materials brought together are both n-type.

In Fig. 2.7 b) a case of two different semiconductors brought together is depicted. When the electron affinities are aligned and the semiconductors are brought together a discontinuity of the band edges forms. This band alignment is the special case of a two-dimensional electron gas (2DEG). Due to the larger energy gap of material 1 electrons are depleted into material 2, which leads to the conduction band of material 1 to bend up and of material 2 to bend down [27]. At the discontinuity where E_{c2} bends down below the Fermi level, electrons accumulate, which then form the 2DEG, see the red region in Fig. 2.7 b). 2DEGs are useful devices with applications in industry, where they function as magnetic sensors utilizing the Hall effect. Also for molecular beam epitaxy (MBE) growth, 2DEGs are helpful tools to evaluate the system purity and growth performance, due to the dependency of the electron concentration and mobility on impurities.

The Anderson model describing the band alignment is limited because, in reality, the situation is more complicated [35]. Even at perfect lattice-matched interfaces, electronic interface states exist, where wavefunctions of one semiconductor penetrate into the other, which are called interface-induced gap states, additionally, chemical bonding is neglected [34, 35]. A high density of interface states can also pin the Fermi level at a certain location. All of these effects can completely change the band
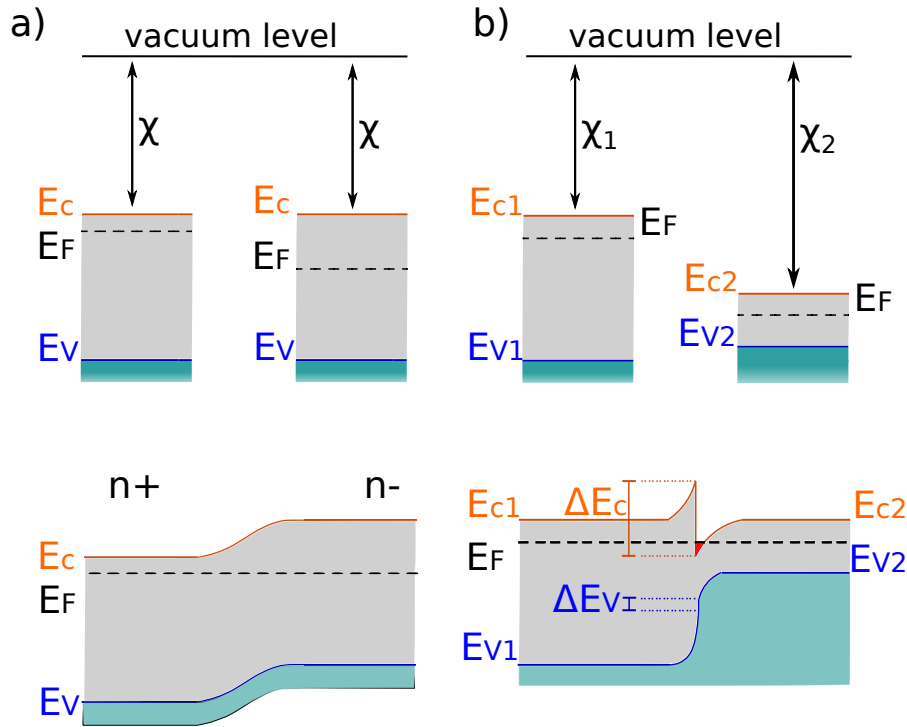
Figure 2.7: a) Two semiconductors of identical material, but different n-type doping concentrations are brought together. In equilibrium conditions, in addition, to the vacuum levels, which are given by the electron affinities χ, the Fermi levels E_F must align and a space charge region results in band bending. E_C denotes the conduction band edge, and E_V the valence band edge. b) Band structure lineup of two different semiconductors. The alignment of the vacuum level and the Fermi level in equilibrium causes a discontinuity to form, where electrons accumulate. This special structure is called a two-dimensional electron gas (2DEG).

structure lineup. In addition, the bonds between two semiconductors are mostly covalent but also partly ionic, because, due to two different atoms forming one base in zinc-blende structures, some electrons are closer to one ion than the other, which induces interface dipoles. All of this is usually neglected in models. For a detailed discussion please refer to [34, 35].

Contacts to semiconductors: Schottky contacts:

A Schottky contact can form at a metal-semiconductor interface. The behavior is similar to the band bending at a semiconductor-semiconductor interface. The difference is that the Fermi level lies in the conduction band of the metal and the electron affinity of the semiconductor now must align with the metal work function (defined as the minimum energy needed to remove an electron from a solid). This is called the Schottky-Mott rule, which has the same limitations as the Anderson rule. For n-type semiconductors, in equilibrium, the Fermi levels E_F align. If the

vacuum electron affinity χ of the semiconductor is smaller than the metal work function Φ_M, the conduction band and valence band will bend up to align χ_S with Φ_M and a depletion region will form. If χ is larger, the conduction and valence band bend down and an accumulation region forms, see Fig.2.8 a) and b), with $\Phi_{MS} = \Phi_M - \Phi_S - (E_C - E_F)$ [27], where Φ_{MS} is the metal-semiconductor work function, Φ_S the semiconductor work function, E_C is the conduction band edge, and E_V the valence band edge. This results in a rectifying behavior [34, 35].
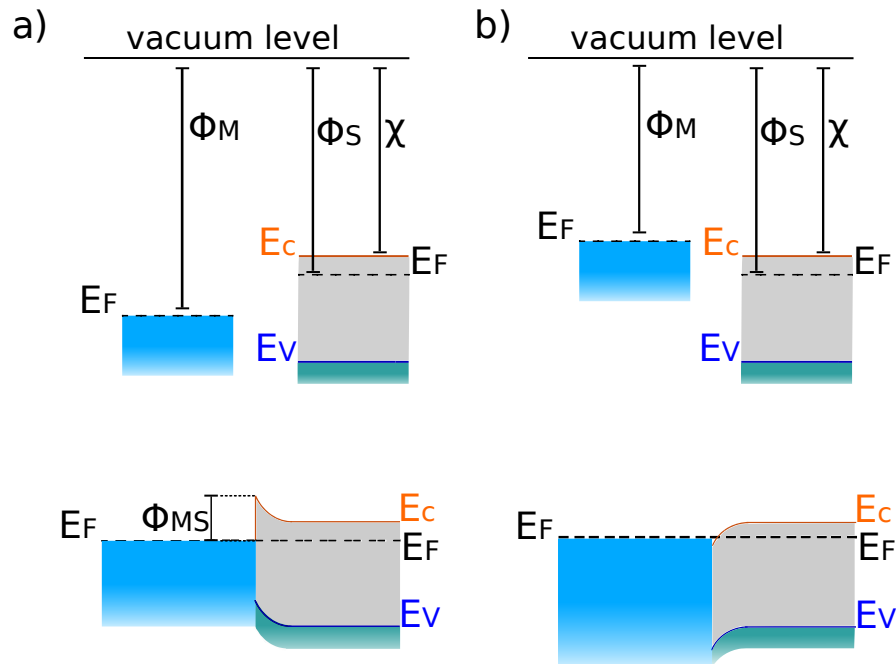
Figure 2.8: Metal- n-type semiconductor band alignment, with Φ_M the metal work function, Φ_{MS} is the metal-semiconductor work function, Φ_S the semiconductor work function, χ the vacuum electron affinity of the semiconductor, E_F the Fermi level, E_C is the conduction band edge, and E_V the valence band edge. a) Sketch of the case of a metal with a high work function. The semiconductor conduction band bends upwards at the discontinuity creating a Schottky barrier. b) Sketch of the case of a metal with a low work function, the semiconductor bands downwards, and a charge accumulation region forms.

Au forms a Schottky barrier with GaAs, whereas an ohmic contact would form with a Ge/Au alloy. InAs and Au form an ohmic contact.

2.2 Transitions in III-V semiconductors

In III-V heterostructures radiative and non-radiative interband and intersubband transitions are possible, as well as various scattering mechanisms, which will be discussed in the following.

2.2.1 Interband vs intersubband transition
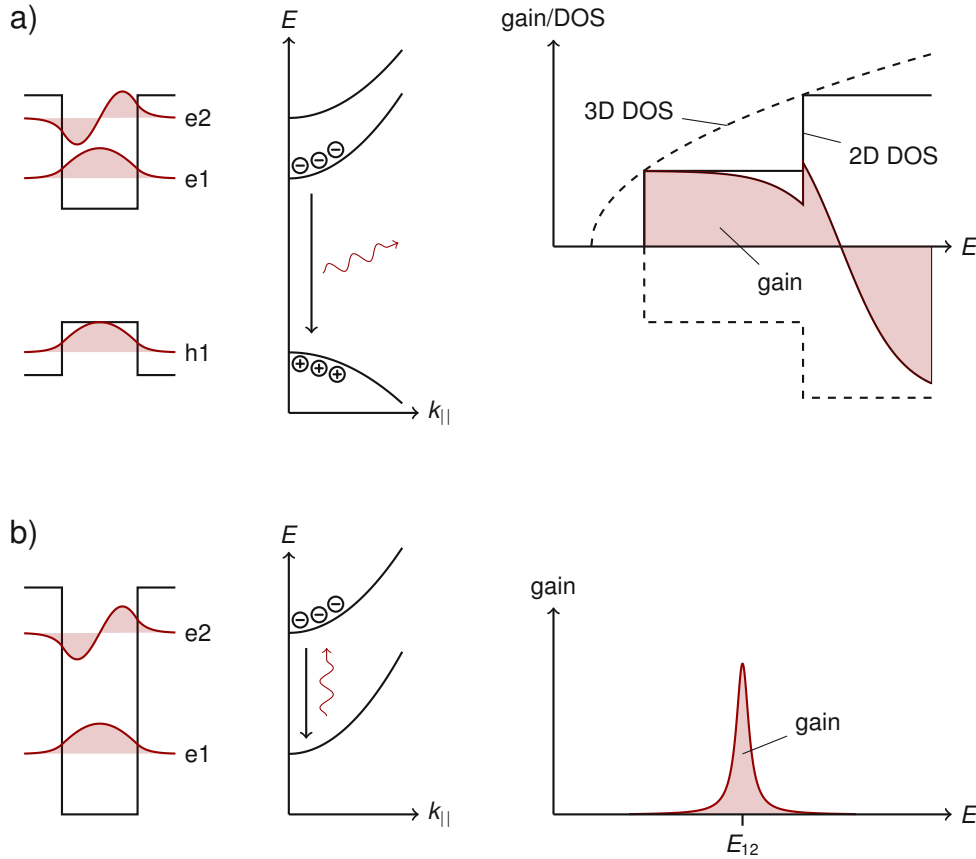
Figure 2.9: a) Sketch of interband transitions and b) intersubband transitions. Note the different energy dispersions of valence and conduction band for interband transitions, which leads to a different gain profile than for intersubband transitions. (Reprinted with permission from [11].)

Fig.2.9 shows a) an interband and b) an intersubband transition (with type-I alignment). While for a) the transition takes place between two bands, for b) it takes place between two subbands in the same band. For an interband transition, the transition energy minimum is limited by the bandgap, while no such limit for intersubband transitions exists. Another difference is the shape of the in-plane dispersion. While the dispersion is the opposite for interband absorption it is the same for intersubband absorption. As a consequence, there is no energy gap for the latter and if the necessary momentum exchange is provided by either elastic or inelastic processes, the electron will change subband. The absorption coefficient for intersubband devices is around $10^3 \, \mathrm{cm}^{-1}$, around one order of magnitude lower than for interband devices, for which radiative transitions dominate.

The density of states also differ, see Fig. 2.9. For intersubband transitions, it is delta-like, because just single levels are involved, like in an atomic system, although

the absorption line is broadened due to scattering. The density of states looks different for interband transitions. There is a cut-on in energy but due to the dispersion shapes no clear cut-off.

Intersubband transitions follow the intersubband selection rule, which will be derived in the next subsection.

2.2.2 Optical transitions

Following [24, 26], the interaction between the optical field with the electrical structure can be described with the perturbation theory. For this, the Hamiltonian is written as a sum of the stationary unperturbed Hamiltonian H_0, plus a time-dependent perturbation term $H_{int}(t)$ arising from the interaction between the optical and electrical field.

$$H = H_0 + H_{int}(t) \tag{2.14}$$

The electron momentum $\mathbf{p}$ in an optical field is influenced by the vector potential $\mathbf{A}$ and replaced by $\mathbf{p} - q\mathbf{A}$, where q is the carrier charge. With $q = -e$, the electron charge, H can be written as

$$H = \frac{(\mathbf{p} + e\mathbf{A})^2}{2m} = \frac{\mathbf{p}^2 + e\mathbf{A} \cdot \mathbf{p} + e\mathbf{p} \cdot \mathbf{A} + e^2\mathbf{A}^2}{2m} \tag{2.15}$$

using the gauge $\nabla \mathbf{A} = 0$, m is the effective electron mass $m = m_e^*$ in the one-band model. In a multi-band model, it would be the rest electron mass $m = m_0$. For low field intensity, one can neglect the term $\mathbf{A}^2$, further employing the dipole approximation where spatial dependence of $\mathbf{A}$ is neglected, $\mathbf{A}$ and $\mathbf{p}$ commute and one writes

$$H = \frac{\mathbf{p}^2}{2m} + \frac{e\mathbf{A} \cdot \mathbf{p}}{m} = H_0 + H_{int} \tag{2.16}$$

With the Fermi Golden rule, the transition probability of an electron making a transition from the initial state $|\psi_i\rangle$ to the final state $|\psi_f\rangle$, with the energies $E_f > E_i$ can be written as

$$P_{if} = \frac{2\pi}{\hbar} \frac{e^2 E_0^2}{4m^2\omega^2} |\langle\psi_i| \mathbf{e} \cdot \mathbf{p} |\psi_f\rangle|^2 \delta(E_f - E_i - \hbar\omega) \tag{2.17}$$

where $\mathbf{e}$ is the polarization, stemming from the vector field $\mathbf{A}$, and $\mathbf{E_0}$ the amplitude of the electric field perpendicular to the propagation direction. This equation does not consider the occupancy of the levels, for this please refer to [24].

The electron state wave functions $|\psi_{i,f}\rangle$ can be expressed by the envelope function

approximation

$$\psi_{i,f} = f_{i,f}(\mathbf{r})u_{\nu,\nu'}(\mathbf{r}) \tag{2.18}$$

with the bands ν and ν' where

$$f_i(\mathbf{r}) = \frac{1}{\sqrt{S}} \exp(i\mathbf{k}_\perp \cdot \mathbf{r}_\perp)\chi_i(z) \tag{2.19}$$

where $k_\perp = (k_x, k_y)$, and $r_\perp = (x, y)$. With the expression of the wave functions one can write

$$\langle \psi_i | \, \mathbf{e} \cdot \mathbf{p} \, | \psi_f \rangle \approx \mathbf{e} \cdot \langle u_\nu | \, \mathbf{p} \, | u_{\nu'} \rangle \langle f_i | f_f \rangle + \delta_{\nu,\nu'} \mathbf{e} \cdot \langle f_i | \, \mathbf{p} \, | f_f \rangle \tag{2.20}$$

The second part of this equation is just non-zero if the transition occurs in the same band (intersubband transition). The first part of the equation corresponds to interband transitions. Plugging in the relation for $f_{i,j}$ one can write [24]

$$\langle f_i | \, \mathbf{e} \cdot \mathbf{p} \, | f_f \rangle = (e_x \hbar k_x + e_y \hbar k_y)\delta_{\nu,\nu'}\delta_{\mathbf{k}'_\perp, \mathbf{k}_\perp} + e_z \delta_{\mathbf{k}'_\perp, \mathbf{k}_\perp} \times \int dz \chi_\nu^*(z) p_z \chi_{\nu'}(z) \tag{2.21}$$

From this equation, it is visible that e_x and e_y just allow transition within the same subband (intraband transitions). Only e_z allows transitions to different subbands. This means that an intersubband detector is just sensitive to electric field components in the growth direction. This is referred to as the intersubband selection rule.

One can define the oscillator strength f_{if} as [26]

$$f_{if} = \frac{2m_0}{\hbar^2} |\, \langle i | \, z \, | f \rangle \,|^2 (E_f - E_i) \tag{2.22}$$

where $\langle i | \, z \, | f \rangle = \frac{1}{im_e^* \omega_{if}} \langle i | \, p_z \, | f \rangle$ in the one-band model. Then the sum rule for the oscillator strength is in the one-band model:

$$\sum_i f_{if} = \frac{m_0}{m_e^*} \tag{2.23}$$

This equation reveals an important relation of the oscillator strength with the effective electron mass. This equation means that the transition strength is larger for materials with smaller effective electron mass.

The absorption strength of a 2-D system in the one-band model, taking into account scattering due to phonons and interface roughness, which broadens the linewidth [26], is

$$\alpha(\omega) = \frac{e^2 \omega z_{ij} n_i}{\epsilon_0 nc} \frac{\gamma}{(E_f - E_i - \hbar\omega)^2 + \gamma^2} \frac{sin^2\theta}{cos\theta} \tag{2.24}$$

where z_{ij} is the dipole matrix element, n_i the population of the initial state, ϵ_0 the vacuum permittivity, n the refractive index, and the Lorentzian linewidth is given as

$$\frac{\gamma/\pi}{(E_f - E_i - \hbar\omega)^2 + \gamma^2} \tag{2.25}$$

where γ is the half-width. Note, that the employed one-band model assumes parabolic bands and is therefore only valid for small energies.

2.2.3 Intersubband scattering mechanisms

The transport of electrons is influenced by various scattering mechanisms [26, 33, 36]. These processes can be elastic, such as electron-electron scattering, impurity, alloy, or interface roughness scattering. Inelastic processes are acoustic- or optical phonon scattering. In III-V intersubband devices, longitudinal optical (LO) phonon scattering is the most efficient process if the energy separation between the subbands is larger than the phonon energy of the material or at elevated temperatures. Only if the energy separation is lower, or at low temperatures, the situation changes and interface roughness scattering and electron-electron scattering are more efficient. Scattering processes are described by Fermi's golden rule.

The electron mobility μ is definded as

$$\mu = \frac{e\tau}{m_e^*} \tag{2.26}$$

where τ is the relaxation time, e the electron charge, and m_e^* the effective electron mass. Fig. 2.10 depicts the temperature dependence of the mobility due to the various scattering mechanisms, which will be described in the following.

Spontaneous emission:

For intersubband devices, the lifetime for spontaneous emission varies from tenths of ns to hundreds of µs depending on the square of the photon energy, in other words, the well width [26]. Compared to the ps lifetime of phonon scattering, the efficiency is low. This is in contrast to interband devices where radiative emission is dominant.
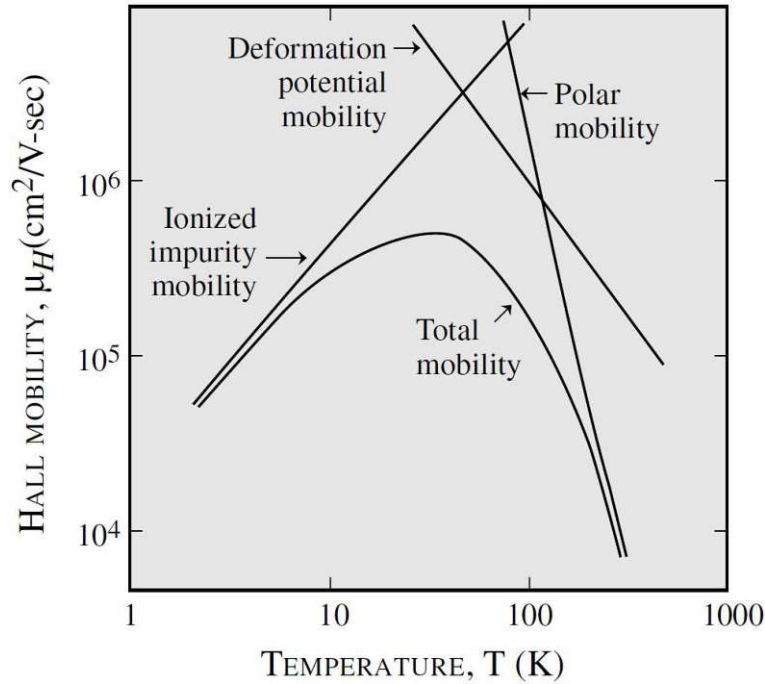
Figure 2.10: Low-field temperature-dependent electron mobility in bulk GaAs. (Reproduced with permission of Cambridge University Press through PLSclear [33].)

Optical phonon scattering:

Phonons are quantized lattice vibrations and scattering can be described by the Fröhlich Hamiltonian because phonons have little dispersion, see Fig 2.11. Energy-independent values are given for the material systems, in table 4.1.
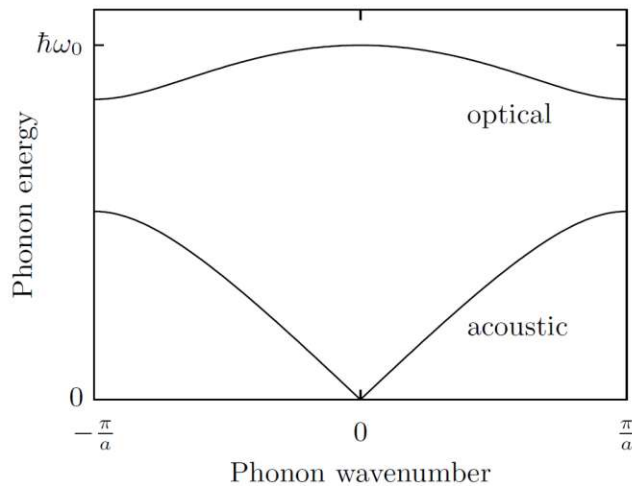
Figure 2.11: Optical and acoustic phonon dispersion. It is visible that in contrast to acoustic phonons, optical phonons have low dispersion. (Reprinted with permission from [11].)

As mentioned above, the optical phonon scattering process can occur if the energy

separation between intersubband levels is greater than the optical phonon energy or the electrons have sufficient kinetic energy. At temperatures above 60 K phonon scattering by thermal activation is dominant [26]. Optical phonon scattering is most efficient if the separation is resonant [37]. The optical phonon lifetime is in the sub-picoseconds to picoseconds range. If the electrons have increased in-plane kinetic energy, the optical phonon lifetime increases.

Phonons have longitudinal and transversal modes. For optical phonons, the atoms move 180° out of phase with each other, and, due to the polarity of III-V materials, the longitudinal optical phonon mode is the dominant mechanism.

Acoustic phonon scattering:

Acoustic phonons are quantized acoustic waves, where the atoms move in the same direction. Acoustic phonon scattering only plays a role in clean systems due to the dominance of LO phonon scattering. The lifetime of such a process is in the tenths of ps to hundreds of ps [26]. Their dispersion is visible in Fig. 2.11.

Impurity scattering

Impurity scattering is an elastic scattering mechanism and can occur on neutral and ionized impurities, whereas the latter dominates. Dopant atoms are impurities purposefully introduced into the crystal structure, which are ionized. Therefore, impurity scattering is largely dependent on the doping level and becomes significantly large for doping concentrations around $10^{17}\,1/\mathrm{cm}^3$ [26, 36]. In the vicinity of the optical transition, dopant atoms can cause a reduction in operating temperature due to impurity scattering [38]. On the other hand, the intersubband electroluminescence linewidth in coupled-quantum well heterostructures could be narrowed if the doping was moved away from the optical transition [39]. Therefore, this is taken into account in the design of devices.

Alloy scattering

Ternary or quaternary III-V semiconductors consist of two or more group-III or group-V elements, which can occupy the same lattice points, and an alloy forms, for which the translation symmetry is limited. Therefore, the mobility inside these materials, even at low temperatures is limited [26, 40]. The wave function resides mostly in the well and only a small fraction is in the barrier. Therefore, materials like $\mathrm{GaAs/Al_xGa_{1-x}As}$ or $\mathrm{InAs/AlAs_{0.16}Sb_{0.84}}$, which were grown for this thesis, exhibit weak alloy scattering. Nevertheless, alloy scattering has a $\sqrt{E}$ energy-dependency,

and therefore increases for short wavelength devices.

Interface roughness scattering

Interface roughness is due to growth imperfections at interfaces. They can be material-dependent or growth-related, due to the surface step heights and correlation length. These parameters can be controlled, for example, by the growth temperature [41]. This scattering mechanism is largely responsible for the broadening of intersubband transitions and becomes more important for higher transition energies. The interface roughness scattering depends largely on the in-plane kinetic energy and therefore shows temperature dependence.

Electron-electron scattering

This scattering mechanism only plays a role for clean samples at low temperatures. It is an elastic scattering process that can move electrons to different subbands.

2.3 Superlattices

Superlattices are probably the simplest form of heterostructures, consisting of two alternating layers of two materials. The repeating layer sequence is called one period. They were first demonstrated in 1970 by Esaki and Tsu in the GaAs/AlGaAs material system [42]. Many effects that more complex devices build on were first observed in superlattices, like Bloch-oscillations [43], Warnier-Stark ladders [44], or the formation of electric field domains [45, 46].

Despite the apparently structural simplicity of superlattices, a magnitude of different effects occurs, which can be quite complicated. In the following, just a few relevant effects for this thesis will be introduced [47].

2.3.1 Vertical transport

Superlattices are categorized into two main groups based on the coupling of the wavefunctions in the single wells to each other. For thick barriers weakly coupled superlattices form, for which the wavefunctions extend just to the neighboring wells. The transport can be assumed to be sequential resonant tunneling [47]. The quantum wells can be viewed as insulated. For thin barriers strongly coupled superlattices form and the wavefunctions extend over many adjacent periods and the transport mechanism is miniband transport [48]. The states that form in the latter need to be described in the form of extended states, for example, Bloch functions.
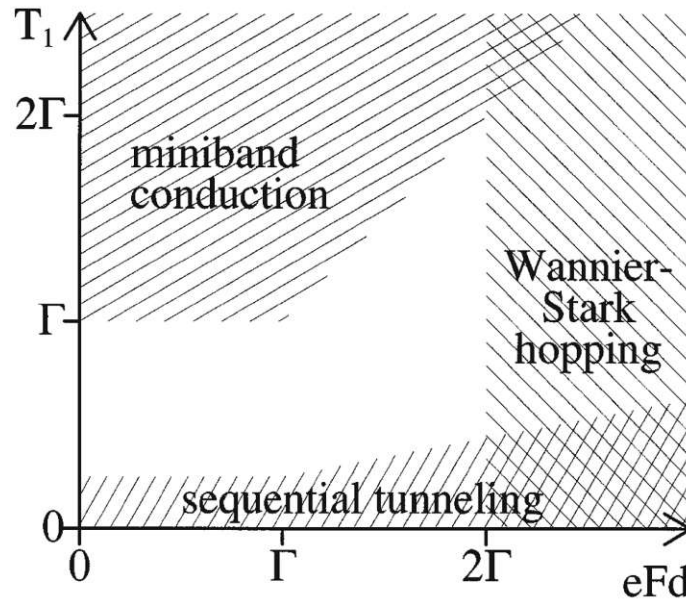
Figure 2.12: Vertical transport regimes for different transport models of superlattices, plotted in dependence of the miniband width (four times the interwell width T_1) and the electric field eFd. $\Gamma/\hbar$ is the scattering rate. (Reprinted with permission from [49]. Copyright 1997, American Physical Society (APS).)

In reality, the form of transport also depends on other parameters like miniband width, scattering rate $\Gamma/\hbar$, and the applied electric field eFd. Above, two transport mechanisms were already mentioned, but a third exists as well, namely Wannier-Stark hopping [50]. Fig. 2.12 depicts the regimes for the different mechanisms, valid for low electron densities and temperatures [49].

2.3.2 Superlattices in electric fields

When applying an electric field to a heterostructure it is assumed for simplicity that the electric field is homogeneous over the entire structure, but this is often not the case, and electric field domains (EFD) will form.

Complicated devices like THz QCLs or QCDs are described with the same transport mechanism of sequential resonant tunneling of weakly coupled superlattices. In weakly coupled superlattices interesting nonlinear phenomena were observed [47]:

As the name already suggests, in EFDs, electric fields are separated by a domain wall, consisting of a charge monopole or charge accumulation layer. This domain wall may move with the electron flow or in the opposite direction [51]. It can also be pinned [51].

In subsection 5.3.1 the observation of negative differential resistance (NDR) segments in current-voltage (I-V) characteristics of superlattices is explained by the

formation of a low- and high electric field domain separated by a charge accumulation layer. I-Vs of superlattices also show multistabilities in the current depending on the voltage starting point [52].

2.4 Quantum cascade lasers (QCLs)

QCLs are mid-infrared (MIR) to THz lasers that are electrically driven, utilizing unipolar intersubband transitions in the conduction band [13]. Due to their functioning principle, one electron cascading through the structure can be responsible for the emission of multiple photons, which results in high output powers [53]. QCLs in the MIR to far-infrared work at room temperature, whereas this achievement is still pending for THz QCLs, although an effort is dedicated towards it. One reason is the narrow energy separation of the laser levels ($< 30\,\mathrm{meV}$), making the suppression of unwanted leakage channels critical. Additionally, free-carrier absorption is prominent in the THz regime, which results in high optical losses. For this reason, THz QCLs are doped considerably low about $3\times10^{10}\,\mathrm{cm}^{-2}$.

2.4.1 Functioning principle

Over the years multiple approaches have developed to the design of the active region, including miniband, bound-to-continuum, two-well, three-well, and four-well designs [55]. These designs are all variations of the classic three-level system for gain. The emission wavelength of QCLs can be tailored by changing the well and barrier widths in the active region. Fig. 2.13 depicts the working principle. Electrons injected into the upper laser level $|2\rangle$ emit a photon by relaxing to the lower laser level $|1\rangle$. The primary condition for lasing is the existence of a population inversion. Therefore a fast extraction of the electrons of the lower laser level is necessary. This is accomplished by depopulation either resonantly utilizing the longitudinal optical (LO)-phonon energy of the material or by miniband extraction.

2.5 Quantum cascade detectors (QCDs)

QCDs are unipolar intersubband MIR detectors, which offer a narrow band ($\leq 0.08\,\mathrm{eV}$) tuneable absorption wavelength [15, 16, 56]. QCDs stand out because of their high-speed detection [57], owed by sub-picosecond unipolar transitions. Additionally, due to their photovoltaic nature, they offer a low-noise working principle at room temperature.
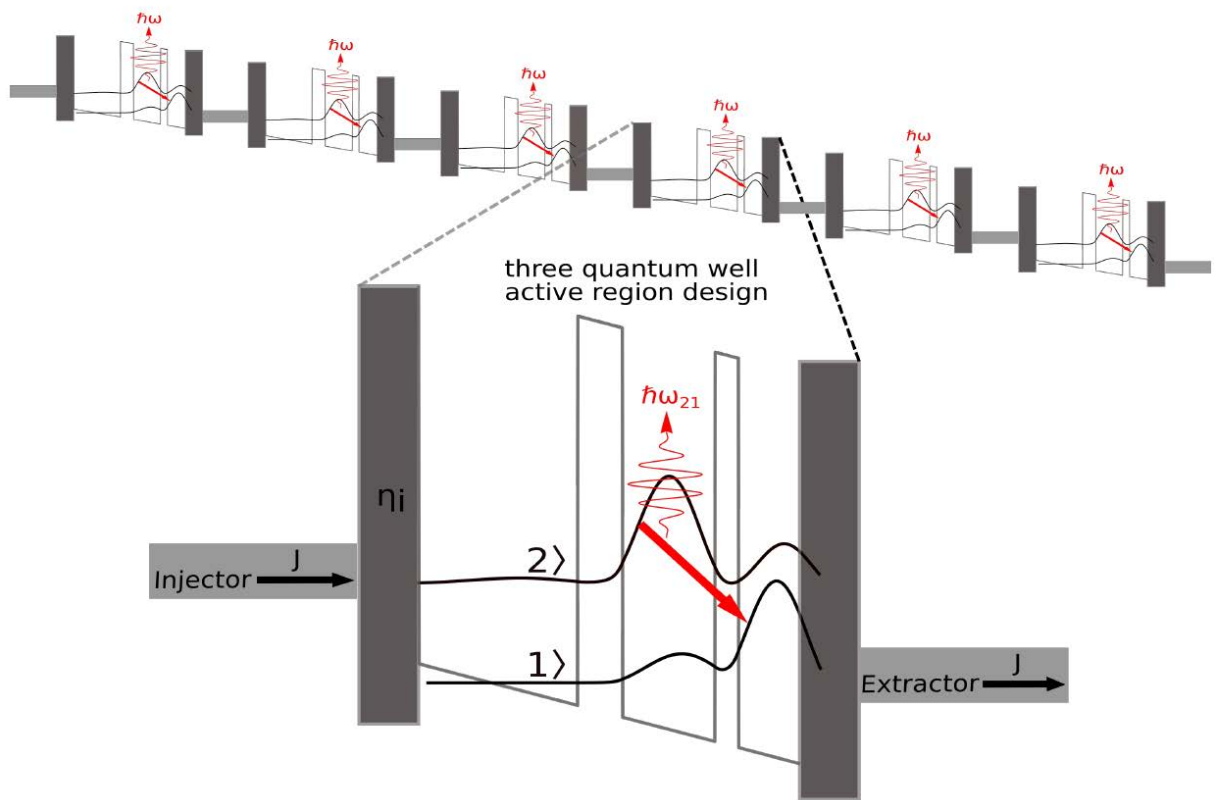
Figure 2.13: Sketch of the working principle of a QCL. Electrons are injected to the upper laser state $|2\rangle$, relax to the lower laser state $|1\rangle$ by emitting a photon, and are extracted fast. (Reprinted with permission from [54].)

2.5.1 Functioning principle

The absorption energy can be adapted within the CBO of the material system by the well width. The narrower the well, the further apart the levels and the higher the transition energy. The QCD is a unipolar design based solely on the conduction (or valence) band. The asymmetry of the band structure design allows for operation without an applied bias.

Fig. 2.14 depicts a typical QCD band structure with the squared probability densities. The red arrows mark the optical transition, which occurs from the ground state to the first excited state that either is in the same well (vertical transition) or in the next well to the right (diagonal transition). From there, the electrons are extracted with scattering rates in the sub-picosecond to the ground state of the next cascade (there are typically 15–30 cascades), where they have to absorb another photon to continue through the active region, and finally reach the contacts and contribute as current flow. A probability always exists that electrons relax or are backscattered and thus then do not contribute to the current flow. In the following figures of merit characterizing QCDs are given.
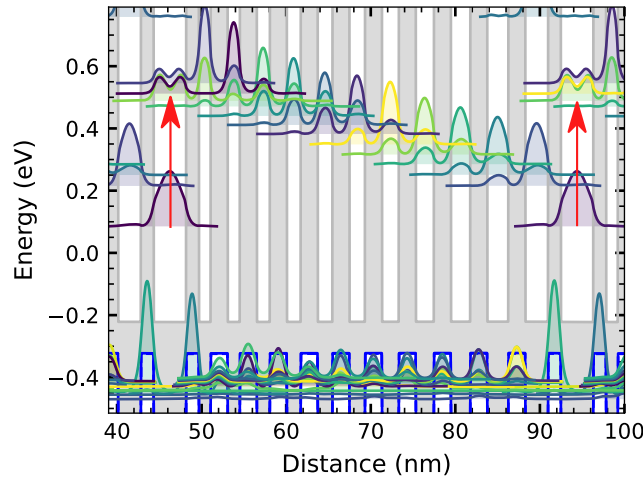
Figure 2.14: Typical InAs/Al(As)Sb QCD bandstructure. The conduction band is outlined in grey and the valence band in blue. The bandgap is filled in grey. The intersubband absorption is marked with red arrows. After the absorption, the electron follows an extraction ladder to the ground state of the next optical well.

2.5.2 Figures of merit

The performance of QCDs and photodetectors in general, is characterized by the responsivity, the specific detectivity, and the noise equivalent power (NEP), the input power that generates current equal to the noise [16, 25, 58].

Responsivity:

The responsivity is defined as the generated photocurrent under illumination I_p divided by the incident light intensity P_ω in units of (W), in other words, the input signal power.

$$R_p = \frac{I_p}{P_\omega} \tag{2.27}$$

For QCDs the responsivity is usually given in terms of absorption efficiency η_{abs}, which is defined by the fraction of photons absorbed by the desired optical transition. It is related to η, the quantum efficiency given by the fraction of generated electrons per incident photons, by

$$\eta = \eta_{abs}\eta_{int} \tag{2.28}$$

where η_{int} is the internal quantum efficiency, the fraction of generated electrons per absorbed photon [15]. It can be written as:

$$\eta_{int} = \frac{p_e}{N_p} \tag{2.29}$$

where p_e is the extraction efficiency defined as the probability that an electron that absorbed a photon by the desired optical transition contributes to the photocurrent, and N_p is the number of periods in the active region. For QCDs the responsivity can be written as [16]:

$$R_p = \frac{e\lambda\eta_{abs}p_e}{hcN_p} \tag{2.30}$$

Noise equivalent power (NEP):

QCDs are photovoltaic devices operated at zero bias, therefore, out of the several noise sources that exist for detectors, like $1/f$ noise, Johnson noise, dark current noise, and photon noise, their noise is dominated below the background limited performance temperature T_{BLIP} by photon noise and above by Johnson noise or thermal noise. This is given as [16, 58]:

$$i_n = \sqrt{\frac{4k_B T \Delta f}{R_0}} \tag{2.31}$$

where R_0 is the differential resistance, T the temperature, and Δf is the measurement bandwidth. From this, the noise equivalent power can be written as:

$$NEP = \frac{i_n}{R_p} \tag{2.32}$$

Specific Detectivity:

With this, the specific detectivity is the reciprocal of NEP and is defined as:

$$D^* = \frac{\sqrt{A\Delta f}}{NEP} \tag{2.33}$$

with A the optical area of the detector. In the Johnson noise limit the specific detectivity becomes [16]:

$$D_j^* = R_p\sqrt{\frac{AR_0}{4k_B T}} \tag{2.34}$$

Below T_{BLIP}, noise is generated due to the background blackbody radiation and the detectivity reads [16]:

$$D^*_{BLIP} = (\frac{R_p}{2e^2 g_p \int g_p p_e \eta_{abs} \frac{d\Phi_{BG}(f)}{df} df})$$ (2.35)

where $\frac{d\Phi_{BG}(f)}{df}$ is the spectral background photon flux density, and g_p is the photodetector gain, which is defined for QCDs as

$$g_p = \frac{p_e}{N_p p_c}$$ (2.36)

where p_c is the capture probability into the optical well ground state. D^*_{BLIP} is the maximum achievable detectivity value.

2.5.3 Optical coupling

As discussed in subsection 2.2.2 QCDs are only sensitive to light polarized in the growth direction. This has to be considered when attempting to couple light into a device.

45° facet double-pass configuration:
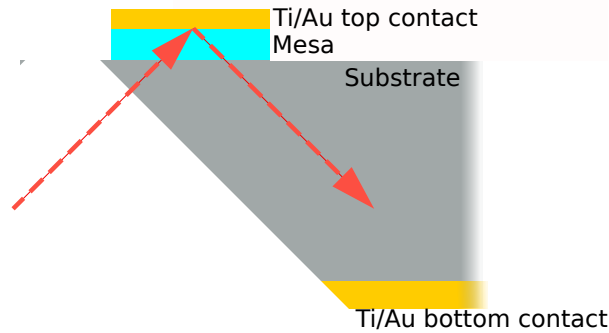
Figure 2.15: Sketch of the double-pass configuration with a 45° polished facet for light coupling. The light passes through the substrate and is reflected at the top Ti/Au contact of the mesa and passes through the mesa again with the opposite polarization.

A standard structure in literature for characterization of QCDs is the double-pass mesa with a 45° facet because it is relatively easy to process and thus robust and easy to reproduce [16], see Fig. 2.15. A facet under an angle of 45° degrees is polished onto the substrate. The facet is then oriented normally to the light source. The light is coupled through the substrate and is reflected at the mesa top-contact (thus double-pass). This geometry creates the requirement that the substrate has to be transparent in the desired characterization range. For a 30-period active region, the

total absorption of this structure is around $25\,\%$ and is therefore used for material and design characterization purposes, but is also a useful structure for comparisons to devices in literature.

With this method, only $50\,\%$ of the incoming light is polarized in the growth direction. The effective interaction length is $2\sqrt{2}d$, where d is the thickness of the active region.

Diffraction grating:

If it is necessary to top-illuminate a QCD, for example, if the substrate is opaque in the desired wavelength range, or if it is required by the device geometry, one of multiple possibilities is to fabricate a diffraction grating.
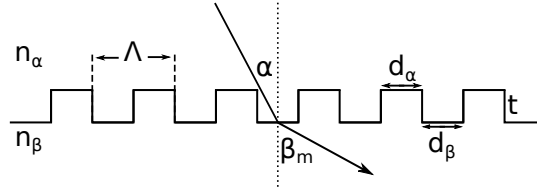
Figure 2.16: Sketch of a diffraction grating. Λ is the grating period, the duty cycle is d_α/d_β, t is the grating depth. n_α and n_β are the refractive indices of the two materials. α is the angle to the surface normal of the incoming plane wave and β_m is the diffracted angle of diffraction order m.

Such a grating is a variation in the refractive index, on the length scale of the wavelength, induced by a fabricated array of trenches onto the device. In Fig. 2.16, the grating period Λ, the grating depth t, and the duty cycle are sketched. An incoming planar wave under the angle α is diffracted to the angle β. A valid diffracted angle must follow the relation [59]:

$$n_\beta sin(\beta_m) - n_\alpha sin(\alpha) = m\frac{\lambda_0}{\Lambda} \tag{2.37}$$

where n_β, and n_α are the refractive indices of the two materials, m the diffraction order, and λ_0 the wavelength.

For diffraction order zero $m = 0$, it is described by Snell's Law

$$sin(\beta_0) = \frac{n_\alpha}{n_\beta}sin(\alpha) \tag{2.38}$$

The sin() function in eq. 2.37 can only vary between -1 and 1 and therefore requires that

$$-(n_\alpha + n_\beta) < \frac{m\lambda_0}{\Lambda} < (n_\alpha + n_\beta) \tag{2.39}$$

which has to be fulfilled for higher diffraction orders. With the Bragg condition for gratings, a condition for λ_B can be found

$$\lambda_B = \frac{2\Lambda n_{eff}}{m_g} \tag{2.40}$$

where m_g is the grating order and n_{eff} the effective refractive index defined as

$$n_{eff} = \frac{n_\alpha d_\alpha + n_\beta d_\beta}{\Lambda} \tag{2.41}$$

where d_α and d_β are the ridges and trenches, respectively.

2.5.4 State-of-the-art QCDs

Over the years since the first demonstration in 2002 [60, 61], QCDs were realized with absorption spectra from the near-infrared [62] (1.7 μm) to the longer far-infrared (19 μm) [63] and even THz regime (2 THz, 150 μm) [64]. These were implemented in various material systems from mature GaAs/AlGaAs [65] and InGaAs/InAlAs [66] with CBOs of 0.2–0.5 eV, to nitride-based materials like GaN/AlN with a CBO of 1.8 eV [25] and II-VI semiconductors [67]. Most reports on QCDs were grown in the InGaAs/InAlAs material system lattice matched to InP. In this material system, more complex fabrications were realized, like pixel array configurations [68], photonic crystal slabs [69], QCDs enhanced by surface-plasmons [70], and single-period devices [71].

The wide spectral operation range of QCDs also allows for applications in chemical sensing [72], image sensing [73], and free-space optical communication [74]. QCDs are also implemented as high speed detectors [57], reaching a 3-dB cutoff at 20 GHz with an operation beyond 50 GHz. These detectors are virtually insaturable, even with Watts of input power [15, 75]. High-speed, paired with a widely tailorable spectral response, will allow for operation in demanding applications like real-time spectroscopy of chemical reactions [76]. Further, high speed QCDs are employed in frequency comb research [77].

Due to the close relationship of QCDs with QCLs, bi-functional devices working as QCL and QCD have been realized [12, 78]. For this approach, the functionality of the laser and detector was monolithically implemented into one active region emitting and detecting at the same energy.

Due to the intersubband optical transitions, QCDs have a lower peak responsivity compared to competing detectors, see subsection 2.5.5. Devices based on InGaAs/AlGaAs, processed in the standard 45° facet configuration reach a room temperature responsivity of around 10 mA/W [68]. On the other hand QCDs excel in detectivities

on the order of 10^{10} Jones at room temperature [79].

With the availability of affordable, high-quality InAs and GaSb substrates, the advantageous intrinsic material properties, like a low effective electron mass of the well material or a high CBO of the InAs/Al(As)Sb material system can now also be used for QCDs [80] to improve the responsivity and establish efficient short wavelength infrared QCDs [81].

2.5.5 Competing detectors to QCDs

QCDs are closely related to the more established quantum well infrared photodetectors (QWIPs) [58], the competing intersubband technology, employing bound-to-continuum state transitions. QWIPs have been fabricated in a wide spectral range and reach high-speed operation, up to 110 GHz has been reported [82]. QWIPs typically require cooling and an applied bias, which increases the dark noise and therefore lowers the detectivity, especially at elevated temperatures. These detectors have reached responsivities and detectivities on the order of multiple 100 mA/W and 10^6 Jones, respectively [83, 84].

On the other hand, QCDs are fundamentally different than other classes III-V heterostructure photo-detectors like interband devices, where optical absorption occurs between the valence and conduction band [85]. These include type-II and other superlattice detectors. As discussed above in subsection 2.2.1, the density of states of such transitions has a cut-on but no strict cut-off. Therefore, these detectors offer broad-band absorption (exceeding 2 eV - compare to the 0.08 eV bandwidth of QCDs [15]) with high responsivities (> 100 mA/W [86]). They excel mostly in the wavelength range between the visible and mid-infrared. Furthermore, these devices often require cooling [85], although recent devices work at room temperature at zero bias up to 5 μm [87]. In contrast to the self-passivated behavior of intersubband devices, interband devices are sensitive to surface effects [15], complicating fabrication. Type-II superlattice detectors have reached a 3-dB bandwidth of up to 7.04 GHz [87].

2.6 Optical characterization

The QCDs presented in this thesis were characterized with an Fourier-transform infrared spectrometer (FTIR) using a Globar broadband MIR source. An FTIR is often based on a Michelson-interferometer. The beam coming from an often broadband source is split by a beam splitter, where one part is reflected by a fixed mirror and the other part by a moveable mirror. The two beams are brought together again where they interfere, based on their difference in optical path length, and the

signal is measured with a detector. This way, per moveable mirror position, some wavelengths contained in the beams will positively interfere while others negatively interfere. With this method, an interferogram is obtained, which is then calculated back to a spectrum.
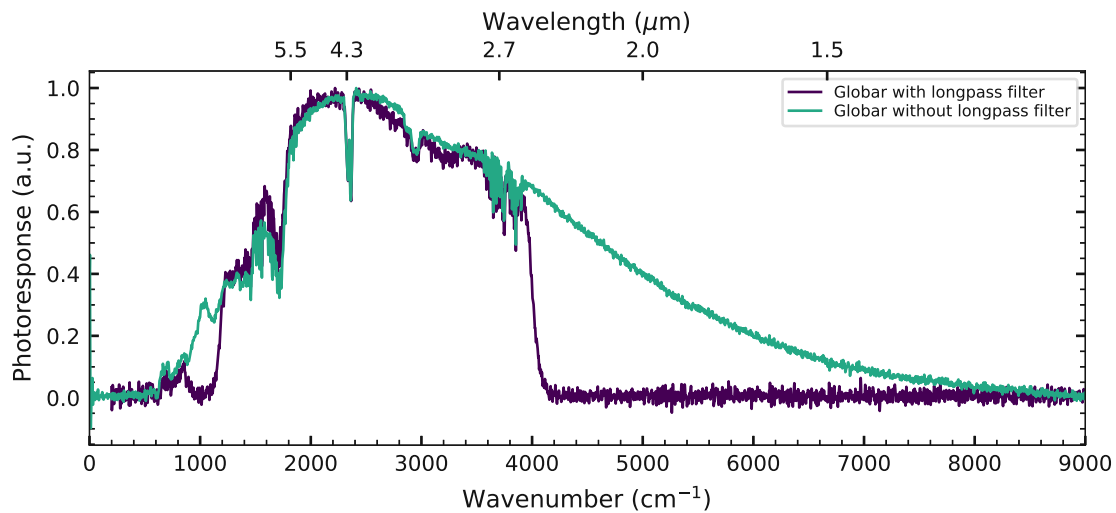
Figure 2.17: The Globar spectrum is plotted with a focusing ZnSe lens before the Ophir detector. For one measurement additionally, a long pass filter was in the beam path with a specified cut-on wavelength of 2.4 µm, 4166 cm^{-1}.

Fig. 2.17 shows the spectral response of the Globar, with the highest signal around 4.3 µm and a decline towards higher and lower energies.

In the following, it is discussed how the different figures of merit of QCDs were measured.

2.6.1 Spectral response

For this thesis, a Bruker Vertex 70v FTIR was used together with a transimpedance amplifier. The FTIR can operate in two modes. In the free-running mode, the moving mirror continuously changes position. This mode can be employed if the detector and the used electronics have a suitable response time, external modulation times must be large compared to the mirror moving time. For QCDs the response time is not an issue. Usually, in the free-running mode is it averaged over a lot of recorded spectra to reduce the noise. If the detector signal is too low, a lock-in amplifier can be utilized to further reduce the noise, and employing the step-scan mode of the FTIR, where the moving mirror is moved to fixed locations before a measurement is taken. This mode of operation takes considerably longer than the free-running mode.

2.6.2 Responsivity

As already defined in subsection 2.5.2, the responsivity is given as the generated photocurrent by the detector under illumination divided by the incident light intensity, see eq. 2.27. The photocurrent was obtained by measuring the electrical output current of a QCD under aligned illuminated conditions, as well as under dark conditions. The dark current was then subtracted from the current under illuminated conditions to account for dark noise. The current was measured with a Keithley SourceMeter source measure unit.

The incoming light intensity was measured for the exact same setup the QCD was measured in, with an Ophir detector, and is typically around 5 mW for the entire beam spot, where the aperture of the Ophir detector is large enough to capture the entire beam spot. To obtain the fraction of the power that was impinging on the mesa of a QCD, which is typically around $100 \times 100\,\mu m$ in size the intensity profile of the beam spot of the setup was measured. This was done by xy-measurements of a $50 \times 50\,\mu m$ mesa, see Fig. 2.18.
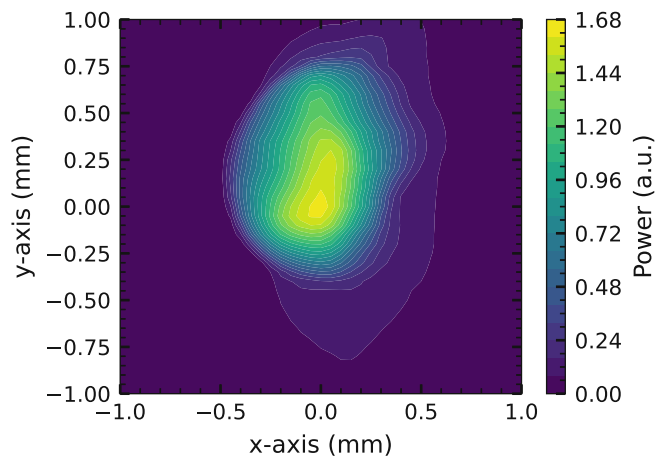
Figure 2.18: Globar beam spot measured with the same setup as for QCDs. This is created from an xy-scan with a $50 \times 50\,\mu m$ QCD.

To obtain the beam profile and intensity on the mesa, it was assumed that the detector was aligned to the maximum intensity of the beam spot. Now, the power impinging on the mesa is obtained by integrating the beam spot intensity profile over the area of the mesa at the location of the maximum intensity of the beam spot profile. The integral of the Globar spectral density function over all frequencies is then the illumination power on the mesa. The unpolarized light of the Globar is taken into account by a factor of two in the calculations, due to the fact that QCDs are only sensitive to one polarization. The total current of the QCD under

illumination minus the dark current is the integral over the detector spectral response. Finally, the responsivity of the QCD is obtained with eq. 2.27. If the mesas were measured inside a cryostat the shadowing of the cryostat and the transmission of the cryostat window has to be taken into account with a correction factor.

The measured QCDs during this thesis had comparably high resistance due to the large CBO and their high-energy optical transitions. If the QCD resistance is on the order of the input resistance of the transimpedance amplifier, additional measures need to be taken, see [88].

2.6.3 Detectivity

The detectivity of a QCD is obtained with eq. 2.34 after the measurement of the responsivity. The differential resistance is obtained by I-V measurements around $0\,\mathrm{V}$.

Growth and analysis

3.1 Crystal structures

Solids exist in different phenotypes, such as amorphous (e.g. glass), polycrystalline, or single crystalline. For high-performance devices, semiconductor technology is dependent on high-quality single crystalline materials.

The definition of a perfect crystal is an infinitely repeating structure built from identical structural elements. It consists of a basis (of one or more atoms) plus a crystal lattice. In the 3-D room, there are 14 possible crystal lattices with translation symmetry, which were defined by Bravais. These Bravais-lattices follow the relation [27]:

$$\mathbf{R} = n_1\mathbf{a}_1 + n_2\mathbf{a}_2 + n_3\mathbf{a}_3 \tag{3.1}$$

where $\mathbf{a}_1$, $\mathbf{a}_2$, and $\mathbf{a}_3$ are vectors (in the x-, y-, and z- direction but not necessarily orthogonal) and n_1, n_2, and n_3 are integral numbers. Except for translation symmetry, crystal lattices can also exhibit rotational-, mirror-, and inversion symmetry, as well as compounds of these symmetries. Given the existence of additional symmetries, crystal lattices are categorized into seven crystal systems, each containing one or more of the 14 Bravais lattices. A good introduction to crystals and solid state physics can be found in [27], a book more specialized to semiconductors is [33].

III-V semiconductors crystallize, like many elements, in one of the following two Bravais lattices, which belong to the most important crystal lattices, therefore they will be briefly introduced:

Face centered cubic (FCC):
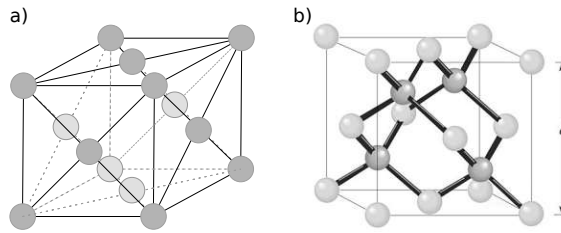
Figure 3.1: a) Face centered cubic crystal structure. b) Zinc Blende crystal structure composed out of an fcc structure with two different atoms in the basis. (Reproduced with permission of Cambridge University Press through PLSclear [33].)

Fig. 3.1 a) depicts an FCC lattice. The unit cell consists of four atoms found at (0,0,0), (0, 1/2, 1/2), (1/2,0,1/2), and (1/2,1/2,0). A prominent example with two (equal) basis atoms is the diamond structure, in which C but also Si or Ge crystallize. If the two basis atoms are not the same kind, the crystal lattice is called Zinc Blende, see Fig. 3.1 b). This is one of the most important crystal structures in III-V semiconductors, as As-, P-, and Sb-based III-V semiconductors crystallize in this crystal lattice. It exhibits the highest possible packing fraction in 3-D crystal lattices of $F_{fcc} = \frac{\pi}{3\sqrt{2}} \approx 0.740$.

Hexagonal close packed (HCP):
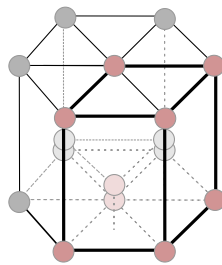
Figure 3.2: Hexagonal close packed crystal structure. The unit cell is emphasized.

Fig. 3.2 depicts an HCP crystal lattice. One unit cell is emphasized by red spheres. It can be constructed from the hexagonal Bravais lattice with a basis of two (or more) identical atoms. In the Wurtzite structure, in which important III-nitride semiconductors like GaN or AlN, but also ZnO crystallize, the two basis atoms each form an hcp lattice, respectively. The HCP lattice also exhibits the highest possible packing fraction for 3-D crystal lattices of $F_{hcp} = \frac{\pi}{3\sqrt{2}} \approx 0.740$.

3.1.1 Miller indices

A crystal plane can be defined by its intersection with the three crystal lattice vectors in units of the lattice constants $\mathbf{a}_1 n_1$, $\mathbf{a}_2 n_2$, and $\mathbf{a}_3 n_3$ [27]:

$$h = \frac{p}{n_1}, k = \frac{p}{n_2}, l = \frac{p}{n_3} \tag{3.2}$$

p is the smallest integer number that makes h, k, and l prime numbers. With this definition all parallel planes in a crystal are defined by the same triple of indices. The triple (hkl) is called Miller indices.

Indices u,v, and w of directions in crystals are then given in square brackets. They are defined as the smallest numbers with the same ratio as the components of the vector $\mathbf{R} = u\mathbf{a_1} + v\mathbf{a_2} + w\mathbf{a_3}$ that points in the same direction, given in units of the lattice constants [27]. For example, the normal vector to the crystal plane (hkl) is given by [hkl].

3.1.2 Reciprocal lattice

The reciprocal lattice is built up from the reciprocal lattice vectors $\mathbf{g}_1$, $\mathbf{g}_2$, and $\mathbf{g}_3$, which are defined in the following way:

$$\mathbf{g}_1 = 2\pi \frac{\mathbf{a}_2 \times \mathbf{a}_3}{\mathbf{a}_1(\mathbf{a}_2 \times \mathbf{a}_3)}, \mathbf{g}_2 = 2\pi \frac{\mathbf{a}_3 \times \mathbf{a}_1}{\mathbf{a}_1(\mathbf{a}_2 \times \mathbf{a}_3)}, \mathbf{g}_3 = 2\pi \frac{\mathbf{a}_1 \times \mathbf{a}_2}{\mathbf{a}_1(\mathbf{a}_2 \times \mathbf{a}_3)} \tag{3.3}$$

The reciprocal lattice is the Fourier transform of the real space lattice. This concept is important for the analysis of crystals, as some analysis methods rely on diffractions of the crystal planes, which then yield a pattern in the reciprocal space.

3.1.3 Defects in single crystals
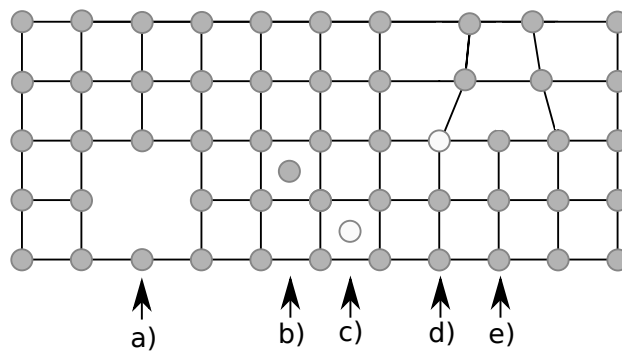
Figure 3.3: Sketch of defects and dislocations in a crystal. a) vacancy, b) interstitial atom, c) interstitial foreign atom, d) substitutional atom, e) edge dislocation.

Defects are differentiated by their dimensionality. In Fig.3.3 some defects and dislocations which are discussed below are sketched.

Point defects:

Point defects can be intrinsic or extrinsic, for extrinsic defects foreign atoms are involved. They can be vacancies, interstitial, or substitutional atoms. For example, doping semiconductors with Si atoms extrinsically produces point defects.

Line defects:

Line defects are edge dislocations or screw dislocations. Dislocations always form a loop or end at a surface. They are characterized by the Burgers vector **b** which gives the magnitude and direction of the dislocation. Threading dislocations and misfit dislocations, two common dislocations in III-V heterostructure growth, always have an edge- and a screw dislocation component. Only the edge component of a misfit dislocation releaves strain.

3.2 Epitaxy

Epitaxy is the growth of single crystalline thin layers on single crystal substrates, where the orientation of the grown layer is well-defined. Additionally, a critical misfit value of the lattice parameters of substrate and layer in the growth plane is not surpassed [89]. In the simplest case, this criterion is achieved by growing material A on a substrate of material A, which is then called homoepitaxy. If material B, which fulfills the criteria is grown on material A it is called heteroepitaxy. Fig. 3.4 shows the bandgap of important III-V semiconductors plotted over the lattice parameters.

During this Ph.D., heterostructures of the following material systems were grown and studied:

GaAs/Al$_x$Ga$_{1-x}$As on GaAs substrates:

This material system offers a minimal lattice mismatch between GaAs and AlAs of 0.145%. The height of the barriers can be adapted by increasing the Al content and because sufficient lattice matching is automatically fulfilled, the growth rates can be determined precisely. This material system is used for the growth of THz quantum cascade lasers (QCLs) due to its maturity and ease of growth. Depending on the Al content in the AlGaAs barriers the conduction band offset (CBO) ranges from 148–357 (15–45% Al), and the effective electron mass of GaAs is $0.0675\,\mathrm{m_0}$ [25].
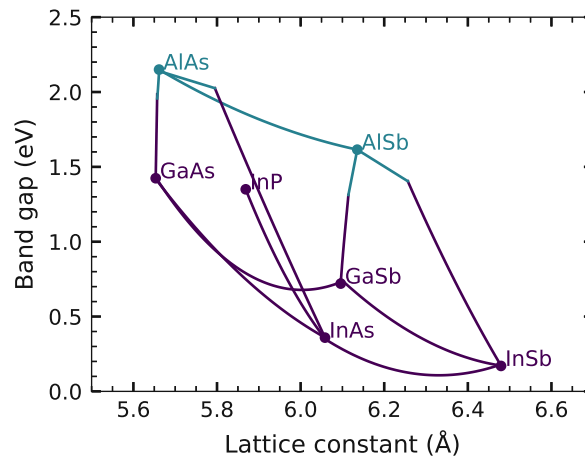
Figure 3.4: Band gap vs. lattice constant for zinc-blende III-V semiconductors. Purple colored are direct band gaps and turquoise indirect band gaps. Ternary alloys are indicated by the lines connecting the binary alloys.

InGaAs/InAlAs on InP substrates:

This system is grown lattice-matched to InP substrates. It is one of the main material systems that is used for quantum cascade detectors (QCDs) and QCLs, due to its higher CBO of $0.5292\,\text{eV}$ in the lattice-matched case. The effective electron mass of InGaAs is $0.043\,\text{m}_0$ [25].

InAs/AlAs$_{0.16}$Sb$_{0.84}$ on InAs substrates:

This material system is grown lattice-matched to InAs substrates. Its material properties, such as a high CBO of $2.28\,\text{eV}$ and a low effective electron mass of $0.026\,\text{m}_0$ benefit QCD optimization [25]. The mixed group-V barrier makes this growth more challenging.

InAs/AlSb on GaSb substrates:

This system is grown strain balanced to GaSb substrates. It offers the same benefits as the InAs-based material system and additionally, it offers transparency of the GaSb substrate up to $0.812\,\text{eV}$ ($1.52\,\mu\text{m}$)[25].

3.2.1 Strain in thin films

In heteroepitaxy, two different materials are brought together to form a heterostructure single crystal. If the materials are not exactly lattice-matched (which is almost never the case, even when lattice-matching is possible), the mismatch in lattice

parameters will cause elastic strain, because the atoms of the grown film are forced to align with the substrate atoms. Additionally, a thermal expansion mismatch exists. Strain can cause the band structure to change and induces defects. Following [90], mathematically strain and stress can be expressed by Hooke's law, which simplifies for cubic lattices to:

$$\sigma = C\epsilon \tag{3.4}$$

where the full relation is

$$\begin{pmatrix} \sigma_{xx} \\ \sigma_{yy} \\ \sigma_{zz} \\ \sigma_{yz} \\ \sigma_{zx} \\ \sigma_{xy} \end{pmatrix} = \begin{pmatrix} C11 & C12 & C12 & 0 & 0 & 0 \\ C12 & C11 & C12 & 0 & 0 & 0 \\ C12 & C12 & C11 & 0 & 0 & 0 \\ 0 & 0 & 0 & C44 & 0 & 0 \\ 0 & 0 & 0 & 0 & C44 & 0 \\ 0 & 0 & 0 & 0 & 0 & C44 \end{pmatrix} = \begin{pmatrix} \epsilon_{xx} \\ \epsilon_{yy} \\ \epsilon_{zz} \\ \epsilon_{yz} \\ \epsilon_{zx} \\ \epsilon_{xy} \end{pmatrix} \tag{3.5}$$

where σ is the stress tensor, ϵ the strain tensor, and C the stiffness matrix. One can assume that the stress in the growth direction is zero, for growth in the z-direction equal strain in the growth plane xy is present:

$$\sigma_{xx} = \sigma_{yy} = \sigma_{||} \tag{3.6}$$

This form of stress is called biaxial stress. Now the grown cubic crystal becomes tetragonal. This is therefore called tetragonal distortion:

$$\epsilon_{||} = \epsilon_{xx} = \epsilon_{yy} = \frac{a - a_0}{a_0}, \epsilon_{\perp} = \frac{c - a_0}{a_0}. \tag{3.7}$$

where a is the strained in-plane lattice constant, a_0 the relaxed lattice constant of the thin film, and c the out-of-plane lattice constant.

The $\epsilon_{||}$ and $\epsilon_{\perp}$ strains are related by

$$\epsilon_{\perp} = -\frac{2C_{12}}{C_{11}}\epsilon_{||} \tag{3.8}$$

A layer under biaxial stress is called pseudomorphic. One can relate the strain to the stress in the following way:

$$\sigma_{||} = (C_{11} + C_{12} - \frac{2C_{13}^2}{C_{33}})\epsilon_{||} \tag{3.9}$$

A lattice mismatch can cause either compressive or tensile strain, depending if the lattice constant of the grown layer is larger or smaller than that of the substrate, see

Fig.3.5.
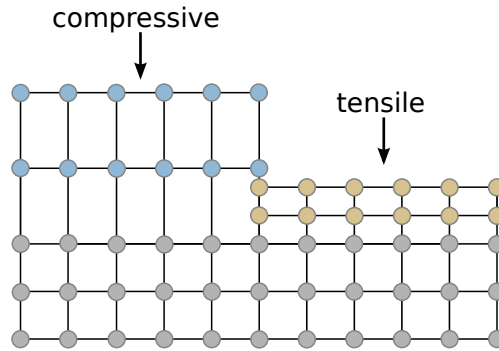
Figure 3.5: Sketch of a crystal lattice with compressive and tensile stress.

This distortion introduces strain energy into the layer, and therefore the layer is expected to relax at some critical energy value. The critical layer thickness is the thickness where the strain energy gets larger than the energy that is necessary to relax the layer. At this point, a misfit dislocation is generated, and thus relaxing the layer becomes energetically favorable.

A conservative estimate of critical layer thickness can be calculated with the formula by Matthews and Blakeslee [91]:

$$x = \frac{\mathbf{b}}{2\pi * m * (1 + \nu)} \ln(\frac{x}{\mathbf{b}} + 1) \tag{3.10}$$

where $\mathbf{b}$ is the Burgers vector of the grown layer, m the misfit to the substrate, and ν the Poisson ratio, given by

$$\nu = \frac{C_{12}}{C_{11} - C_{12}} \tag{3.11}$$

In Fig. 3.6 the critical layer thickness for a few material systems are calculated.

As mentioned, epitaxial films can be grown lattice-matched or strain balanced to the substrate. Strain balancing can be achieved by growing sub-critical-thickness layers of two materials whose strain energy balances each other on the substrate lattice parameter. This is done, for example, with InAs/AlSb grown on GaSb. These two materials have almost opposite mismatches to GaSb of 0.62063 % for InAs and -0.64542% for AlSb.

3.3 Doping in III-V semiconductors

Doping is defined as altering the electrical properties of a crystal. It is done by deliberately adding impurities, which, in the ideal case, then occupy substitutional
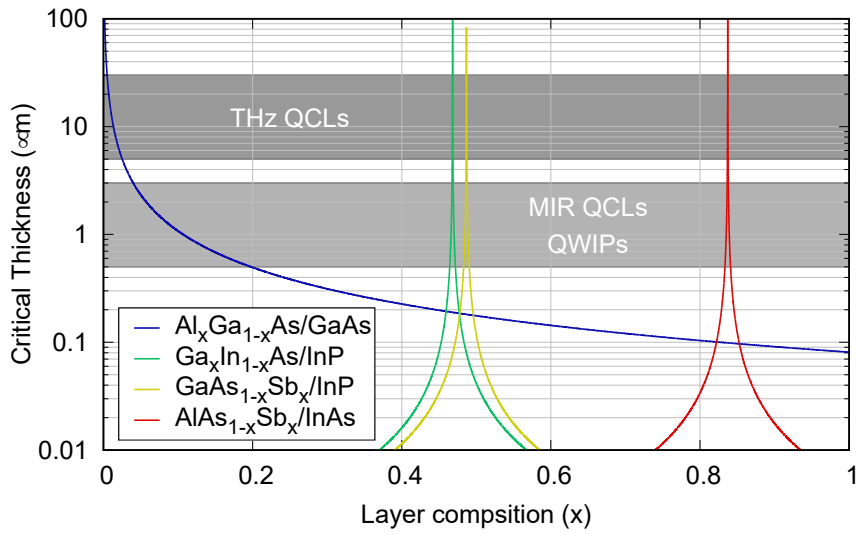
Figure 3.6: Calculation of critical layer thicknesses for important III-V semiconductor materials for THz QCLs and mid-infrared QCDs. The calculation was done with a refined version of eq. 3.10, see [92]. (Reprinted with permission from [93].)

lattice sites, and provide free carriers for electrical conductance. The Bohr radius of such dopants can exceed $100\,\text{Å}$. Such impurities are ideally ionized at room temperature due to low activation energy and are then called shallow impurities or dopants [94]. They can donate electrons, which makes the matrix material n-type (donors), or holes, which makes it p-type (acceptors). For III-V semiconductors, dopants can be selected from groups II, IV, or VI. Group-II dopants such as Be would occupy group-III sites and act as acceptors and group-VI dopants would occupy group-V sites and act as donors. The most prominent dopant for III-V semiconductors is Si. Due to its position in group-IV, it can occupy either a group-III site and act as a donor or the group-V site and act as an acceptor. This behavior is called amphoteric. A result of the amphoteric behavior of group-IV elements is that depending on the growth conditions they self-compensate. This means that dopants occupying the group-V sites and therefore acting as acceptors partially compensate the donors from the group-III sites. Si is a popular donor because it mostly occupies group-III sites and has an ionization energy of 4–$6\,\text{meV}$ whereas the Si acceptor ionization energy is $35\,\text{meV}$ in GaAs [94]. The Si doping concentration exhibits a saturation at about $5\times10^{18}\,1/\text{cm}^3$, because starting from this threshold Si acceptors at group V sites drastically increase. The saturation depends on the growth conditions, specifically on the growth temperature, the group-III/group-V flux ratio, and whether As_2 or As_4 is used.

Above critical doping concentrations ($1\times10^{19}\,1/\text{cm}^3$) effects such as the Mott-transition, the Burstein-Moss Shift, impurity bands, band gap narrowing and more

occur, which are described in [94].

Another dopant used during this thesis is Te, which is evaporated from GaTe, due to its high vapor pressure. This makes its incorporation also highly temperature dependent. Te has an ionization energy of 30 meV in GaAs, which is rather high compared to Si [94]. It is used as a dopant in Sb-compounds where Si exhibits a strong amphoteric behavior.

3.3.1 Diffusion of Dopants

At sufficiently high temperatures, dopant atoms can diffuse from their original (desired) location. The diffusion length L_D can be calculated from the equation:

$$\sigma_{Diff} = \sqrt{2}L_D = \sqrt{2Dt} \tag{3.12}$$

where σ_{Diff} is the standard deviation of the Gaussian distribution, D the diffusion constant, and t the time. The full width at half maximum (FWHM) is given at FWHM $\approx 2.355\,\sigma = 2.355\sqrt{2Dt}$ [94].

Luckily, Si has a rather low diffusion constant compared to other dopants, with $D = 1 \times 10^{-18}$ cm^2/s at 600°C in GaAs and doping in the 1×10^{18} 1/cm^3 range [95]. This results after 48 h at growth temperature in a diffusion of approx. 9 nm. Still, the Si diffusion is considered for in molecular beam epitaxy (MBE) device growth and counteracted by shifting the doping inside the well away from the barriers [38].

3.3.2 Donor-complex (DX)-centers

Donor complex (DX)-centers are deep traps generated from Si, Te, etc. atoms in Al$_x$Ga$_{1-x}$As layers with $0.2 \geq$ x ≥ 0.4 [94, 96]. Studies [97, 98] suggest that DX-centers are frozen out below 150 K and are not fully ionized even at 300 K, with a thermal activation energy of 135 meV. Studies also found that the DX-center concentration increases with Al-fraction in the barriers, while the shallow donor concentration decreases[94]. As a result, it is attempted not to dope AlGaAs barriers.

3.4 Molecular beam epitaxy of III-V semiconductors

MBE is one of the two main techniques that yield the utmost control of growth conditions, high material quality, and purity to achieve growth accuracy and reproducibility. The possible single crystal film morphologies range from quantum dots to nano-wires to surfaces with low surface roughness [99].

In the following, aspects that distinguish MBE technology from other growth techniques, the growth mechanisms, and kinetics are introduced.

3.4.1 Molecular beam epitaxy (MBE) technology
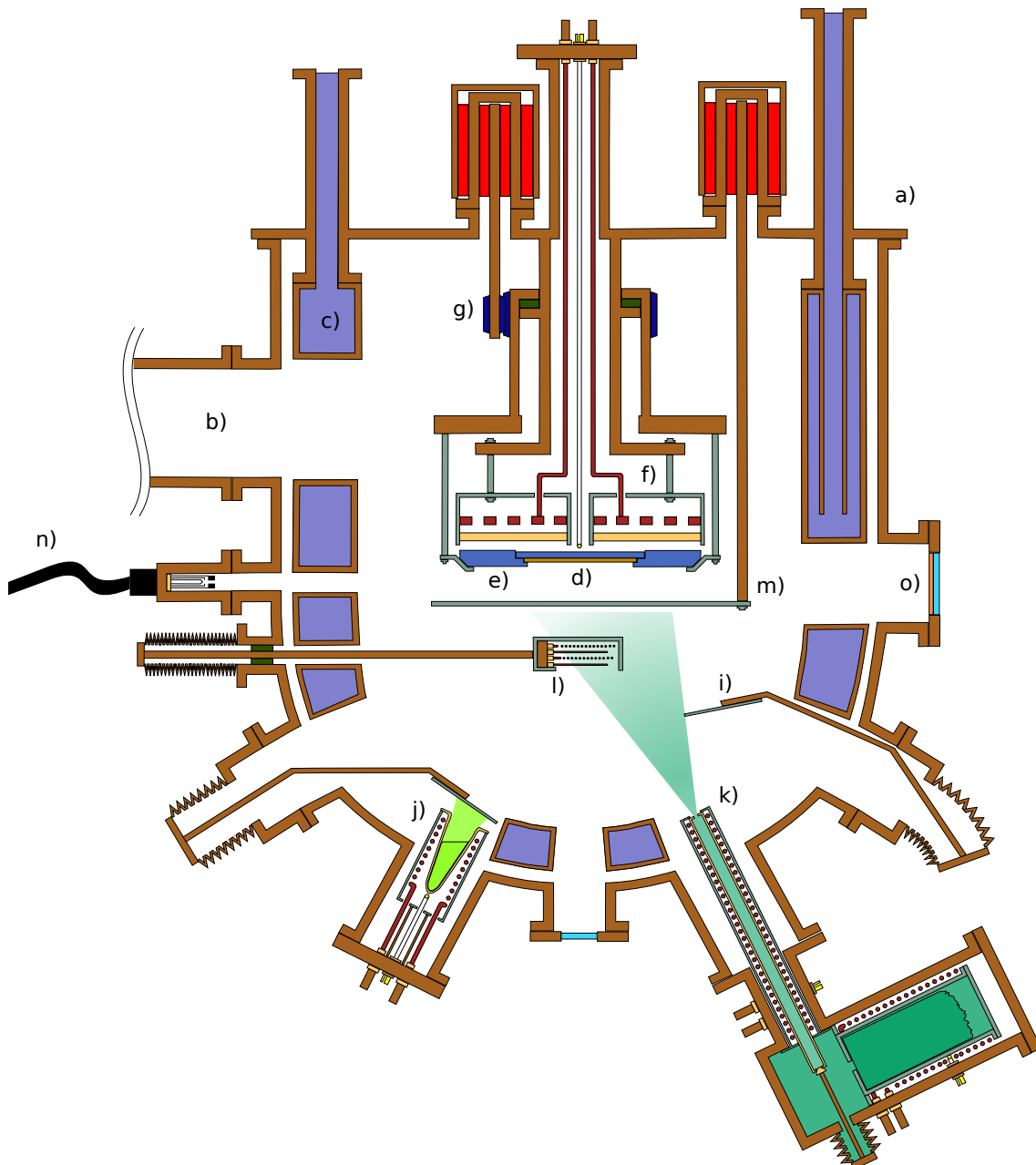
Figure 3.7: Sketch of a Riber C21 MBE chamber. The single elements are described in the text. (Reprinted with permission from [93].)

Fig. 3.7 shows an illustration of a cut through the center of a round MBE. a) The vacuum chamber is operated in ultra high vacuum (UHV) conditions, which is achieved by several pumps: b) a closed-cycle helium cryo pump, an ion getter

pump, and a titanium getter pump. c) Additionally, the chamber is equipped with a hollow shroud that runs along the inner chamber side walls, which is filled with liquid nitrogen. With the help of these pumps, the system reaches a background pressure of 10^{-10} Torr. d) The substrate is in the center of the chamber and faces downwards. It is held by a platen with cut-outs either for full, half, quarter wavers, or square pieces. It is also possible to mount any desired shape with In-bonding on holders with no cut-outs. f) The substrate is heated to the desired growth temperature by the substrate heater, which is on the backside of the substrate. A floating thermocouple controls the heater temperature. g) The substrate is rotated to guarantee homogeneous heat distribution but more importantly homogeneous growth. h) The substrate temperature itself is monitored by pyrometers through a chamber window. i) The flux to the substrate is controlled with shutters. j) These are in front of effusion cells. These cells must have precise control loops for stable temperatures, especially during operation, when shutters open and close, see section 3.7, which are usually measured at the base and tip of crucibles, which, depending on the material, are usually out of pBN. k) Cracking cells are used for sublimating group-V materials like As or Sb. They have a cracking zone where the As_4 or Sb_4 molecules, which sublimate as tetramers can be cracked into dimers or monomers. l) The beam equivalent pressures of the cells can be measured with an ion gauge, which can be moved in front of the cells. m) The substrate is also protected by a main shutter. In-situ measurements of the growth quality are possible with a reflection high energy electron diffraction (RHEED) set up in the chamber, see section 3.5.1. n) An electron gun emits electrons under a grazing angle to the substrate where they are diffracted off the surface onto o) a phosphorescent screen where they display a diffraction pattern.

Vacuum requirements:

UHV conditions are needed for epitaxy for multiple reasons [99, 100]. First, to keep the purity of the source material in the cells. Impurities or oxidation alters the device properties and in the worst case can lead to highly insulating or unintentionally doped layers, making devices unusable. A characteristic for MBE is the growth rate of around $1\,\mu m/h$, or one monolayer per second, making the growth vulnerable to impurity incorporation. The MBE chamber needs to keep a background doping that should be much lower than the intentional doping, which starts at $5\times10^{15}\,1/cm^3$. For this purpose, the grower needs to be able to control the composition and doping of the grown layer precisely, see below. A general equation taking into account the sticking coefficient s_i at growth temperature, the impingement rate w_i, the growth

rate r_g, and the concentration of impurities in the flux n_i, where i is the material species, can be written as [100]:

$$n = \sum_i \frac{s_i w_i}{r_g} \tag{3.13}$$

and w_i is given as:

$$w_i = p_i \sqrt{\frac{N_A}{2\pi k_B M_i T}} \tag{3.14}$$

where N_A is the Avogadro constant, T is the temperature, and M_i is the molecular weight of the gas species. The condition for sufficiently clean layers is:

$$t_1(b) = 10^{-8} t_1(v) \tag{3.15}$$

where $t_1(b)$ and $t_1(v)$ are the monolayer deposition times of the beam and residual gas vapor.

The second important parameter is the mean free path length of the system, the distance a particle can travel between collisions. A characteristic of MBE is the operation in the molecular flow regime, which is defined as the mean free path being much longer than the diameter of the chamber. This requirement is necessary to guarantee no interactions between the growth species itself or the residual gas during its travel to the substrate. The mean free path L of the gas molecules can be written depending on the temperature T, the pressure p, and the molecular diameter d, as [100]:

$$L = \frac{k_B T}{\sqrt{2}\pi p d^2} \approx 3.11 \times 10^{-24} \frac{T}{p d^2} \tag{3.16}$$

Evaporation sources:

Above, the importance of pure materials was discussed, another equally important factor for film quality is the uniformity over the wafer and the layer-to-layer reproducibility, which depends on the long-term flux stability, as well as the flux variations from shutter operations, see section 3.4.2. As mentioned above, two types of evaporation sources are usually utilized in MBE systems for group-III cells, which are evaporated, and for group-V cells, which are sublimated.

For evaporation from a large isothermal enclosure with an equilibrium pressure p_{eq}, with a small orifice, and infinitely thin-walled to eliminate scattering, the number N_e of molecules evaporating from an orifice area A_e during the time t is given by the Knudsen equation [100]:

$$\Gamma_e = \frac{dN_e}{dt} = A_e(p_{eq} - p_v)\sqrt{\frac{N_A}{2\pi M k_B T}}\left(\frac{molecules}{s}\right) \tag{3.17}$$

where p_v is the vacuum pressure. This type of cell is called Knudsen cell. Real effusion cells in MBE systems do not fulfill the condition of a small orifice and an isothermal enclosure with equilibrium pressure since the cells are either cylindrical or conical. Therefore, this equation can just be considered as an approximation. Nevertheless, the above equation gives the correct dependency on the pressure p_{eq} and temperature T. The beam equivalent pressures plotted over the inverse temperature are shown for group III and group V materials in Fig. 3.8.
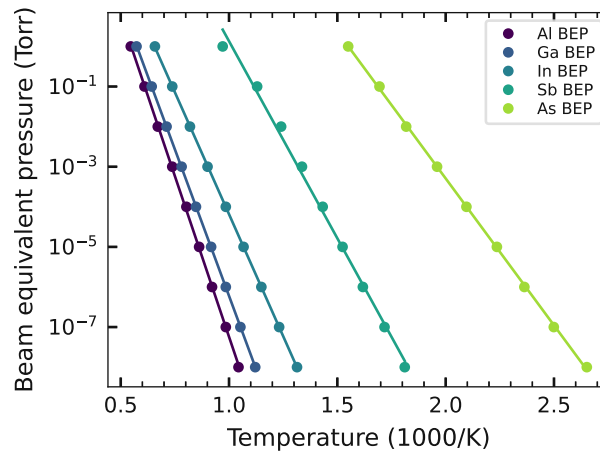
Figure 3.8: Vapor pressures for group III and group V elements used. Data from [101].

The uniformity of the deposited film also depends on the position of the cell relative to the substrate [100]:

$$d\Gamma_\theta = \frac{\Gamma_e}{\pi}cos\theta d\omega \tag{3.18}$$

which is the so-called cosine law of emission, with the differential angular effusion rate $d\Gamma_\theta$. With this one can calculate the flux I_A at a central point A where $\theta = 0$ and ϕ is the tilt of the source against the surface normal:

$$I_A = \frac{\Gamma_e}{\pi r_A^2}\cos\phi \tag{3.19}$$

where r_A is the distance to point A. The flux at at the edge point B is given by:

$$I_B = \frac{\Gamma_e}{\pi r_B^2}cos\theta cos(\theta + \phi) \tag{3.20}$$

Fig. 3.9 a) shows the deposition profile along the circumference of a 3-inch wafer.

It is obvious that this is not uniform enough. In practice, the substrate is rotated during growth at 60 rpm for improved uniformity, see Fig. 3.9 b). Additionally, real cells yield good uniformity at the expense of reduced efficiency.
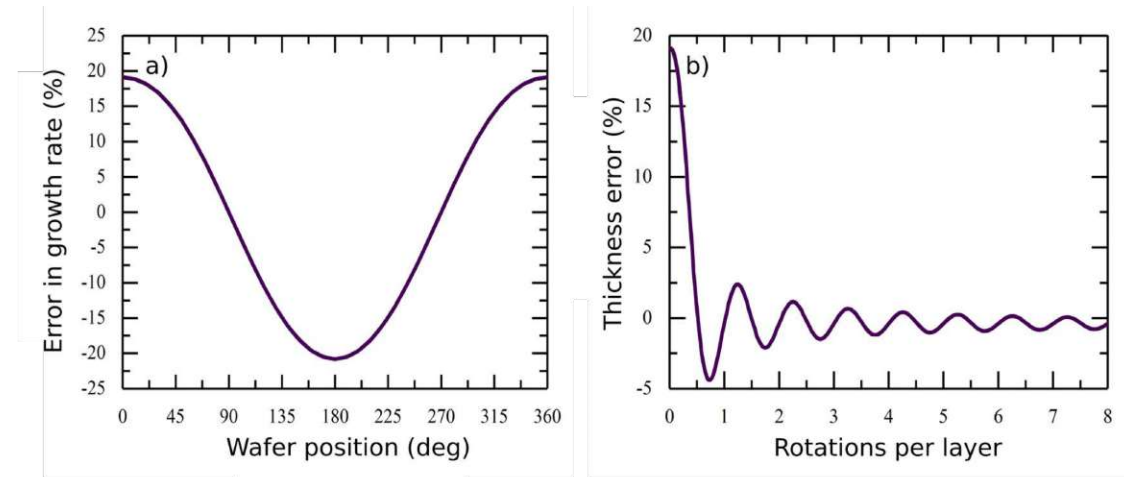
Figure 3.9: Calculated error in growth rate for a) without rotation over the wafer circumference, and b) with substrate rotation. (Reproduced with permission from A.M. Andrews, T. Roch, unpublished.)

For group-V elements cracking cells are employed. The reason is that group-V elements sublimate as tetramers. A cracking zone that is heated produces dimers or monomers, which can be more beneficial for specific growth conditions, because they are more reactive. A cracking cell has a reservoir that is loaded with material and is kept at a fixed temperature. The reservoir is closed with a valve. When the valve is opened material passes through a tube through the cracking zone into the chamber.

Challenges of measuring the substrate temperature:

Acquiring the correct substrate surface temperature during growth is crucial in MBE growth. There is a thermocouple located between the substrate and the heater. Because the substrate is rotating at 60 rpm during the growth and the heater is fixed, the thermocouple cannot touch the substrate. This results in the floating thermocouple measuring the heater temperature and not the substrate temperature. Another issue is that the temperature of the growth surface differs from the backside facing the heater. This is due to thermal absorption, conductivity, and additional radiation from the hot cells.

To measure the substrate growth temperature without contact or interference with the growth, either infrared pyrometers [99] or solid-state spectrometers measuring the temperature-dependent bandgap [102] are utilized. Optical pyrometers detect the radiance, see Fig. 3.10. The vertical lines give the detection wavelength of

employed pyrometers. For GaAs- and InP-based materials, a Si-detector at $0.97\,\mu m$ is commonly employed, which has its lower detection limit at a radiance of about $10\,\mu W/(m^2 sr)$. This limits the lowest measurable temperature to around $450\,°C$ [99]. By changing to a longer wavelength pyrometer, one can measure lower temperatures as long as the wavelength does not fall within the bandgap.
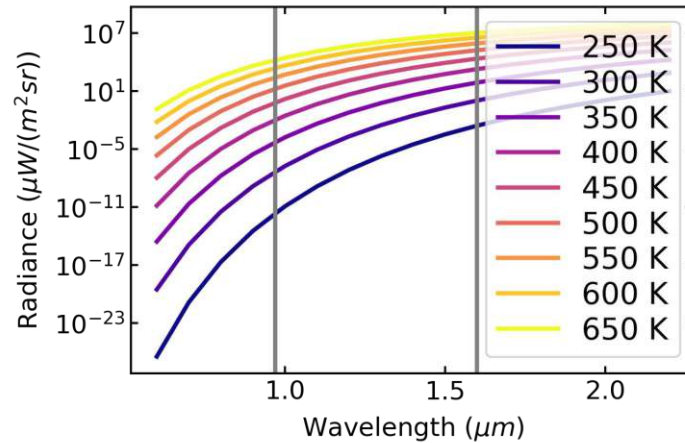
Figure 3.10: Radiance of a black body. The vertical lines at $0.97\,\mu m$ and $1.6\,\mu m$ are absorption wavelengths of commonly used detectors. (Reprinted with permission from the lecture notes of the course at TU Wien: 362.145 "Heterostructures for Nanoelectronics and Photonics")

The spectral emittance ϵ_λ is given as:

$$\epsilon_\lambda = \frac{\epsilon_{material}}{\epsilon_{blackbody}} \tag{3.21}$$

where the emittance of the material to be measured $\epsilon_{material}$ needs to be known, but also the transmissivity of the viewport. For bandgap measurements, the absorption edge of the substrate is measured using either diffuse reflected radiation or the substrate heater behind the sample as the broadband light source. For bandgap measurements, the limit for the lowest measurable temperature is the integration time, often the limit is set to the lowest temperature of $250\,°C$.

3.4.2 Growth mechanisms and kinetics

When a molecular flow of atoms impinges on the surface of a substrate, the atoms can either adsorb, desorb, migrate, aggregate with other adatoms, or incorporate, see Fig. 3.11. Sample surfaces are not perfectly flat, even GaAs $(0\,0\,1)$ surfaces always have a slight miscut to them, which introduces surface steps or kinks, on which it is energetically easier for adatoms to incorporate. The preferred growth mode for III-V
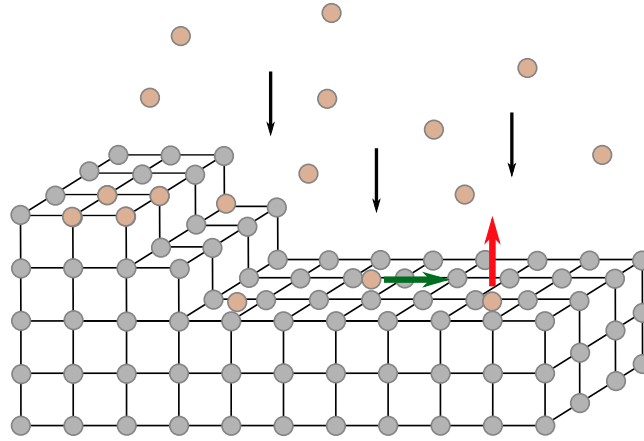
Figure 3.11: Sketch of processes occurring on the sample surface during MBE growth. The black arrows indicate the impinging molecular flow of atoms. The green arrow indicates surface migration and the red arrow desorption.

heterostructures in MBE is step-flow growth.

When growing material A on a substrate of material B, the nucleation of material A on material B is needed. This requires the careful adjustment of growth parameters, to achieve the wanted properties of the epitaxial layers, like low defect densities and a good layer morphology. Of course, during the growth process, physics, thermodynamics and chemistry play an important role.

Growth with As$_4$ vs. As$_2$

For the growth of As-based III-V heterostructures with MBE, either As$_4$ or As$_2$ molecules can be used, for which the interactions with the growing layer differ [89]. As$_2$ is first adsorbed into a weakly bound state, which would desorb again in less than 10^{-5} s unless group-III, e.g. Ga is available. The sticking probability of As$_2$ on GaAs is controlled by the Ga flux and is almost unity if enough Ga is available, otherwise, it is effectively zero. This maintains stochiometry.

The growth process is more complex for As$_4$ molecules. Again the As$_4$ is first adsorbed into a weakly bound state, with a desorption time shorter than 10^{-5} s. For As$_4$ the sticking probability is never greater than 0.5, even if there is enough Ga available. In a second-order reaction from two As$_4$ molecules, four As atoms are incorporated into the film while the other four As atoms desorb again as an As$_4$ molecule.

As mentioned above these two different growth mechanisms can influence the doping of the structure.

MBE growth modes:

Based on the growth conditions, like the temperature, surface saturation, and strain, different modes of growth can be energetically favorable. Macroscopically, the occurrence of a growth mode can be described by the surface free energies of the substrate γ_S, the epitaxial layer γ_L, and the interface between the substrate and the layer γ_I. Complete wetting of the substrate by the layer material occurs when the relation $(\gamma_L + \gamma_I) \leq \gamma_S$ is fulfilled, and the layer atoms are bound more strongly to the substrate than to each other. Otherwise, the energy of the system would have to increase, and therefore only partial wetting occurs.

Traditionally, three growth modes have been described for MBE growth [89, 90], see Fig. 3.12:
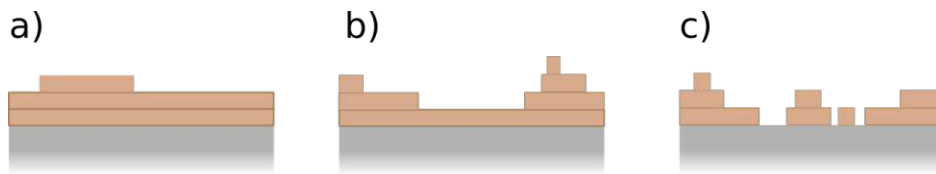
Figure 3.12: The three classical growth modes are sketched. a) Frank-van der Merwe growth where the film grows layer by layer, b) the Stranski-Krastanov growth where islands grow and no complete wetting of the surface occurs, and c) Volmer-Weber growth where after the completion of one layer islands grow.

Frank-van der Merwe growth is a 2-D layer-by-layer growth mode Fig. 3.12 a). For the purposes of MBE heterostructure growth, the Frank-van der Merwe growth mode is preferred for smooth surfaces and sharp interfaces between the sometimes even sub-nanometer thick layers. This mode fulfills the condition $(\gamma_L + \gamma_I) < \gamma_S$. In Fig. 3.12 b) the Stranski-Krastanov growth mode is illustrated. It is a growth mode that is first 2-D, but after a certain critical layer thickness is surpassed becomes 3-D, and $(\gamma_L + \gamma_I) \geq \gamma_S$ is barely satisfied. In Fig. 3.12 c) the Volmer-Weber growth is depicted. It is a 3-D growth mode where islands prefer to form, which then grow and coalesce, but the resulting surface has a high root mean square (RMS) surface roughness. For this growth mode $(\gamma_L + \gamma_I) > \gamma_S$ holds.

Growth of thin layers

The growth of thin layers with MBE becomes especially important for QCDs designed for high absorption energies, because the wells need to be significantly thinner (around 1 nm or less) to create the necessary energy levels. The ability to grow reproducible uniform thin layers depends on the following parameters: the growth rate, the substrate rotation, the shutter transients, the shutter timing, and the shutter opening

and closing time.

Previously, the evaporation uniformity due to the cell's geometry and the rotation of the substrate was discussed. Fig. 3.9 b) shows the error in film thickness at the wafer edge vs. the rotations per layer. Layers need to be deposited either during an integer number of rotations or with four or more rotations to be homogeneous. If the first condition is fulfilled, then exactly one rotation is sufficient. For this, the growth rate of the thin layer needs to be adapted.
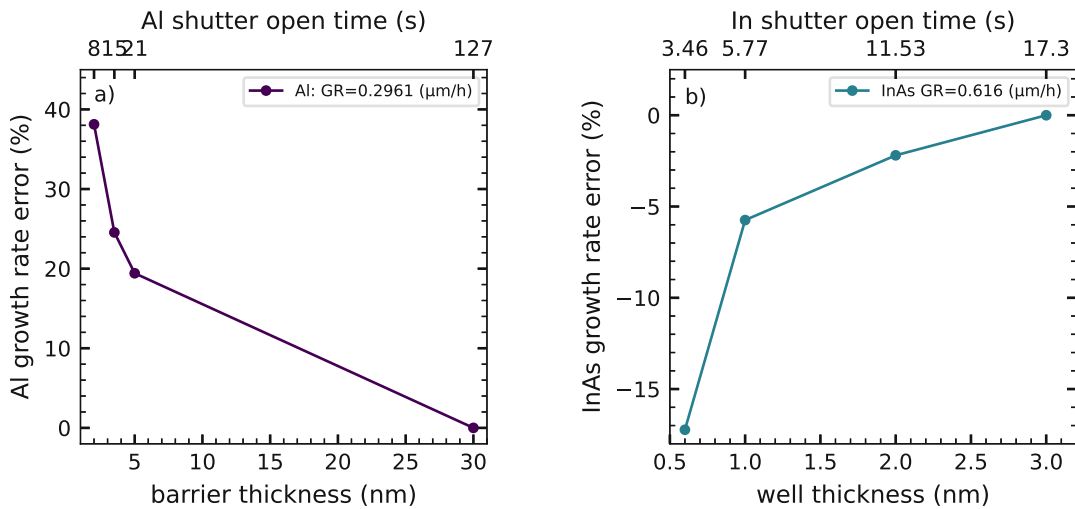
Figure 3.13: The growth error due to shutter effects is plotted for a) AlGaAs growth and b) InAs growth. It was measured by growing multiple superlattice structures and analysis by HR-XRD. It is visible that the Al- and In-cell show exactly the opposite behavior, due to the operating conditions of each cell.

Effects that can be neglected with sufficiently thick layers, like shutter opening and closing times or shutter transients, need to be taken into account. Shutter operation times are usually around 100 ms. For the cell to stabilize again after it was brought out of equilibrium when the shutter opens or closes, takes time. This depends on cell design, temperature, and the PID-control loop, which controls the supplied power to keep the cell temperature stable. As mentioned above, group-III cells have two heaters, each having their own thermocouple and control loop, one for the base and one for the tip. Often, the base and tip are kept at different temperatures to optimize cell performance. If the PID settings are not optimal, the supplied power and therefore temperature can start to oscillate due to interference. A deviation in cell temperature of more than $0.2\,°C$ is too much to maintain the growth rates. Another parameter is, how fast the control loop reacts to changes. Once the shutter opens, the cell is not in equilibrium anymore and the supplied power needs to be adapted until the cell reaches equilibrium. The time this process needs is critical for

growth rate deviations due to shutter transients. In Fig. 3.13, the error in growth rate is plotted over the layer thickness for a) AlGaAs and b) InAs layers. During the growth of thin layers, the error due to shutter transients has to be taken into account.

3.4.3 Surface reconstruction

Surfaces are abrupt terminations of the bulk crystal. The terminating atoms have broken bonds, so-called dangling bonds. All systems drive to minimize their energy, therefore the surface atoms rearrange. This happens either by surface relaxations, aka a change of position of the surface atoms, where neither the symmetry nor the periodicity is altered or by surface reconstructions, which alter both the symmetry and periodicity.

The saturation of broken bonds is usually accompanied by local deformations which introduces strain. Stable recombinations result when the energy reduction is greater than the induced strain energy. Surface reconstructions (a dimerization of surface atoms) can belong to one of five types: square, rectangular, centered rectangular, hexagonal, and oblique [35, 90]. It is important to note that surface reconstructions are not limited to just the topmost monolayer, but incorporate in two or more layers.

In an ideal case, III-V semiconductor $(1\,0\,0)$ surfaces can be either terminated by group-III or group-V atoms, where different reconstructions form for both cases. The termination can be controlled during MBE by changing the group-III to group-V ratio, growth temperature, and adsorbates.

Wood's notation:

Surface reconstruction naming follows Wood's notation [27]. Here, a_S is the surface mesh and a_B the bulk mesh, then they have the unit translations a_{1S}, and a_{2S} and a_{1B}, and a_{2B}, respectively. The surface reconstruction is then noted as $(a_{1S}/a_{1B} \times a_{2S}/a_{2B})$R. Where R indicates any rotations of the surface mesh, and if the rotation is 0°, it is omitted. A c in front of the expression is used to indicate centered meshes.

GaAs $(1\,0\,0)$ and InAs $(1\,0\,0)$ reconstructions:

MBE grown GaAs $(1\,0\,0)$ typically exhibits a (2×4) reconstruction, which is the result of an As-stabilized surface at a temperature of $600\,°C$. A Ga-stabilized surface would yield a (4×2) reconstruction. The same reconstructions are also observed for InAs $(1\,0\,0)$ surfaces at lower temperatures. Fig. 3.14 depicts a (2×4) reconstruction

on a GaAs (1 0 0) surface. The black spheres corresponding to As atoms form dimers due to the dangling bonds of the surface atoms.
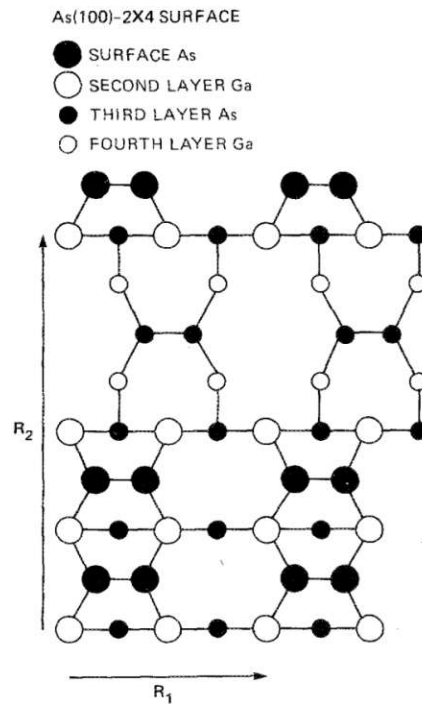
Figure 3.14: Surface reconstruction formation of a GaAs (100) surface, where a (2×4) reconstruction forms, as indicated by the rectangle marking the unit cell. (Reprinted with permission from [103]. Copyright 1987, American Vacuum Society.)

3.4.4 Growth of InAs/AlAs$_{0.16}$Sb$_{0.84}$ on InAs substrates

InAs/AlAs$_{0.16}$Sb$_{0.84}$ is grown lattice-matched to InAs. The thermal oxide removal (ox-off) was performed at 510 °C under an As flux of 1.1×10^{-5} Torr. To find the optimal ox-off temperature, the surface was monitored with RHEED, and the surface roughness and defect concentration were analyzed with an optical microscope for different oxide removal temperatures.

To obtain lattice-matching, a certain As-to-Sb ratio has to be kept in the AlAsSb barriers. A known phenomenon is the As-for-Sb exchange, which occurs because of the higher binding energy of As, compared to Sb. The dependencies on the growth rates, the growth temperature, and the flux ratios were studied in a previous work [31, 93] and in literature [104, 105]. This exchange means that As can irreversibly claim a lattice site previously occupied by an Sb atom up to three monolayers in depth. Due to these factors, achieving the correct ratio can turn out to be challenging. Different steps are necessary:

Finding the lowest As-stabilized growth flux:

Usually, III-V compounds are grown in a group-V over-pressure for smooth films, and then the growth is limited by the availability of the group-III element due to its high sticking coefficient, see section 3.4.2. For the growth of $AlAs_{0.16}Sb_{0.84}$ the correct As:Sb ratio is necessary. The exact amount of supplied group-V flux depends on the group-III growth rate and the growth temperature, while also the growth rate shows a dependency on the growth temperature due to the competing group-V atoms. A higher growth rate needs a higher supply of group-V flux, but a higher growth temperature will facilitate the As-for-Sb exchange. Different As fluxes are necessary to grow InAs and $AlAs_{0.16}Sb_{0.84}$. While InAs can be grown in an As over-pressure, no excess As in the chamber is desired for the subsequent barrier growth. If too little As is supplied, In droplets will form on the surface, therefore, the lowest As-flux for high-quality InAs growth was determined. To find the lowest As-pressure, InAs layers were grown on InAs substrates while monitoring the surface reconstruction with RHEED. During InAs growth in an As-rich environment, a (2×4) reconstruction will form. As soon as the growth changes to an In-rich environment the reconstruction will change to (4×2), see Fig. 3.23. The lowest As pressure for As-stabilized environments was then recorded for different temperatures, see Fig. 3.15, revealing a linear behavior over the temperature range. Finally, the optimized flux values for $InAs/AlAs_{0.16}Sb_{0.84}$ growth was an As flux of 3.0×10^{-6} Torr during the InAs growth with a growth rate of $0.62\,\mu m/h$ and an As flux of 9.0×10^{-7} Torr during the $AlAs_{0.16}Sb_{0.84}$ growth with a growth rate of $0.48\,\mu m/h$. This quick change of flux for these alternating layers was achieved by opening and closing the As shutter, while keeping the valve open, while the As valve position was optimized to lattice match the $AlAs_{0.16}Sb_{0.84}$ layers.

Lattice-matching:

As a first step, bulk AlAsSb was grown on InAs to find the correct lattice-matching parameters. These calibrations were analyzed with high-resolution X-ray diffraction (HR-XRD). In the second step, superlattices with InAs were grown. As mentioned above, during the growth of the InAs and the AlAsSb layers, the As shutter was closed and opened. While for group-III materials or Sb, a closed shutter hinders the material flux to the substrate completely, this is not true for As. The closed As shutter decreased the As flux to approx. 1/3 of the open-shutter flux. In the case of growing AlAsSb, As shutter operations were preferred, due to their short duration, over As valve operations, typically 100 ms. Additionally, it was observed that the As flux does not need as long to stabilize again as is the case after case after As valve
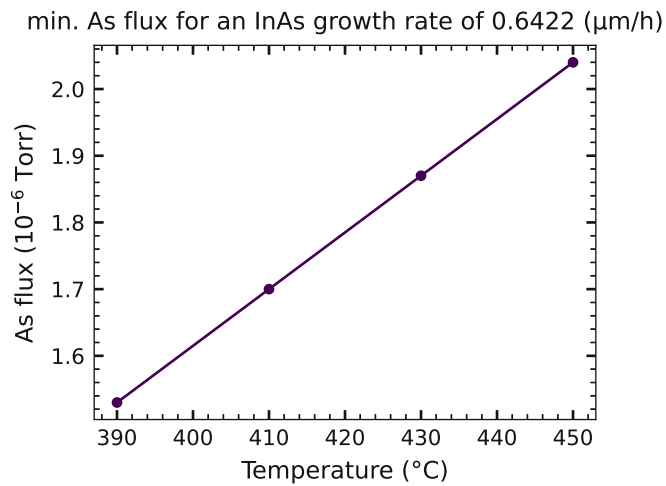
Figure 3.15: The minimum As flux for a stabilized InAs growth with an InAs growth rate of $0.6422\,\mu\text{m/h}$ is plotted over the growth temperature.

operations.

The final lattice-matching conditions for the $AlAs_{0.16}Sb_{0.84}$ barriers were chosen as follows for the grown QCDs: At an growth rate of $0.48\,\mu\text{m/h}$, the As flux was $9.0{\times}10^{-7}$ Torr, and the Sb flux was $2.8{\times}10^{-6}$ Torr.

Optimizing the growth temperature:

MBE growth takes place in non-equilibrium conditions, where the growth temperature is chosen to be $\leq 2/3$ of the melting temperature of the substrate. If the temperature is chosen too low, the migration length of adsorbed atoms is not long enough to find an optimal incorporation spot, preferably at a kink or step edge, the growing film will get rough, and in the worst case, islands will start to grow. With the optimal growth temperature, the interface roughness and interdiffusion of the layers can be minimized. The optimal growth conditions for InAs and Al(As)Sb are different, due to their different binding energies and mobilities on the substrate surface. Literature suggests a growth temperature higher than $500\,^\circ\text{C}$ for AlSb layers [106] and a growth temperature of around $430\,^\circ\text{C}$ for InAs layers [107]. To investigate this, InAs/AlSb $(2.5/2.4\,\text{nm}$ and $2.5/1.5\,\text{nm})$ double-superlattice (SL)s at the growth temperatures of $450\,^\circ\text{C}$ and $420\,^\circ\text{C}$ were grown. It was observed that at $420\,^\circ\text{C}$ the FWHM of SL peaks in HR-XRD-scans decreased by about $15\,\%$ from 155.77 arcsec to 135.57 arcsec, see Fig. 3.16 a) and b).

For the grown devices, the lower growth temperature had two additional benefits: The temperature-activated As-for-Sb exchange could be better controlled, and the diffusion and intermixing of the grown layers decreases, which promotes sharp
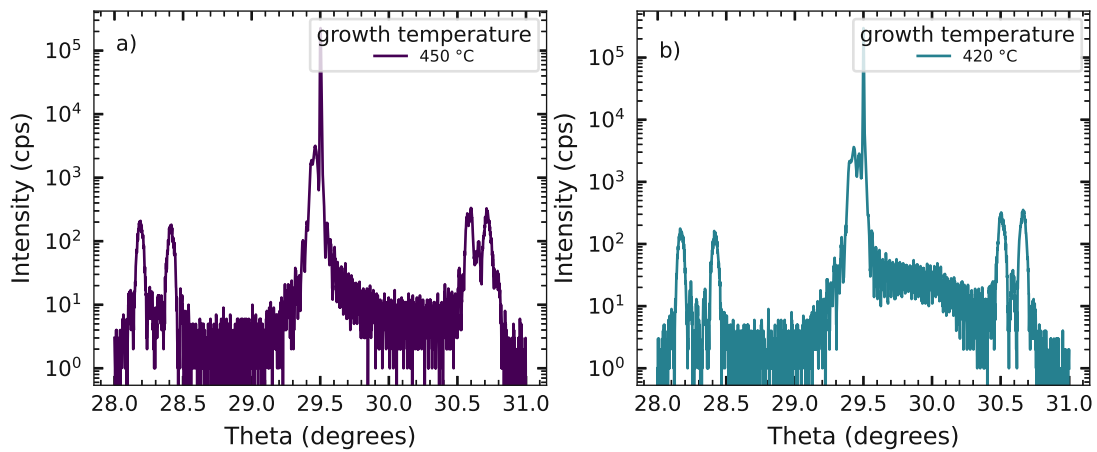
Figure 3.16: InAs/AlSb (2.5/2.4 nm, and 2.5/1.5 nm) double superlattices grown on GaSb. The growth temperature was a) 450 °C, and b) 420 °C. The FWHM of the SL peaks are 155.77 arcsec and 135.57 arcsec, respectively.

interfaces.

Optimizing shutter sequences:

To achieve low interface roughness and prevent interdiffusion of the layers (in addition to the growth temperature) shutter sequences and waiting times influence growing layers, including the thin layers employed (around 1-3 nm) [108–110]. The sequences were developed by analyzing the FWHM of satellite peaks in HR-XRD scans. While waiting times between the layers prolong the growth and therefore yield higher material and energy consumption, it was found that without the waiting times after the InAs layer excess As incorporated in the AlAsSb layers. The best results were from a 2 s waiting time after each layer.

Published results also come to the conclusion that InSb interfaces, rather than AlAs between the InAs/Al(As)Sb layers, yield higher material quality and are beneficial for carrier mobility [108, 111]. Therefore, these interfaces were facilitated by the implemented shutter sequences.

3.4.5 Growth of InAs/AlSb on GaSb substrates

The growth on GaSb substrates was first established in this group during this Ph.D. work. Therefore, additional steps were taken to characterize the heterostructures.

The thermal oxide removal from GaSb substrates was conducted in an Sb-stabilized atmosphere. The first calibrations were the oxide removal from the GaSb substrate and a GaSb buffer layer grown at 485 °C. The samples showed cross hatching and an

RMS surface roughness of 0.349 nm, see Fig.3.17 a), which shows a $10\times10\,\mu$m atomic force microscopy (AFM)-scan of the sample surface with the emerging crosshatch pattern.
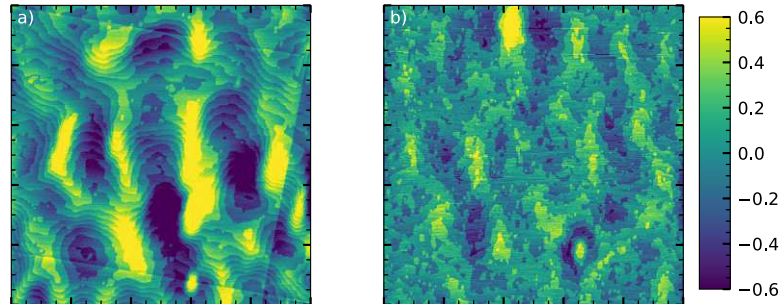
Figure 3.17: AFM-scans of an area of $10\times10\,\mu$m of GaSb grown on on a GaSb substrate after the thermal oxide removal. In a) cross-hatching is visible, which occurred due to As contamination in the chamber. The RMS surface roughness is 0.349 nm. b) The RMS surface roughness is 0.218 nm.

In the HR-XRD, a peak to the right of the substrate peak is observed. This is the result of As incorporation into the film by the residual As-background of approx. 1×10^{-8} Torr from previous As-stabilized growths. The As-background was two orders of magnitude lower than the Sb-flux. This result points out the potency of the As-for-Sb exchange.

A smooth surface after the thermal oxide removal is important because the crystalline quality of the substrate has a significant influence on the layer quality grown on top. Optimal parameters for the thermal oxide removal were found to be a temperature of $570\,°$C at a stabilizing Sb flux of 1.0×10^{-6} Torr and a subsequent smoothing GaSb buffer layer of 100 nm grown at a temperature of $485\,°$C. Fig.3.17 b) shows an AFM-scan of a $10\times10\,\mu$m area with an RMS surface roughness of 0.218 nm, where a 300 nm GaSb buffer layer had been grown.

In the following, the unique growth challenges of this material system are discussed:

Optimizing shutter sequences:

Contrary to the growth of InAs/AlAs$_{0.16}$Sb$_{0.84}$, no As at all is wanted in the AlSb layers. The result is more severe measures to counteract As incorporation in AlSb. Waiting times and retarded As valve opening and closing times were developed through analysis of InAs/AlSb HR-XRD-scans. The optimized growth opens the As valve 1 s before the InAs layer is grown and closes it up to two monolayers (depending on InAs layer thickness) before it is finished to deplete the As in the chamber before all the shutters are closed. A waiting time of 3.5 s lets the system stabilize before

the Sb shutter is opened 1 s before the AlSb growth starts. The result is nominally strain balanced InAs/AlSb (2.4/2.5 nm and 2.4/1.5 nm) SL, see Fig. 3.18, where the zero-th-order SL peak of the first strain balanced SL overlaps with the substrate peak and thus suggests ideal strain-balancing.
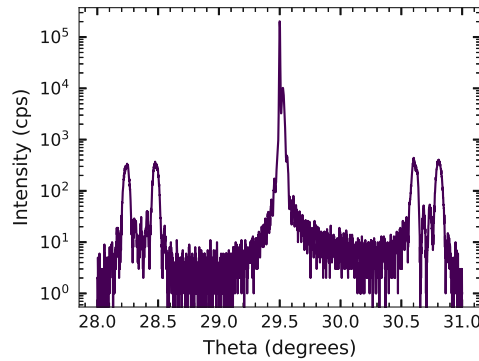
Figure 3.18: HR-XRD of an InAs/AlSb double-SL (2.4/2.5 nm and 2.4/1.5 nm) grown on GaSb. Note that the second superlattice, grown to determine the growth rates, is not strain balanced and its zero-th-order SL peak is to the right of the substrate peak in the center.

Doping of GaSb:

For the growth of InAs/AlSb structures on GaSb, Te was utilized as a dopant instead of Si, although the InAs wells are also n-type doped with Si. This is due to the following reasons:

After the thermal oxide removal, a GaSb buffer layer has to be grown to smoothen the surface again before the SL growth is started. Undoped GaSb grown by MBE is p-type due to a native acceptor background related, among others, to Sb- and Ga-deficiencies [112] with a concentration of 1–3×10^{15} $1/cm^3$, for a 5–7 µm thick GaSb layer measured with Hall [113] and therefore has to be doped. Si acts more as a p-type dopant for Sb compounds due to its amphoteric behavior. For this reason, Te in the form of a GaTe compound was used as an n-type dopant. The second reason is that the unwanted diffusion of Si atoms from the InAs wells into the AlSb barriers could cause p-type doping, see section 3.3.

Literature suggests a doping minimum for n-type doping of GaSb with Te at 77 K of 1.3×10^{16} $1/cm^3$ [114] of 5–7 µm thick GaSb grown with MBE on GaAs and measured with Hall [113], where electrical photoluminescence spectra in this study suggest that below a doping of 1×10^{17} $1/cm^3$ a band related to acceptor states is still dominant although donor bands emerged [114].

3.5 Analysis of III-V heterostructures

There are several non-destructive in-situ and ex-situ analysis techniques that were used to characterize the grown structures, which are explained in the following:

3.5.1 Reflection high-energy electron diffraction (RHEED)

RHEED is an in-situ surface analysis technique that is available in most MBE-systems due to the UHV growth conditions [90, 115]. Electrons are accelerated from an electron gun to several keV (8–30 keV) towards the sample surface under a low angle of 1.1–1.5°. The diffracted beam then hits an aluminum-coated fluorescent phosphors screen and forms a diffraction pattern that can be recorded with a camera.

Due to the glancing incident angle and the low interaction between incident electrons and atoms, RHEED is a surface-sensitive technique of the surface reconstruction morphology, and crystal lattice.

Diffraction conditions:

When electrons are scattered by two atoms in a 1-D chain constructive interference takes place when the path difference between the two scattered waves is a multiple of the wavelength, see Fig. 3.19.
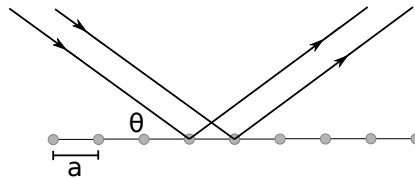
Figure 3.19: Sketch of the electron diffraction on a 1-D chain with lattice-constant a.

Following [90, 115] and using $k = \frac{2\pi}{\lambda}$ for the wave vector the condition is:

$$kcos\theta_i - kcos\theta_f = \frac{2\pi n}{a} \tag{3.22}$$

where θ_i and θ_f are the incident and final scattered glancing angles.

Fig. 3.20 illustrates the allowed wave vectors for diffraction conditions. In 2-D this condition becomes:

$$\mathbf{k}_{f,t} - \mathbf{k}_{i,t} = m_1\mathbf{a}_1^* + m_2\mathbf{a}_2^* \tag{3.23}$$

where $\mathbf{k}_{i,t}$ and $\mathbf{k}_{f,t}$ are the initial and final 2-D wave vectors, m_1 and m_2 are integers and $\mathbf{a}_1^*$ and $\mathbf{a}_2^*$ reciprocal space lattice vectors. For a 2-D grid, the periodicity in the
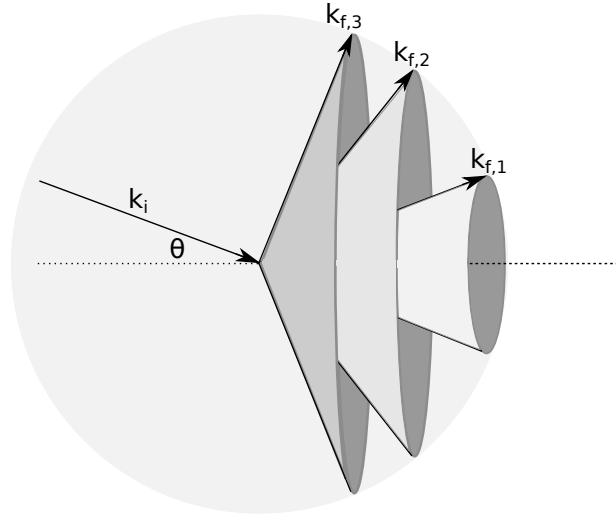
Figure 3.20: Sketch of the allowed diffracted wave vectors kf1 and its higher diffraction orders $k_{f,2}$, and $k_{f,3}$.

third direction is missing, the reciprocal lattice becomes a family of rods.

The Ewald sphere:

Points along the Ewald sphere conserve energy and momentum [90, 115]. For energy conservation $|\mathbf{k}_{i,t}| = |\mathbf{k}_{f,t}|$ must hold. Momentum conversation means that $\mathbf{k}_{f,t} - \mathbf{k}_{i,t} = \mathbf{G}_m$ must hold, where $\mathbf{G}_m$ is a 3-D reciprocal lattice vector. The intersection of the Ewald sphere with the reciprocal lattice rods, which fulfill constructive interference, determines the allowed diffraction points, which lie on a circle called Laue zone, see Fig. 3.21. In this case, the Bragg condition is fulfilled. The separation of the reciprocal lattice rods is the reciprocal lattice vector $\mathbf{B}_m$. For a square lattice, the spacing between the rods is given by $2\pi/a$.

Kikuchi lines:

Kikuchi lines are formed by inelastic electron scattering processes during electron diffraction, see Fig. 3.22. When electrons inelastically scatter, some scatter along lattice planes due to having the correct Bragg angle. These electrons then form the Kikuchi lines and can be attributed to crystal directions. The intensity of those lines depends strongly on the surface morphology. The observation of Kikuchi lines on the RHEED screen is a sign of flat surfaces, as scattering from steps or surface roughness broadens Kikuchi lines [115].
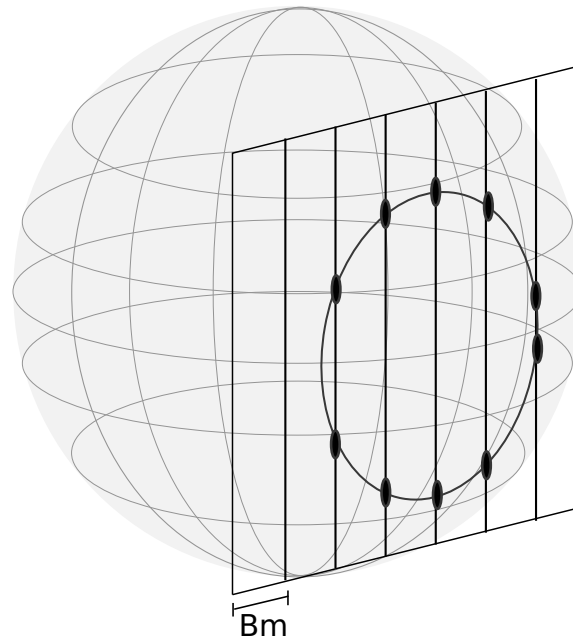
Figure 3.21: Sketch of the Ewald sphere. Where it intersects the 2-D reciprocal space of lattice rods determines the allowed diffraction points. $\mathbf{B}_m$ the reciprocal lattice vector corresponds to the separation between the single rods.
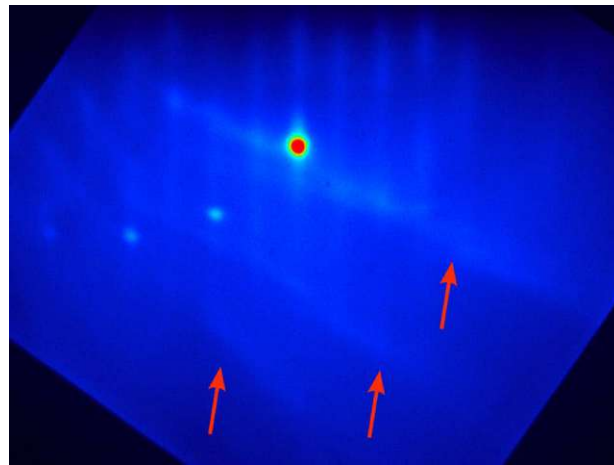
Figure 3.22: Kikuchi lines forming on an InAs RHEED pattern (some are marked with red arrows). A Laue zone is visible as well.

Applications:

RHEED is used as an in-situ tool to determine the surface quality of a growing sample in real-time [116]. Electrons diffracted from an infinitely and atomically flat surface will have reciprocal lattice rods that will be infinitely narrow. The rods will appear as points on the RHEED screen. In reality, even on an atomically flat surface, there are lattice vibrations that lead to a finite width of the reciprocal rods. Moreover, the Ewald sphere surface has a finite thickness, because the electron beam

is not entirely monochromatic. Depending on the growth mode, the surface will not be perfectly flat but steps or islands are constantly present, which broadens the reciprocal rods. All of these factors make the reciprocal rods appear more like ellipses on the screen. If the surface becomes rough, in other words, 3-D, the third dimension is well defined and the reciprocal rods turn into points on the RHEED screen.

Amorphous surfaces, such as an oxide layer on the sample, will not show a RHEED pattern at all. RHEED is therefore used to monitor the thermal oxide removal procedure. With RHEED surface reconstructions (see subsection 3.4.3), which help to determine growth conditions can be monitored, see Fig. 3.23 of an As-rich a) and In-rich b) surface reconstruction of InAs.
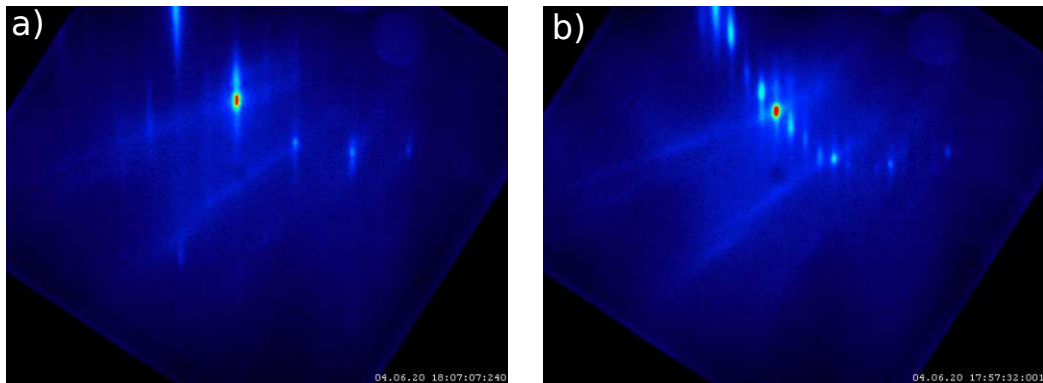
Figure 3.23: RHEED pattern of an InAs surface, under a) As-rich conditions forming a (2×4) reconstruction, and b) In-rich conditions, forming a (4×2) reconstruction. Kikuchi lines and the zero-th-order Laue zone are visible as well.

With RHEED, the growth rate can be determined, due to the dependency of the RHEED spot intensity on the surface, see Fig. 3.24 for an illustration. If the surface is flat, the RHEED intensity is at its maximum. When a monolayer grows, depending on the growth mode, first, 2-D islands will form, and the spot intensity will fall due to deconstructive interference. As soon as the islands connect again to a flat monolayer the intensity will rise again.

3.5.2 High-resolution X-ray diffraction (HR-XRD)

HR-XRD is a powerful tool for nondestructive ex-situ characterization of epitaxial layers. It yields information about composition, uniformity, thickness, strain, relaxation, and crystallinity. For heterostructures, it further obtains information about interfaces. An excellent book on the analysis of epitaxial layers is [32]. In the further course, an overview of the basic principles for III-V semiconductor heterostructure characterization is given.
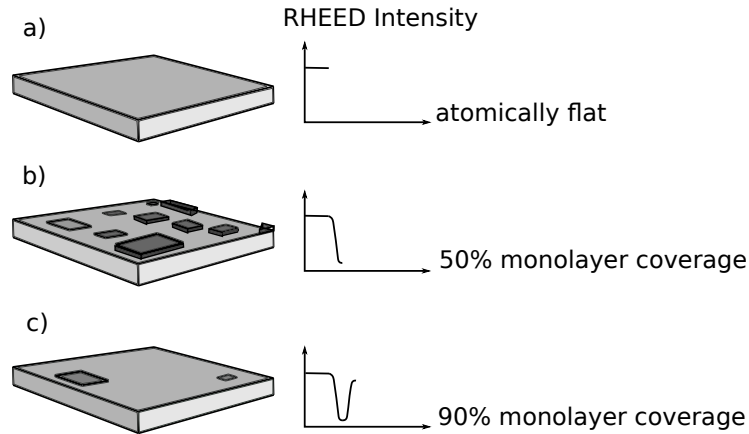
Figure 3.24: Illustration of the intensity variation of RHEED spots, due to the surface morphology. In layer-by-layer growth, the growth rate can be determined by intensity oscillations.

ω-2θ-scan:

ω is the angle between the sample surface and the incoming X-ray beam [32]. If the sample surface is not parallel to the lattice planes an angle ϕ exists. θ is the angle between the incident beam and the lattice planes. If $\phi = 0$ then $\theta = \omega$. A reflection is called symmetric for planes where $\theta = \omega$, like $(0\,0\,1)$, $(0\,0\,2)$, etc.. In that case, θ is rotated twice as fast as ω in an ω-2θ-scan. For asymmetric reflections $\omega = \theta \pm \phi$, high incidence ($+\phi$), and low incidence ($-\phi$) reflections exist, for example, the $(1\,1\,5)$ and $(\bar{1}\,\bar{1}\,5)$ planes. Whenever diffraction on a crystal is involved, Bragg's law comes into play:

$$2d_{hkl}sin\theta_B = n\lambda \tag{3.24}$$

where d_{hkl} is the spacing of the lattice planes and hkl the Miller indices of the plane. θ_B is the Bragg angle, λ the wavelength and n an integer number.
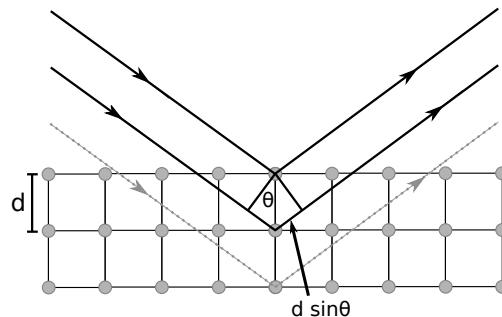
Figure 3.25: Sketch of Bragg's law for constructive interference.

Fig. 3.25 shows a sketch of the diffraction on lattice planes. Constructive interference between X-ray scattering on the upper lattice plane and X-ray scattering on

the lower occurs when their path difference 2δ is a multiple of λ.

Under the assumption of elastic scattering the incident (k_i) and diffracted (k_s) wavevector fulfill following relation:

$$\mathbf{G}_{hkl} = \mathbf{k}_s - \mathbf{k}_i \qquad (3.25)$$

where $\mathbf{G}_{hkl}$ is the reciprocal lattice vector. $\mathbf{G}_{hkl}$ points to the surface of the Ewald sphere in reciprocal space.

Figure 3.26: Sketch of the reciprocal space map, showing accessible and inaccessible areas for Bragg diffraction. (Reprinted with permission from [32]. Copyright 1996, Springer.)

Fig. 3.26 shows the reciprocal space map, showing accessible and inaccessible areas for Bragg diffraction. For (0 0 1) oriented substrates with heterostructures the most common scans are performed on the (0 0 4) and (0 0 2) planes. Based on the atomic structure factors, the intensity of the satellite peaks compared to the substrate peak is higher for the (0 0 2) scan, as seen in Fig. 3.27.

For an ω-2θ-scan, ω between k_i and the sample surface changes [32]. This yields a straight, radial movement of k_s in reciprocal space from the origin (0 0 0) along $\mathbf{G}_{hkl}$, see Fig. 3.28 a). An ω-scan with fixed 2θ would yield a transverse movement in reciprocal space, Fig. 3.28 b). Such scans yield so-called rocking curves.

Figure 3.27: . HR-XRD-scans of a GaAs/AlGaAs multi-quantum well structure. While in the $(0\,0\,4)$-scan the substrate and 0th-order SL peaks are better resolved, in the $(0\,0\,2)$ scan the higher order SL peaks have higher intensity.
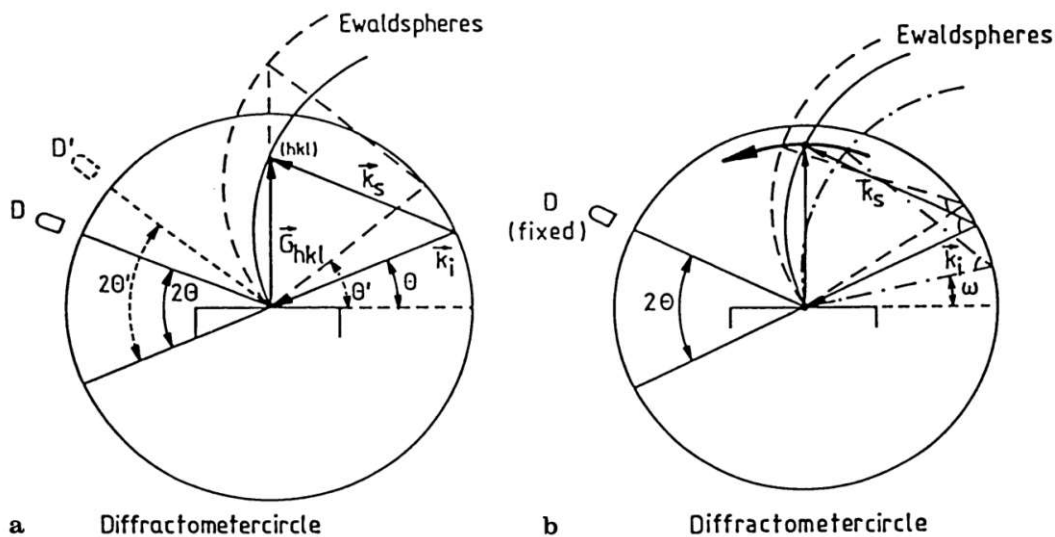
Figure 3.28: Sketch of the Ewald spheres for a) an ω-2θ-scan resulting in a radial movement of k_s in reciprocal space and b) an ω-scan with a fixed 2θ resulting in transverse movement in reciprocal space. D denotes the detector. (Reprinted with permission from [32]. Copyright 1996, Springer.)

Triple-axis spectrometer:

For single-crystal heterostructures either a double-axis or triple-axis spectrometer were used, where the latter is an extension of the double-axis system with an analyzer crystal between the sample and the detector [32]. For a sketch of the setup view Fig. 3.29.

For HR-XRD one sacrifices intensity and measurement speed to gain accuracy in the angular resolution and thus narrow diffraction satellites can be observed. This is
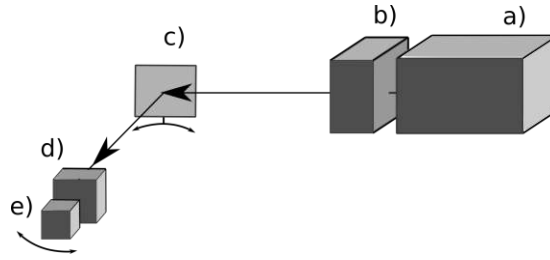
Figure 3.29: . Sketch of a triple-axis configuration for HR-XRD. a) is the X-ray tube, b) Bartel's monochromator, c) the sample, d) the analyzer, and e) the detector. For this setup, the X-ray tube is fixed and the sample, analyzer, and detector rotate.

done with monochromators in front of the X-ray source. In our case, a CuK-alpha X-ray source together with a Bartels 4-bounce-monochromator and collimator with channel cut $(2\,2\,0)$ Ge was utilized. The analyzer is also a channel-cut crystal that additionally narrows the diffracted beam before the detector, to sample a smaller slice of reciprocal space.

Measurement of strain:

If (partial) strain relaxation occurs, due to the introduction of misfit dislocations, all the grown layer is not pseudomorphic anymore [32]. This means the in-plane lattice vector does not correspond to the one of the substrate anymore. To determine this, it is necessary to perform asymmetric scans of planes in the $[1\,1\,0]$ and $[\bar{1}\,\bar{1}\,0]$ directions. While symmetric scans of the planes in the $[0\,0\,1]$ direction measure the lattice constant in the z-direction.
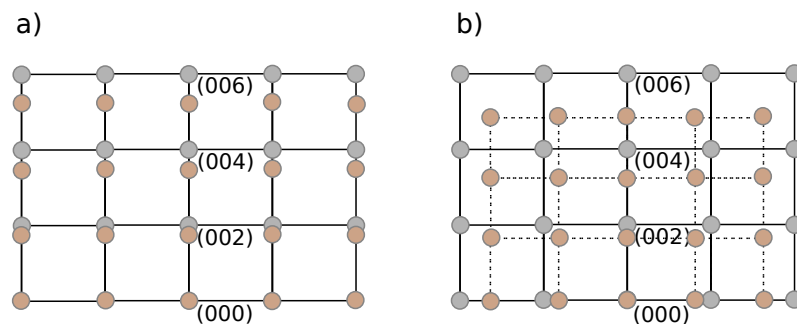
Figure 3.30: Sketch of the reciprocal space of a substrate crystal (grey points) and the grown layers (orange points). a) shows the case of a fully strained grown layer, while in b) it is completely relaxed.

Fig. 3.30 shows the crystallographic directions in the reciprocal lattice for the substrate (gray) and a) a fully strained layer, and b) a fully relaxed layer. Since in the fully strained case the in-plane lattice constant of layer and substrate are identical, their in-plane positions in the reciprocal lattice overlap. Once the layer

fully relaxes it becomes cubic again (rectangular in reciprocal space), hence the asymmetric lattice points do not overlap with the substrate anymore.

Fig. 3.31 shows the $(1\,1\,5)$ and $(\overline{1}\,\overline{1}\,5)$ scan of a not lattice-matched AlAsSb layer grown on InAs.
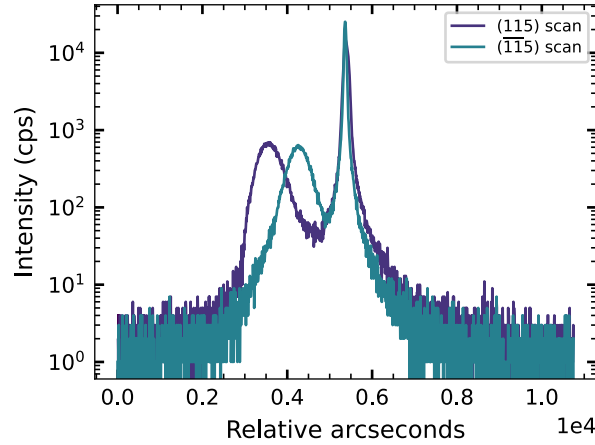
Figure 3.31: HR-XRD-scans of a not lattice-matched bulk AlAsSb layer grown on InAs.

Superlattices:

Fig. 3.32 shows a HR-XRD of an InAs/AlSb QCD. The substrate is usually the highest intensity peak in these structures, followed by the zero-th-order superlattice peak, also higher-order SL-peaks of the active region (AR) are observed, where the first three SL peaks in both the positive and negative directions are labeled. For this structure, a contact-SL with a different periodicity was additionally grown. The peaks are broader, because the contact-SL are thinner, additionally, they are further apart because the SL period is smaller. The higher order contact-SL peaks are also labeled. On the right side, a broad modulation of intensity is visible. The envelope function corresponds to a 20 nm thick InAs layer that was grown as a top contact. On this modulation so-called thickness fringes are visible.

The period of a superlattice, D, namely the thickness of the repeating structure, which is composed of multiple layers is given as [32]:

$$D = \frac{(L_i - L_j)\lambda}{2(sin\theta_i - sin\theta_j)} \tag{3.26}$$

where L_i and L_j are satellite peaks, and θ_i and θ_j are the corresponding Bragg angles. From this equation, growth rate deviations can be determined. To find out the deviations of each layer within one period, more conditions are necessary. In the
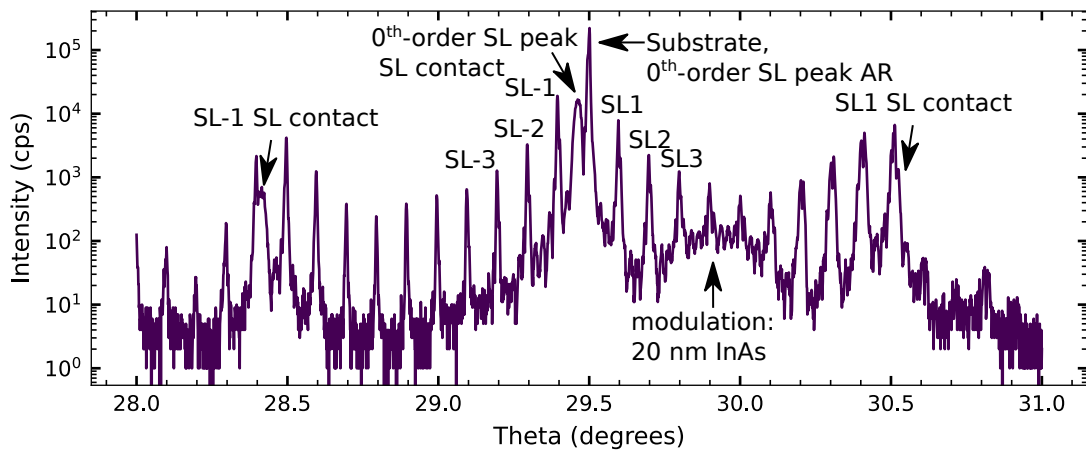
Figure 3.32: . HR-XRD-scan of an InAs/AlSb QCD. The substrate, the 0th-order SL peaks, a few higher-order SL peaks, and an intensity variation due to a top contact are labeled.

GaAs/Al$_x$Ga$_{1-x}$As material system, one additional condition is the total Al-fraction in the structure, given by the distance of the zero-th-order diffraction peak to the substrate. For the InAs/AlSb material system, double-superlattices have to be grown, where the thickness of one material stays constant in both superlattices.

The satellite peak FWHM and the intensity, and position provide information on thickness and composition variations, as well as interface roughness and interdiffusion.

Reciprocal space map (RSM) scans:

As discussed above, ω-2θ-scans yield a radial movement in reciprocal space, while a ω-scan with fixed 2θ yields a transverse movement. By scanning slices of ω-2θ-scans for different ω offsets a space map of reciprocal space can be obtained, see Fig.3.33.

From such an reciprocal space map (RSM) a number of conclusions can be drawn [32]: RSMs in asymmetric crystal directions yield conclusions about strain and relaxation in a layer, see section 3.5.2. Depending on the shape of the now 3-D peak, conclusions about mosaic spread (crystallites that are a bit misoriented), interface roughness, and growth rate fluctuations can be made. If mosaic spread occurs, the peaks will be horizontally broadened and tilted. If interface roughness occurs, the peaks are horizontally broadened, and with higher SL peak order become broader. Finally, if fluctuations in the growth rate occur, the peaks will be elongated vertically, which also increases with increasing SL peak order. For both interface roughness and growth rate fluctuations the zero-th-order SL peak are unaffected.
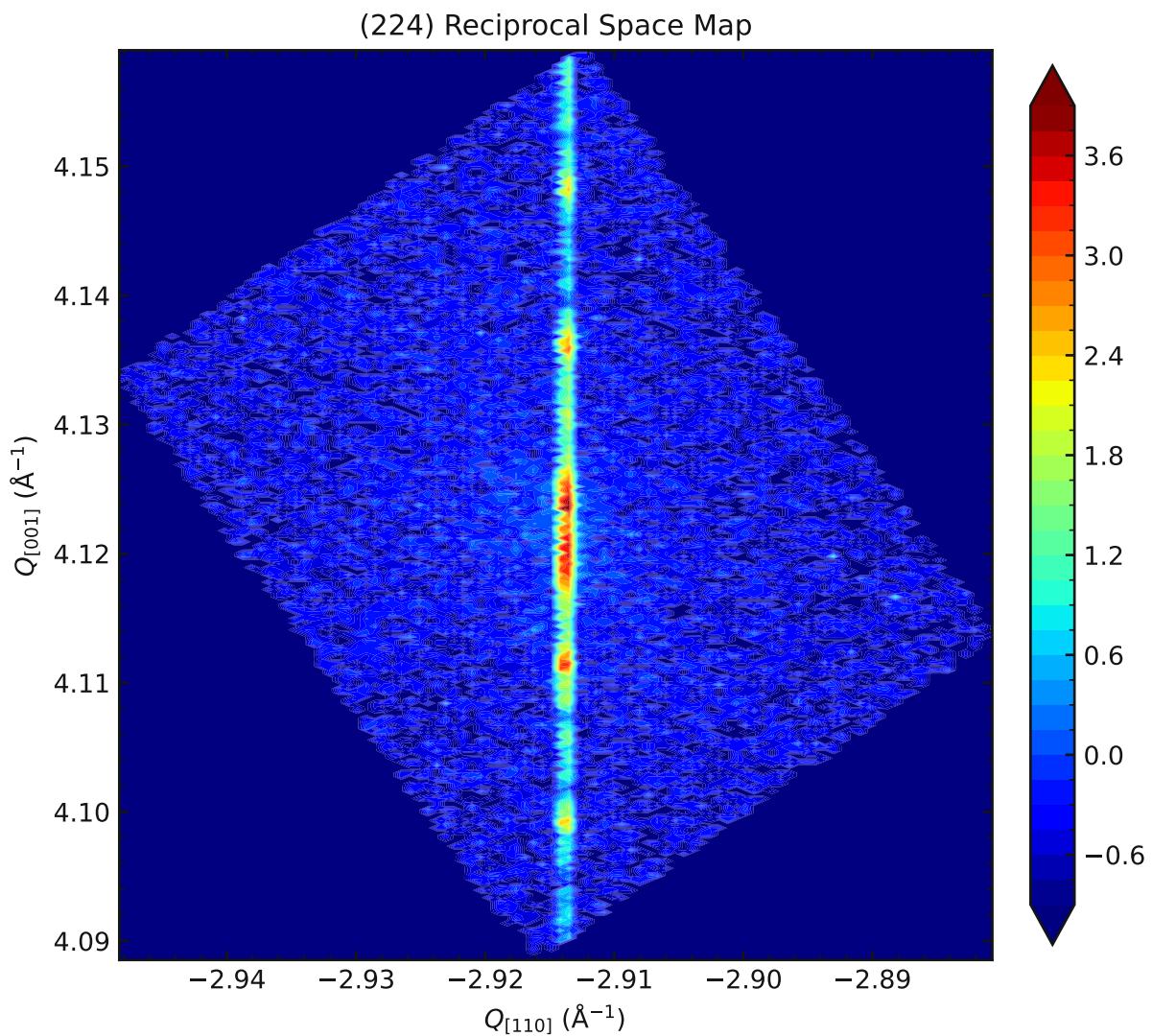
Figure 3.33: Reciprocal space map of the $(2\,2\,4)$ plane of an InAs/AlSb QCD. It shows a perfectly strain-balanced device. The SL peaks show no sign of a mosaic spread, interface roughness, or growth rate fluctuations.

3.5.3 Atomic force microscopy (AFM)

AFM produces high-resolution images of surface topographies [117] that can resolve sub-monolayer roughness. This is done by detecting the mechanical force that the surface imposes on the tip of a cantilever, where the displacement of the cantilever is usually optically detected, see Fig. 3.34. Non-conducting samples can be measured. AFM can be operated in ambient conditions as well as in UHV, or cryogenic conditions.

There are different operating modes for AFM:
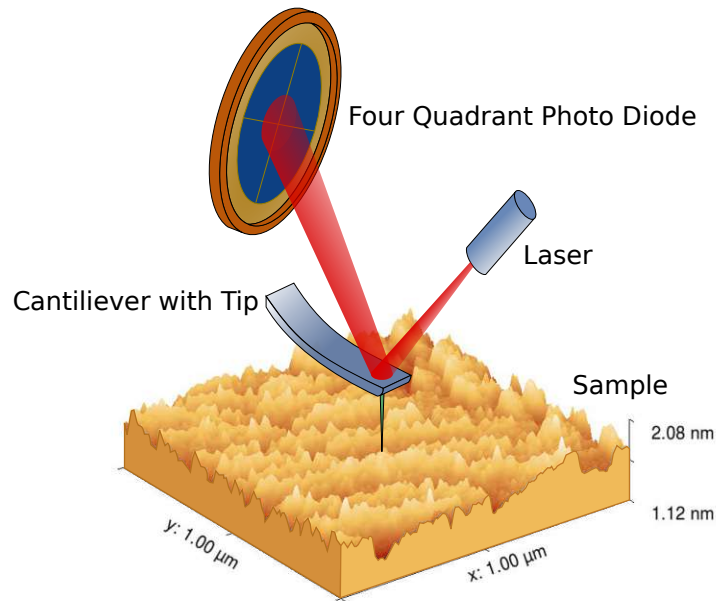
Figure 3.34: Sketch of the working principle of an AFM. The oscillations of a cantilever are measured in this setup with a laser and a four-quadrant photodiode. (Reprinted with permission from [93].)

Contact mode:

In this mode, the AFM tip is moved across the sample surface and maintains constant height. The force on the cantilever stems from the repulsive interaction due to the Pauli exclusion principle and the attractive van-der-Waals interaction if the tip is too far away. In the contact mode the wave functions of the tip (which has a single atom sitting on the top in the ideal case) and the surface overlap and repel each other. This produces high powers in the order of magnitude of 10^{-10} N, which can cause damage to the sample.

Intermittent-contact mode or tapping mode:

In this mode, the cantilever oscillates with a constant amplitude close to its resonance frequency, which is dampened when the tip touches the surface.

<div align="right">

CHAPTER 4

</div>

<div align="center">

InAs/Al(As)Sb quantum cascade detectors

</div>

This chapter covers the design, growth analysis, fabrication, and optical characterization of quantum cascade detectors (QCDs) based on the InAs/Al(Sb)As material system, which can be grown either lattice-matched to InAs substrates or strain-balanced to GaSb substrates.

4.1 Motivation

Performance metrics of QCDs are primarily the responsivity and detectivity, which were discussed in section 2.5. Both parameters can be optimized with the QCD band structure design. While design trade-offs impose limits between maximum responsivity and detectivity, such as the number of periods, other optimization limits are material-intrinsic. For example, both the responsivity and the detectivity can be increased by a lower effective electron mass m_e^* of the well material. The responsivity increases because the optical transition strength improves, see equation 2.23. The detectivity improves because the scattering rates are decreased, leading to lower noise and higher resistance, see equation 2.33.

Important parameters of different material systems used for QCDs designs are given in table 4.1. While the first intersubband (ISB) transitions were observed for the material system GaAs/Al_xGa_{1-x}As [118, 119], the most widely used system for QCDs is the InP-based lattice-matched $In_{0.53}Ga_{0.47}As/In_{0.52}Al_{0.48}As$ material system [16, 68], where the conduction band offset (CBO) of $0.52\,eV$ that can be extended up to around $0.61\,eV$ in the strained case and to $0.68\,eV$ when using InAs [120] limits

Material system	Well m_e^* (m_0)	CBO (eV)	E(LO-phonon) (meV)	Substrate	E_g (eV)
$In_{0.53}Ga_{0.47}As/In_{0.52}Al_{0.48}As$	0.043	0.529–0.61	34	InP	1.42
$In_{0.53}Ga_{0.47}As/AlAs_{0.56}Sb_{0.44}$	0.043	1.48	34	InP	1.42
$GaAs/Al_xGa_{1-x}As$	0.0675	148–357 (15–45% Al)	36	GaAs	1.519
InAs/AlSb	0.026	2.14	30	GaSb	0.812
$InAs/AlAs_{0.16}Sb_{0.84}$	0.026	2.28	30	InAs	0.417
$GaN/Al_xGa_{1-x}N$	0.2	1.8x	91	GaN	3.51
$ZnO/Mg_{0.3}Zn_{0.7}O$	0.24	0.414	72	ZnO	3.37
$Zn_{0.51}Cd_{0.49}Se/Zn_{0.29}Cd_{0.26}Mg_{0.45}Se$	0.13	1.1	35	InP	1.42

Table 4.1: Summary of important parameters for material systems used for QCD designs. Given are the effective electron masses m_e^* in the well and the longitudinal optical (LO)-phonon energies of the well material. The CBO is given at the Γ-point, and the bandgap of the substrate is E_g. On InP InAlAs/InGaAs can be either grown lattice-matched or strained, like this the CBO can be extended [120, 127]. The parameters are from [25, 79].

this system to detectable wavelengths of $\geq 4\,\mu m$. As discussed in section 2.5.5, the advantage of QCDs, over other photodetectors is the desingable, high-speed, narrow-band detection. To explore shorter wavelengths, one has to use material systems with a higher CBO, which is also beneficial for longer wavelength QCDs because the noise is reduced due to lower leakage current / increased resistance of the high barriers. GaN- and ZnO-based systems, belonging to the III-nitrite and II-VI semiconductors, offer high CBOs and no leakage into satellite valleys due to direct and large band gaps. The latter is important for high-temperature operations [121]. For GaN-based QCDs, the shortest QCD wavelengths have been demonstrated [122, 123], see section 2.5.4. Only since recently native GaN substrates exist with high quality, before that, growth was challenging due to a high threading dislocation density in the substrates [124]. On $[0\,0\,0\,1]$ grown films, internal fields exist in GaN due to its polar growth direction, complicating designs.

Coming back to As- and Sb-based semiconductors, barrier alloys with AlSb yield high CBOs. The $In_{0.53}Ga_{0.47}As/AlAs_{0.56}Sb_{0.44}$ material system grown lattice matched to InP obtained absorption wavelengths of $2.14\,\mu m$ [125]. Material systems that rely on InAs as a well material are promising because InAs offers one of the lowest m_e^*, half of that of InP and one-tenth of that of ZnO [126]. The InAs/Al(As)Sb material system additionally offers a high CBO, $2.28\,eV$ at the Γ-point and $1.35\,eV$ to the L-valley [25]. Due to the low effective electron mass of InAs, the levels inside the quantum well move further apart at the same well thickness compared to materials with higher m_e^*, meaning that InAs wells designed for a specific absorption wavelength are thicker compared to materials with higher m_e^*. This gives an advantage in growth due to higher growth tolerances for short wavelength QCDs (where wells need to be thinner) but also for MIR QCDs.

4.2 InAs versus GaSb substrates for QCDs

Both InAs and GaSb substrates have advantages and disadvantages for the growth of InAs/Al(As)Sb based QCDs. On InAs substrates, InAs/AlAs$_{0.16}$Sb$_{0.84}$ can be grown lattice-matched, which reduces the probability of generating defects because layers can be grown strain free. Furthermore, there is no limit due to a critical layer thickness, giving an additional degree of freedom in the design of the structure, because well and barrier materials do not need to be strain balanced to each other. On the other hand, due to the small InAs bandgap of 0.417 eV, the substrate becomes absorbent with wavelengths below 2.97 μm. To utilize the enormous CBO of 2.28 eV at the Γ-Point and 1.35 eV to the L-valley of the InAs/AlAs$_{0.16}$Sb$_{0.84}$ material system, one would need to either remove the substrate or use top-side illumination. In section 2.5 it was discussed that QCDs are only sensitive to an electric field polarized in the growth direction (TM), which limits the surface normal illumination design to some sort of diffraction design and this complicates the fabrication. An advantage of GaSb substrates is the larger bandgap of 0.812 eV, being transparent for wavelengths down to 1.52 μm. GaSb-based QCDs can therefore be fabricated in the standard double-pass 45° facet method, where the illumination occurs through the substrate.

On GaSb, InAs/AlSb can be grown strain balanced, where InAs has a tensile mismatch of 0.62063 %, and a critical layer thickness of 36 nm and AlSb has a compressive mismatch of -0.64542 % with a critical layer thickness of 35 nm, calculated with the formula of Matthews and Blakeslee's [91]. Therefore the InAs/AlSb ratio for a strain-compensated growth is 0.9615:1. Meaning that to strain-compensate the QCD the AlSb barriers would be needed to be grown almost as thick as the InAs wells. This limits the design possibilities enormously, making it impossible to optimize the QCD design, especially because the AlSb barriers need to be grown thinner than for InP based designed due to the high CBO. One trick lies in the utilization of sub-monolayer thick InSb interfaces (mismatch of -5.9187 % to GaSb), which is discussed in more detail in section 4.4.4. Still, the growth is more challenging because of the two different group-V materials in the two layers. The As-for-Sb exchange (see section 3.4.4), and inter-diffusion of the layers have to be completely prevented to stay strain-balanced and ensure a defect-free growth that corresponds to the calculated design, see section 3.4.4.

4.3 InAs/AlAs$_{0.16}$Sb$_{0.84}$ QCD on InAs working at 2.7 µm

As the growth itself of this material system is discussed in section 3.4.4, here the discussion will focus on the design, growth analysis, fabrication, and characterization of the QCD. The results presented in this section are partly based on the publication by M. Giparakis, et al.; "2.7 µm quantum cascade detector: Above band gap energy intersubband detection". Appl. Phys. Lett. 120 (7): 071104. (2022) [81].

4.3.1 Band structure design

The band structure was simulated using an in-house simulation tool, capable of performing simulations in the 8-band k·p-formalism. The tool includes scattering mechanisms such as LO- and acoustic-phonon scattering, interface roughness scattering, and alloy scattering.
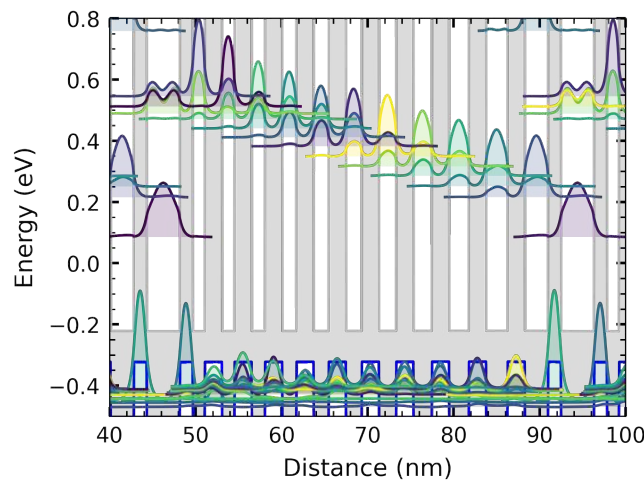
Figure 4.1: Band structure of the QCD detecting at 2.7 µm. The layer thicknesses are in nm as follows: **1.50**, 1.38, **2.00**, 1.43, **2.00**, 1.55, **2.00**, 1.65, **2.00**, 1.75, **2.00**, 1.85, **2.00**, 2.00, **2.00**, 2.15, **2.00**, 2.30, **2.00**, 2.50, **2.00**, 2.70, **1.50**, and 3.85. The boldly printed layers represent the AlAs$_{0.16}$Sb$_{0.84}$ barriers. The underlined well is doped 3×10^{18} cm^{-3}. This QCD is published in [81]. Figure adapted from [81].

Fig. 4.1 shows the band structure with the carrier probability densities of the QCD working at 2.7 µm. The conduction band is plotted in dark grey, the valence band in blue, and the band gap in light grey. The optical transition takes place in the widest well from the ground state to the first excited state. For this design, the LO-phonon energy is employed in the extraction region, ensuring sub-picosecond scattering times. In the design, a vertical optical transition is implemented. This takes advantage of the

high optical transition energy of 0.459 eV of the QCD detecting at 2.7 µm, for which absorption efficiencies are reduced, but extraction efficiencies are increased. To ensure reduced back-filling, the lowest extractor state has an energy separation of more than 120 meV to the ground state, which also increases the lifetime in the ground level and benefits the absorption efficiency. Notice the thin barriers (1.5–2.0 nm), compared to conventional InP-based QCD designs, typically ranging from 3.0–6.5 nm [68]. Due to the high CBO, these thin barriers are needed for the InAs/Al(As)Sb material system to keep the extraction efficiency high. Thinner barriers also result in increased splitting of the energy levels, which have to be considered during the design. Due to the high absorption energy of 0.459 eV, the wells also become remarkably thinner, making the growth tolerances more demanding.

InAs/AlAs$_{0.16}$Sb$_{0.84}$ has a type-II band alignment of approximately 0.14 eV, see Fig. 4.1. If states are available in the barrier material valence band, strong interband absorptions in the near-infrared range (around 2 µm) are expected. The narrow wells needed for absorption at 2.7 µm lift the ground state of the optical transition up and effectively increase the bandgap, due to quantum confinement.

4.3.2 Growth analysis

In the following the growth of the QCD working at 2.7 µm is analyzed. The growth itself was discussed in section 3.4.4.
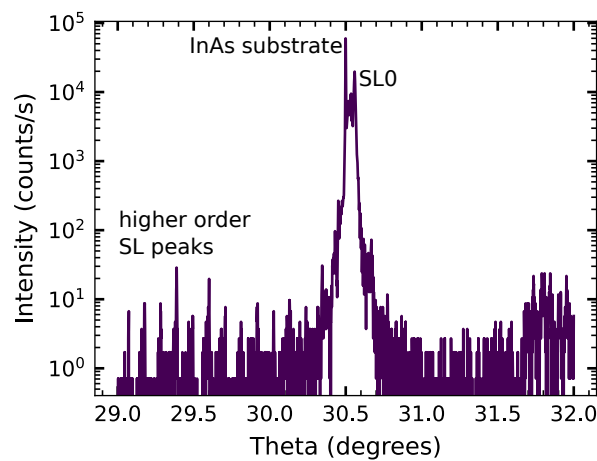
Figure 4.2: High-resolution X-ray diffraction (HR-XRD) of the grown QCD at 2.7 µm in the (0 0 4) ω-2θ scan. The InAs substrate and the superlattice peaks are marked, SL0 marks the 0th-order superlattice (SL) peak. Figure adapted from [81].

Fig. 4.2 shows the high-resolution X-ray diffraction (HR-XRD) of the grown QCD at 2.7 µm in the (0 0 4) ω-2θ scan, for an introduction into HR-XRD please refer to
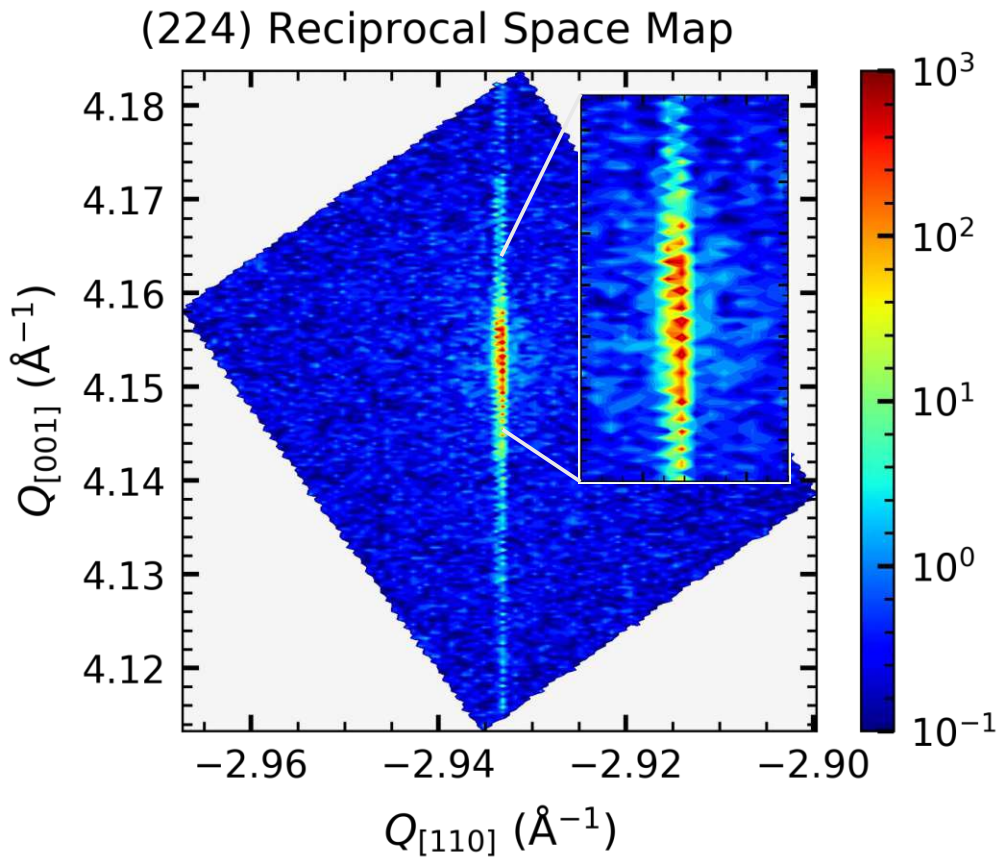
Figure 4.3: (2 2 4) reciprocal space map of the grown QCD at 2.7 μm. No growth rate fluctuations, interface roughness, or mosaic spread is apparent from this scan. The contour pattern is influenced by image processing. The intensity contours are in one straight vertical line indicating that no relaxation occurred.

section 3.5.2. The position of the zero-th-order SL peak indicates lattice matching between the grown structure and the InAs substrate. From the distance to the substrate peak, a lattice mismatch of 0.173% can be calculated. The higher order SL peaks have a mean full width at half maximum (FWHM) of 20.268 arcsec, while the simulation gives a mean FWHM of 15.696 arcsec. The growth results need to be in comparison to the material quality of the substrate, where a (0 0 4) HR-XRD measurement of an InAs substrate gave a FWHM of 14.4 arcsec of the substrate peak. The results indicate sharp interfaces, and therefore low interface roughness or layer inter-diffusion. The growth thickness of the active region is 1.443 μm (30 periods), over which no growth rate deviations are expected nor observed from the HR-XRD, which would show up as broadening or splitting of higher order superlattice peaks. Fig. 4.3 shows the (2 2 4) reciprocal space map (RSM) of the QCD, which gave no indication of growth rate fluctuations, interface roughness, or mosaic spread. The

contour pattern observed is related to image processing, due to the reciprocal space not being a perfect grid. Furthermore, the vertical line of the intensity contours indicates that no relaxation of the film occurred, see section 3.5.2 for a discussion on conclusions that can be drawn from RSM scans.
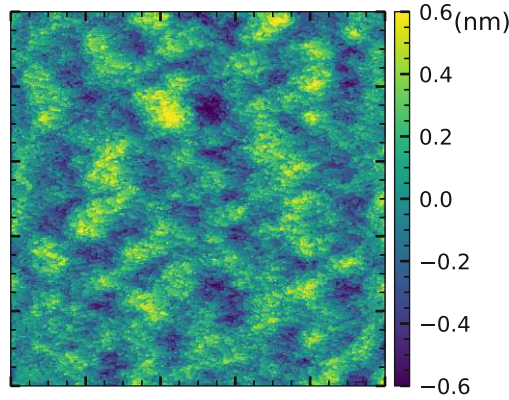
Figure 4.4: 10×10 µm AFM scan of the InAs/AlAs$_{0.16}$Sb$_{0.84}$ QCD. The measured root mean square (RMS) surface roughness is 0.228 nm.

Fig. 4.4 shows the 10×10 µm atomic force microscopy (AFM) scan of the QCD, from which step flow growth can be observed. An RMS surface roughness of 0.228 nm was measured, which is not significantly rougher than a commercially available InAs substrate with an RMS surface roughness of approximately 0.2 nm. This indicates low growth roughness.

4.3.3 COMSOL simulations: designing a diffraction grating

QCDs are usually characterized using the double-pass 45°-facet method, illuminating the QCD through the substrate, see section 2.5.3. This is not possible in this case, because the bandgap energy of the InAs substrate lies below the designed absorption energy of the QCD, which would cause absorption of the designed absorption wavelength by the substrate. Therefore top-illumination is required, but as discussed in section 2.2.2, QCDs follow the intersubband transition selection rule, allowing only light polarized in the growth direction to be detected. This is the reason why a diffraction grating is employed, see section 2.5.3 for an introduction. It had to be determined if the designed absorption wavelength of the QCD corresponds to the absorption wavelength of the real grown device. For this, cleaved side facets were fabricated in a quick wet-etching process according to the instruction of [128] and characterized with a Fourier-transform infrared spectrometer (FTIR) according to section 2.6. Once the peak responsivity was confirmed to match the design, 2-D

COMSOL simulations with "electromagnetic waves frequency-domain" physics and a "frequency-domain" study were employed. The active region of the QCD was probed for its absorbed power coming from an input port in the air above the grating. Initial simulations showed that it is beneficial if the grating is etched directly into the active region of the QCD, see inset of Fig. 4.5 of the transverse scheme of the top-illuminated QCD with a diffraction grating. The red arrows indicate the illumination direction. The black layers are the grown top and bottom contact layers. The cyan layer is the passivation and the yellow layers the fabricated top and bottom contacts.
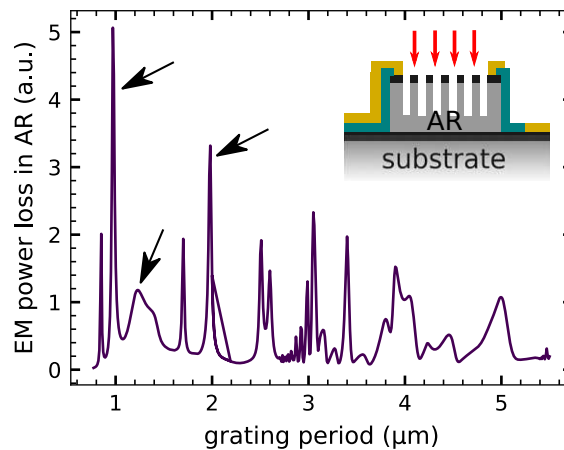
Figure 4.5: COMSOL simulation of the absorption of incident light with a wavelength of 2.7 µm in the active region plotted over the grating period sweep. The inset is reprinted from [81] and shows a sketch of the transverse device scheme. The black layers above the substrate and above the active region (AR) are the doped contact layers. The cyan layer is the Si_3N_4 passivation and the yellow layers are the top and bottom Ti/Au contacts. The red arrows indicate the illumination direction.

Fig. 4.5 shows a sweep over the grating period vs. the absorbed power in the active region. From the parametric grating sweep, three grating periods were chosen for fabrication, which are marked with arrows: 0.97 µm, 1.24 µm, and 1.98 µm. The grating period of 1.24 µm was chosen because it shows a broader absorption, making it more tolerant to deviations in fabrication, while other grating periods would show higher absorption.

Parametric sweeps for each chosen grating period over the grating depth were performed, see Fig. 4.6. The simulations show that the absorption is dependent on the etch depth and it is apparent, that a small window in the etch depth of about 50 nm exists to hit optimal parameters. The black vertical line in Fig. 4.6 indicates the real etch depth in the final fabricated devices.

A sweep over the duty cycle yielded the best results for a duty cycle around 0.5 for all three grating periods.
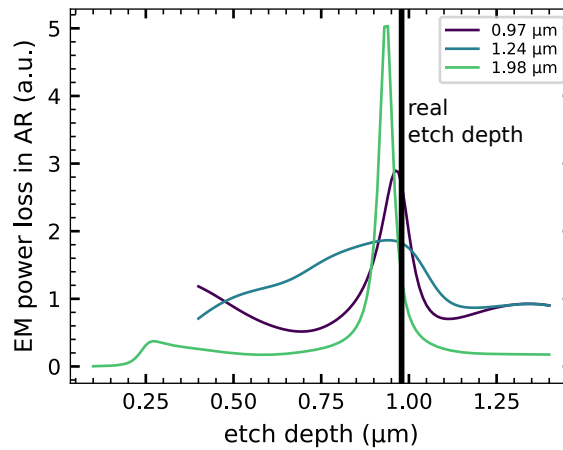
Figure 4.6: COMSOL simulation of the absorption in the active region plotted over a sweep of the etch depth. Note the small etch depth window for best results. The vertical black line indicates the real etch depth of the processed devices.

4.3.4 Fabrication of a top-side illuminated QCD

In the following the fabrication of the top-side illuminated InAs/AlAs$_{0.16}$Sb$_{0.84}$ QCD is discussed. Fig. 4.7 depicts a schematic of the entire process.

As a first step a) the 10×10 mm sample is cleaned first in acetone and then in isopropyl alcohol to remove cleaving dust and surface contamination. If necessary, this is done in an ultrasonic bath. In the next step b), Si$_3$N$_4$ is deposited as a hardmask with plasma enhanced chemical vapor deposition (PECVD). Next c), the hardmask is defined using optical lithography. The hardmask is dry-etched in an inductively-coupled plasma (ICP)-reactive ion etching (RIE) chamber using CHF$_3$ and O$_2$, d). This is an anisotropic process and leads to straight sidewalls. The photoresist is then removed using an O$_2$ plasma and subsequently with acetone and isopropyl alcohol, e). Now the mesas can be defined in the ICP-RIE with a Cl/Ar-process, f), etching down until the bottom contact, yielding vertical smooth, slightly positive sloped sidewalls. This process needs multiple steps, as the etch rate has to be monitored with a stylus profiler to stop the etch within the bottom contact. Subsequently, the Si$_3$N$_4$ hardmask is removed in the RIE with an SF$_6$ process, g). In the next step, the lithography for the grating on the mesas is performed. For this, a Si$_3$N$_4$ hardmask is deposited again, h). Afterwards, the lithography for the grating is performed, i). The three different grating periods were defined with electron beam lithography (EBL). The hardmask is dry-etched in an ICP-RIE chamber using CHF$_3$ and O$_2$, j). The photoresist is removed, k). The sample is etched again with the same Cl/Ar-process for which the mesas were defined, l). In section 4.3.3 COMSOL simulations showed that the grating etch depth needs to be accurate for optimal
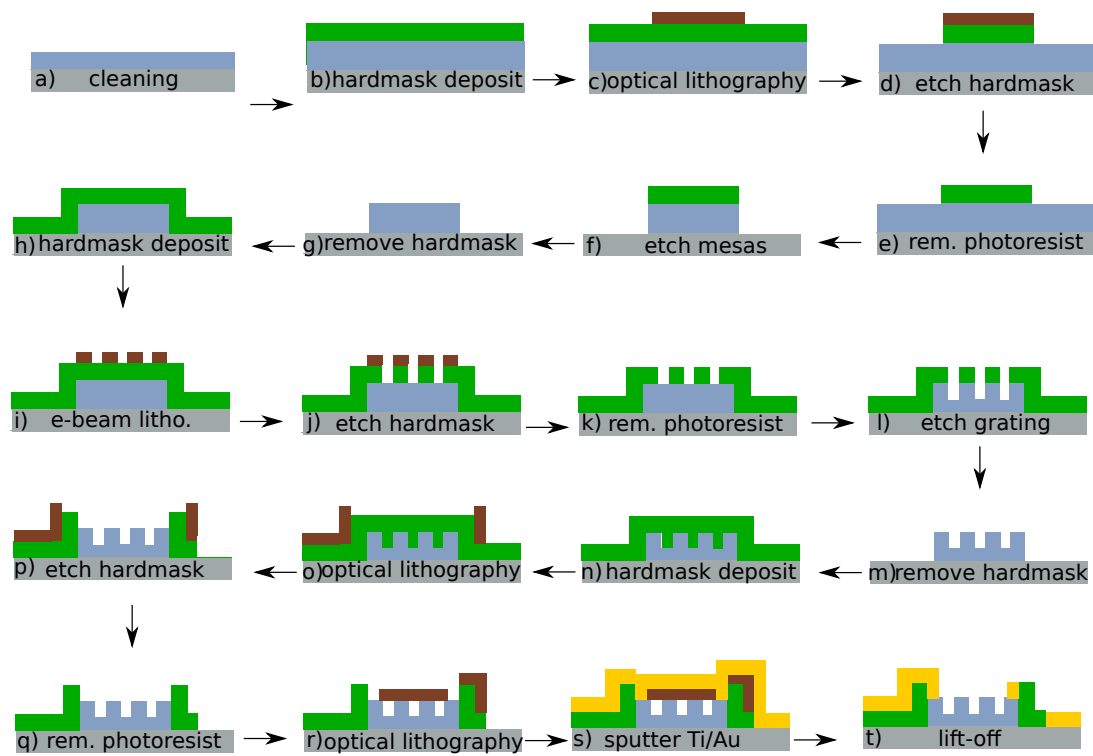
Figure 4.7: Sketches of the transverse device scheme that depict conducted fabrication steps. The gray layer is the substrate. The blue layer is the active region. The Si_3N_4 hardmask/passivation is drawn in green. The photoresist is depicted in dark red and the Ti/Au contacts in yellow.

performance. Due to the small dimensions of the trenches, the etch rate is different from before and can not be checked during the etch process with a stylus profiler. Therefore, the etch rate was determined beforehand by performing the same process on a test sample and cutting through the grating with a focussed ion beam (FIB), see inset of Fig. 4.8. The etch depth was optimized for the grating with a period of $0.97\,\mu m$ and was measured to be $980\,nm$ deep. This is close to the desired etch depth of $960\,nm$ and means that the grating was etched through the $60\,nm$ top contact and through 20 periods of the active region, leaving ten periods untouched. Then the hardmask is removed again, m), with a combination of CHF_3 and O_2 and SF_6 to efficiently remove the Si_3N_4 from the trenches. Again Si_3N_4 is deposited, this time, it acts as electrical passivation, n). Optical lithography is performed to open the passivation at the top and bottom contacts, o). In the next step, the passivation is dry-etched using CHF_3 and O_2, p), and the photoresist is removed, g). Again optical lithography is performed to define the mask for the top and bottom contacts, r). Then Ti/Au contacts are sputtered, s), and a lift-off in acetone is performed, t).

Fig. 4.8 shows an optical image of the finished device. The grating is etched directly into the active region, see inset, and is surrounded by the top contact, which is
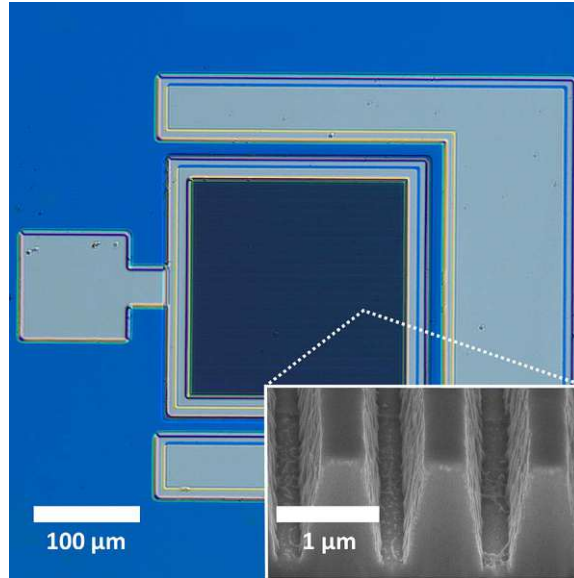
Figure 4.8: Optical picture of the finished fabrication of a mesa with a 200×200 μm surface grating, which is framed by the top contact that is extended to the left. The bottom contact frames the mesa on three sides. The grating, which is etched directly into the active region is magnified in a scanning electron microscope (SEM) image at the right bottom of the image.

extended on top of the Si$_3$N$_4$ passivation. The mesa is surrounded on three sides by the bottom contact.

For the finished device of the QCD detecting at 2.7 μm , the gratings are etched over an area of 50×50 nm, 100×100 nm, 150×150 nm, and 200×200 nm. The process includes three different grating periods: 0.97 μm, 1.24 μm, and 1.98 μm. The framing top contact is additionally 20 nm in width, making the mesa 40 nm longer per side than the surface grating.

4.3.5 Optical characterization

The QCD was optically characterized with an FTIR and a Globar source, as described in section 2.6 to measure the responsivity and detectivity. A long-pass filter with a specified cut-on wavelength of 2.4 μm, 4166 1/cm (or cut-off at 2.5 μm, 4000 1/cm) was used for some measurements to block nearby higher energy interband transitions that will be discussed in section 4.4.4.

For each of the three different grating periods, 3–5 200×200 μm devices were measured, and for the 0.97 μm grating period 3–5 devices of the different mesa sizes were measured. These measurements were conducted at ambient conditions. For a device with a grating period of 0.97 μm, a surface grating area of 200×200 μm, and at ambient conditions, a responsivity of 5.63 mA/W at 2.73 μm (3650 1/cm)
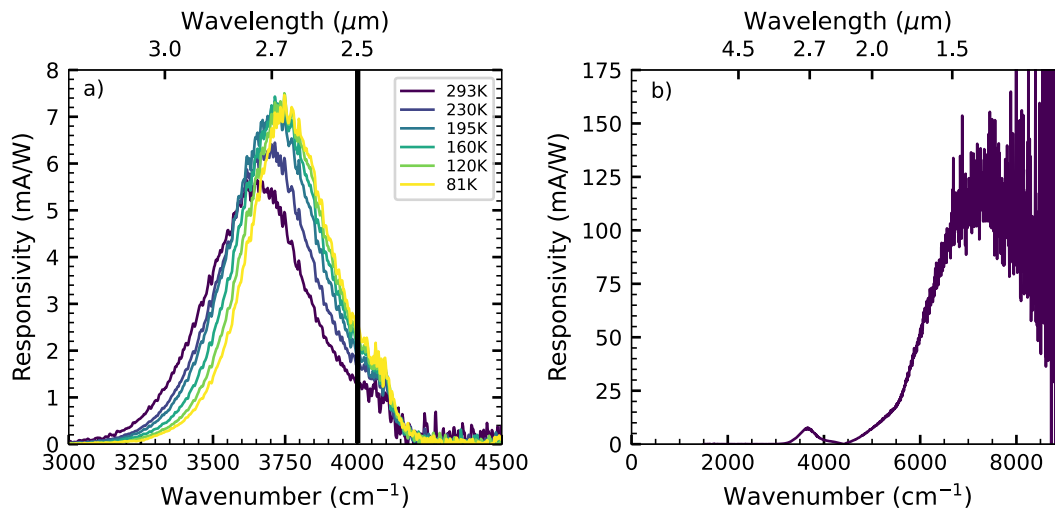
Figure 4.9: a) Temperature-dependent responsivity measurement of a $200{\times}200\,\mu m$ surface grating mesa. The black vertical line depicts the cut-off of the utilized long-pass filter. b) Responsivity measurement of a $200{\times}200\,\mu m$ surface grating mesa at ambient conditions without the long-pass filter. The full spectrum reveals a strong absorption signal to the right of the QCD signal stemming from interband absorptions. The intense noise in b) is due to the Globar source having almost no signal at short wavelengths.

was measured, while for the interband signal, the responsivity is almost an order of magnitude higher. The QCDs temperature-dependent responsivity was also measured in a cryostat down to 80 K, see Fig. 4.9 a), where a maximum responsivity of 7.49 mA/W at 80 K was measured. Note both the blue shift of the responsivity and minimal temperature dependence at temperatures from 200–80 K. To compensate for the reduced transmission of the cryostat window and shadowing effects, the temperature-dependent measurements were scaled according to the measurement of the same device at ambient conditions.

Measurements without the long-pass filter revealed a broadband interband absorption occurring from 1.17–2.27µm (4400—8500 1/cm), see Fig. 4.9 b). A comparison to the Globar signal (see Fig. 2.17 in section 2.6) shows that the Globar has almost no intensity in this range anymore, which explains the intense noise observed in Fig. 4.9 b). The origin of this interband signal is discussed in section 4.4.4. The black vertical line in Fig. 4.9 a) corresponds to the long-pass filter cut-on. Fig. 4.10 shows the temperature-dependent photocurrent measurement of the QCD, including the interband signal. The obtained spectrum was normed by the Globar spectrum and to unity. A blue shift of the interband signal is apparent. Except for the measurements at 120 K, and 160 K the photocurrent increases with temperature and is the highest for 300 K, which is in contrast to the temperature-dependent trend of the QCD signal
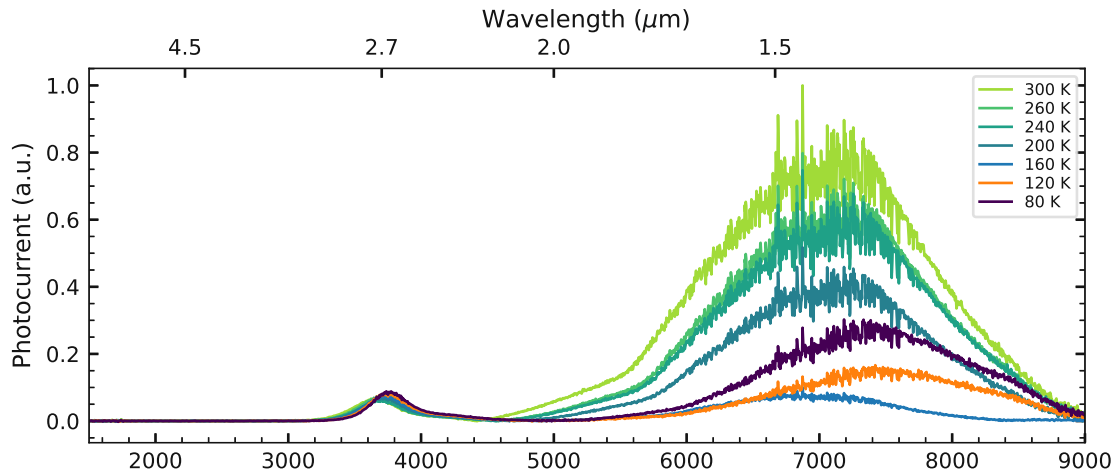
Figure 4.10: Temperature-dependent photocurrent measurements of the QCD detecting at 2.7 µm. In contrast to the QCD signal, the photocurrent of the interband signal ranges from 1–2 µm is increasing with the temperature, except for the measurements at 120 K and 160 K. The photocurrent was normed by the Globar spectrum and to unity.

at 2.7 µm.
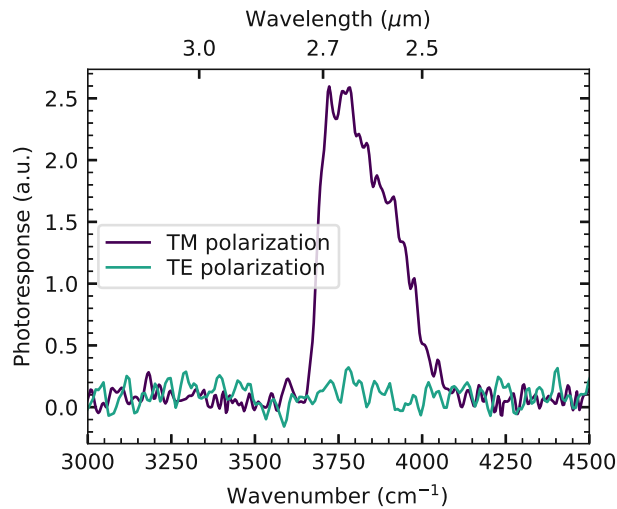
Figure 4.11: A cleaved side-facet of a mesa-only (no grating) fabrication of the QCD absorbing at 2.7 µm was measured with light polarized parallel (TM polarization) or normal (TE polarization) to the growth direction. There is no photoresponse of the QCD for the second case. The slight cut-off of the photoresponse towards longer wavelengths is attributed to a different used lens optimized for near-infrared wavelengths.

Polarisation-dependent measurements were conducted to confirm the intersubband nature of the QCD at 2.7 µm, see Fig. 4.11, which is also apparent by the narrow

band signal. The polarisation-dependent measurements were conducted on cleaved side facets of a different fabrication of the QCD that were processed without a diffraction grating. For these devices, the mesa surface was a Ti/Au top contact, and the bottom contact was on the backside of the substrate.
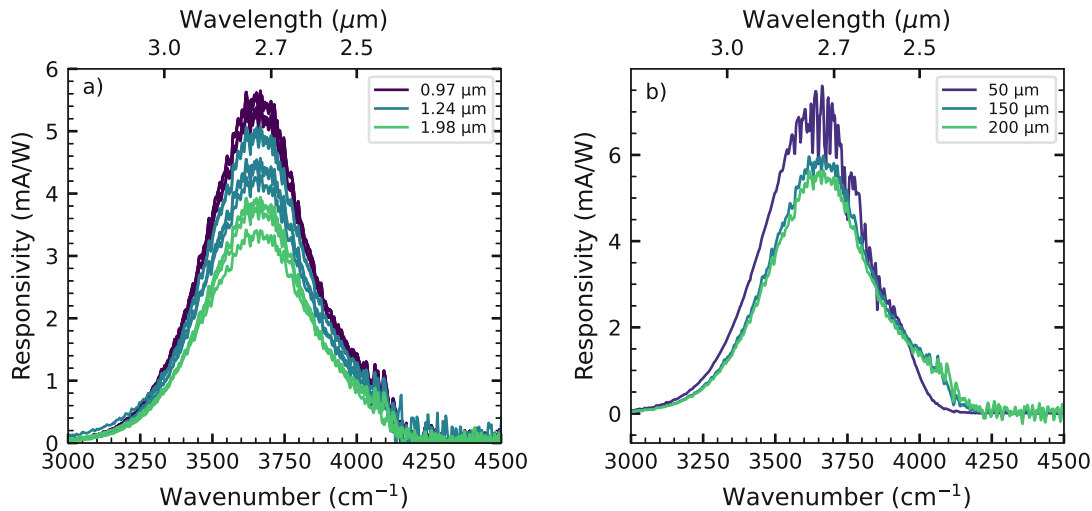
Figure 4.12: a) The responsivities measured at ambient conditions for a $200{\times}200\,\mu m$ surface grating device and the three different grating periods are compared. For each grating period multiple devices were measured, which are plotted in the same color. b) The responsivities measured at ambient conditions for devices with a grating period of $0.97\,\mu m$, and three different surface grating sizes are compared.

Fig. 4.12 a) shows the measured responsivity for the three different grating periods. Compared to the COMSOL etch depth-dependent simulations for each grating, see Fig.4.6, the responsivity is in agreement with the simulation at the real etch depth, which is marked with a black line in the simulation. The grating period of $0.97\,\mu m$ performs the best, followed by the $1.24\,\mu m$, and the $1.98\,\mu m$ grating periods.

Fig. 4.12 b) shows the measured responsivity for the different surface grating sizes. No data for the $100{\times}100\,\mu m$ devices exists because all devices are shorted. The $50{\times}50\,\mu m$ devices show the highest responsivity.

Fig. 4.13 shows the dependency of the interband signal of the QCD on the grating period. The photocurrent was normed by the Globar spectrum. Equally to the QCD signal, the grating period of $0.97\,\mu m$ performs the best, followed by the $1.24\,\mu m$, and the $1.98\,\mu m$ grating periods.

Fig.4.14 a) shows the temperature-dependent I-V characteristics of a $200{\times}200\,\mu m$ surface grating mesa. Room-temperature I-V characteristics of the different surface grating sizes were measured and are divided in Fig.4.14 b) by their area and in Fig.4.14 c) by their circumference. For the $200{\times}200\,\mu m$ and the $150{\times}150\,\mu m$ devices
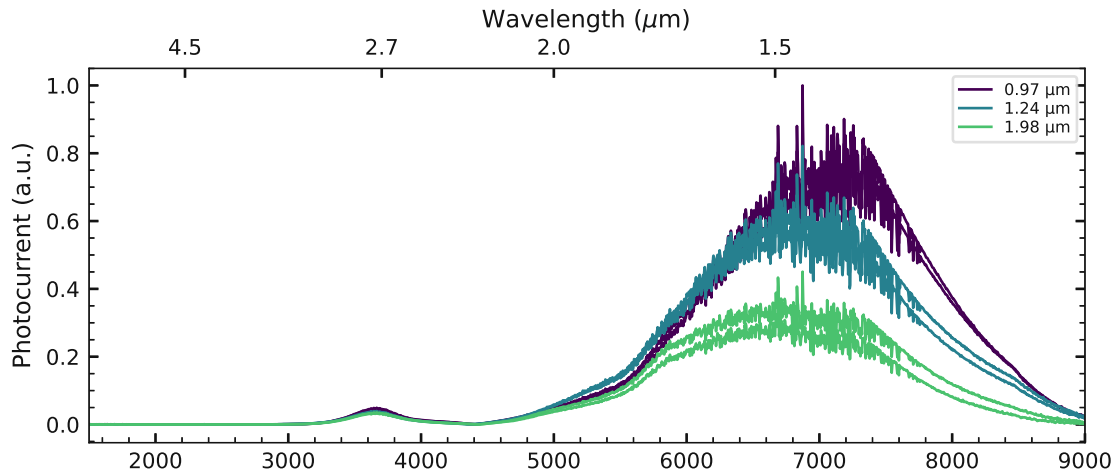
Figure 4.13: Photocurrent dependency of the interband signal of the QCD on the grating period. Measurements of two devices are plotted for each grating period. The photocurrent was normed by the Globar spectrum and to unity.
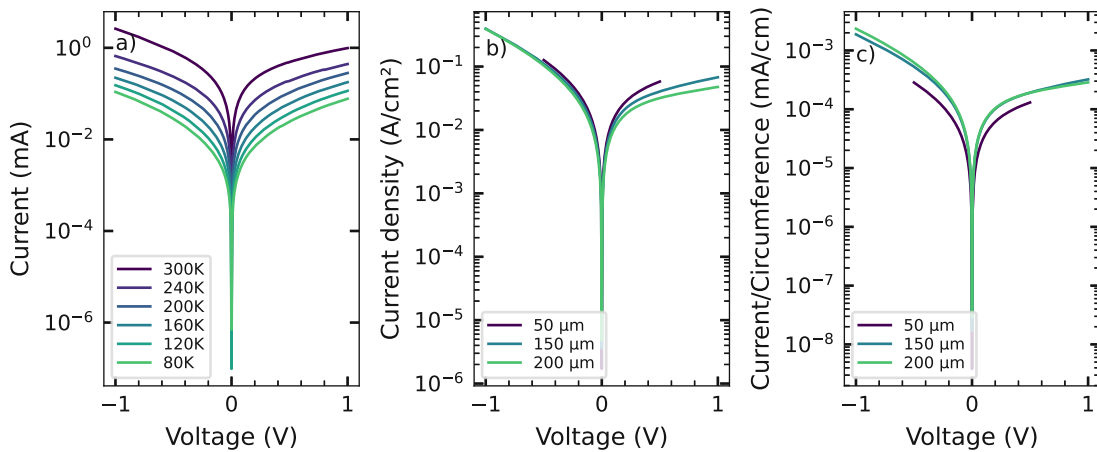
Figure 4.14: a) Temperature-dependent current-voltage (I-V) measurements of a 200×200 µm surface grating device. b) and c) I-V measurements at ambient conditions for the three different surface grating sizes, where the b) plots the current density and c) the current divided by the circumference over the voltage.

the current scales with the mesa circumference and not their area. This indicates surface leakage, a problem that would need to be solved for future projects.

The specific detectivity can be calculated from the responsivity and the I-V characteristics using eq.2.34. For this, the differential resistance at zero voltage was extracted from the I-Vs. Fig. 4.15 shows the temperature-dependent detectivity, which is 1.37×10^8 Jones at room temperature, again for the interband signal the room temperature detectivity is approx. one order of magnitude higher. To the right y-axis, the differential resistance and electrical area product $R_0 A$ is plotted over the

temperature to which an activation energy can be fitted/calculated to be 265 meV.
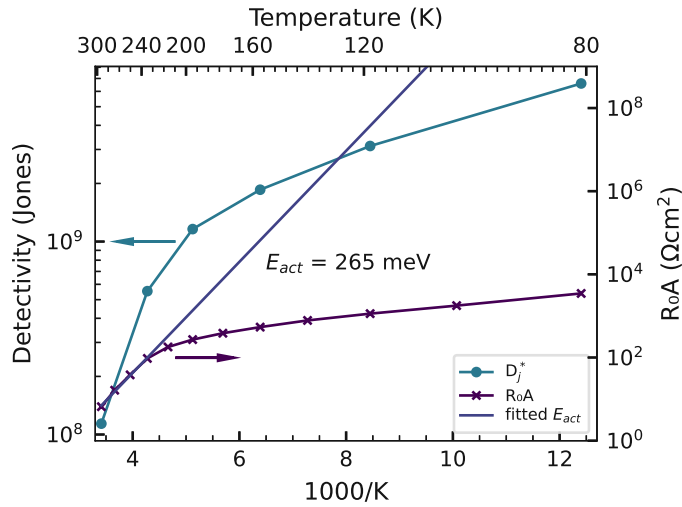
Figure 4.15: Plot of the temperature-dependent specific detectivity (left y-axis) and the R_0A product (right y-axis) for which an activation energy of 265 meV can be fitted/calculated. Figure adapted from [81].

4.4 InAs/AlSb QCDs strain balanced to GaSb substrates

The growth of the InAs/AlSb material system was discussed in section 3.4.5. In this section, the focus lies on the band structure design, growth analysis, fabrication, and characterization of these QCDs.

4.4.1 Band structure design for QCDs absorbing at a target wavelength between 3.7–5.5 μm

The QCDs on GaSb were designed with similar considerations as for the QCDs grown on InAs, described in section 4.3.1. The significant difference in designs for GaSb substrates is that strain balancing needs to be considered, which effectively reduces the degrees of freedom in design. Due to the mismatches between GaSb and InAs (0.62063%) and AlSb (-0.64542%), the strain-balanced InAs:AlSb ratio is 0.9615:1. This means that maintaining strain balance would result in approximately the same thickness barriers as wells. Considering that well thicknesses for a QCD design detecting at 4.3 μm range between 2.95–7.2 nm, this strategy is impractical, since thick AlSb barriers would drastically reduce the extraction efficiency. The solution

lies in the interfaces. Since InAs and AlSb consist of different group V materials after the growth of an InAs layer either an InSb or an AlAs interface can form. Studies found superior carrier mobility with the formation of InSb interfaces [108]. The mismatch of InSb to GaSb is -5.9187%. This means that the growth of sub-monolayer thick InSb layers after the InAs wells can strain-balance a device optimized for high performance, where the InAs:AlSb ratio is closer to 3:1. This gives back the freedom one would have with lattice-matched materials in the design. Additionally, this design step results in the formation of the preferred InSb interfaces.

The critical layer thickness of InAs on GaSb is $35\,\mathrm{nm}$ according to eq. 3.10, this means that no single-crystal thick ($\geq 100\,\mathrm{nm}$) contacts can be grown, therefore a contact superlattice was designed. Additionally, the design needed transition layers from the GaSb substrate to the superlattice contacts. The grown QCDs on GaSb were doped in the InAs wells using Te from a GaTe cell. It is also possible to dope InAs with Si, like it was done for the QCD detecting at $2.7\,\mu\mathrm{m}$ grown on InAs, but Si is a p-dopant for the AlSb barriers, see section 3.3. By doping the structure with Te one excludes p-doping in the barriers due to dopant diffusion.
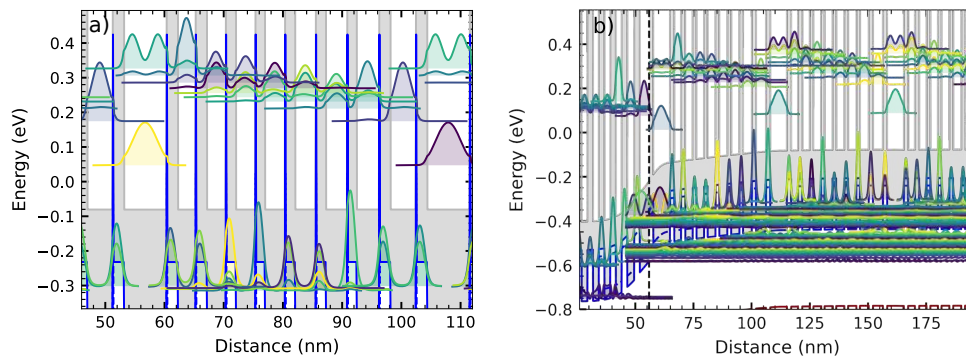
Figure 4.16: a) QCD band structure with a peak responsivity at $4.3\,\mu\mathrm{m}$. The layer thicknesses in nm are as follows: **1.80**, <u>7.20</u>, **1.80**, 2.95, **1.80**, 3.20, **1.60**, 3.30, **1.50**, 3.40, **1.60**, 3.50, **1.60**, 3.60, **1.50**, 3.80, **1.80**, and 4.30. The boldly printed layers represent the AlSb barriers. The underlined well is doped $8\times10^{17}\ 1/\mathrm{cm}^3$. b) The alignment of the active region to the superlattice contact is depicted. Notice the band bending at the interface. The black dashed line corresponds to a boundary in the simulation.

Fig. 4.16 a) shows the first design of a QCD detecting at $4.3\,\mu\mathrm{m}$ which incorporates InSb interface layers. The conduction band is drawn in grey and the valence band in blue. The blue peaks extending into the InAs conduction band stem from the InSb valence band. Note that the layer thicknesses are too small to allow states in the InSb to form. These layers have negligible influence on the level formation

itself. Fig. 4.16 b) shows the alignment with the contact superlattice. It is visible that band bending occurs at the beginning of the active region. To counteract level misalignment due to the band bending, the last few wells of the contact superlattice were designed wider to move the levels down. The black dashed line corresponds to a boundary in the simulation.
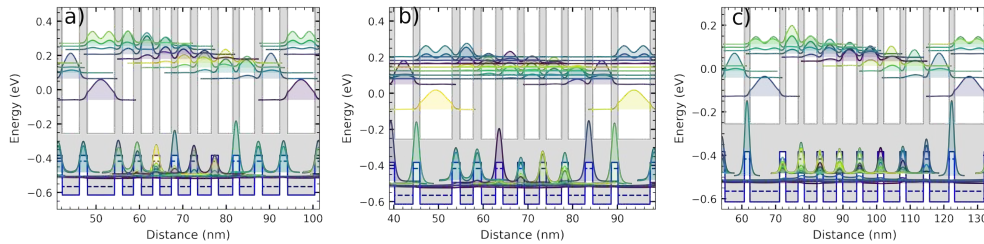
Figure 4.17: QCD band structures: a) Peak responsivity at 3.65 μm. The layer thicknesses are in nm as follows: **1.80**, <u>6.30</u>, **1.80**, 2.55, **1.80**, 2.65, **1.60**, 2.70, **1.50**, 2.90, **1.60**, 3.20, **1.60**, 3.35, **1.80**, and 4.0. b) Peak responsivity at 4.3 μm (this design will be referred to as 4.3b μm in the text). The layer thicknesses are in nm as follows: **1.50**, <u>7.20</u>, **1.80**, 2.95, **1.80**, 3.20, **1.60**, 3.30, **1.50**, 3.40, **1.60**, 3.50, **1.60**, 3.60, **1.50**, 3.80, **1.80**, and 4.30. c) Peak responsivity at 5.5 μm. The layer thicknesses are in nm as follows: **1.60**, <u>8.85</u>, **1.80**, 3.70, **1.80**, 3.80, **1.80**, 4.0, **1.80**, 4.20, **1.80**, 4.40, **1.80**, 4.80, **1.80**, 5.20, **1.80**, and 5.80. The boldly printed layers represent the AlSb barriers. The underlined well is doped 8×10^{17} 1/cm^3.

Fig. 4.17 shows the designs for the QCDs grown for absorption wavelengths of 3.7 μm, 4.3 μm (which is the second design at this wavelength, and will be referred to as 4.3b μm), and 5.5 μm, where the InSb layers are not plotted for easier readability.

4.4.2 Growth analysis

In the following, the growth of those devices is analyzed. The growth itself was discussed in section 3.4.5.

Fig. 4.18 shows the HR-XRD (0 0 4) ω-2θ scans of the grown QCDs. Section 3.5.2 gives an introduction to HR-XRD patterns and analysis.

The HR-XRD scans show the superposition of the active region (AR) with the contact SL, the latter having broader peaks because the SL contact layers are thin. Fig. 4.19 shows the (2 2 4) RSM scans of the QCDs. In RSM scans interface roughness and growth rate fluctuations would result in broadened peaks (in one case horizontally and in the other case vertically), while the zero-th-order SL peak remains unaffected from these broadenings, see section 3.5.2. From the scans in Fig. 4.19 no difference between the zero-th-order SL peak and the satellite peaks is apparent. Therefore, interface roughness is assumed to be low. Also, no indication of mosaic spread
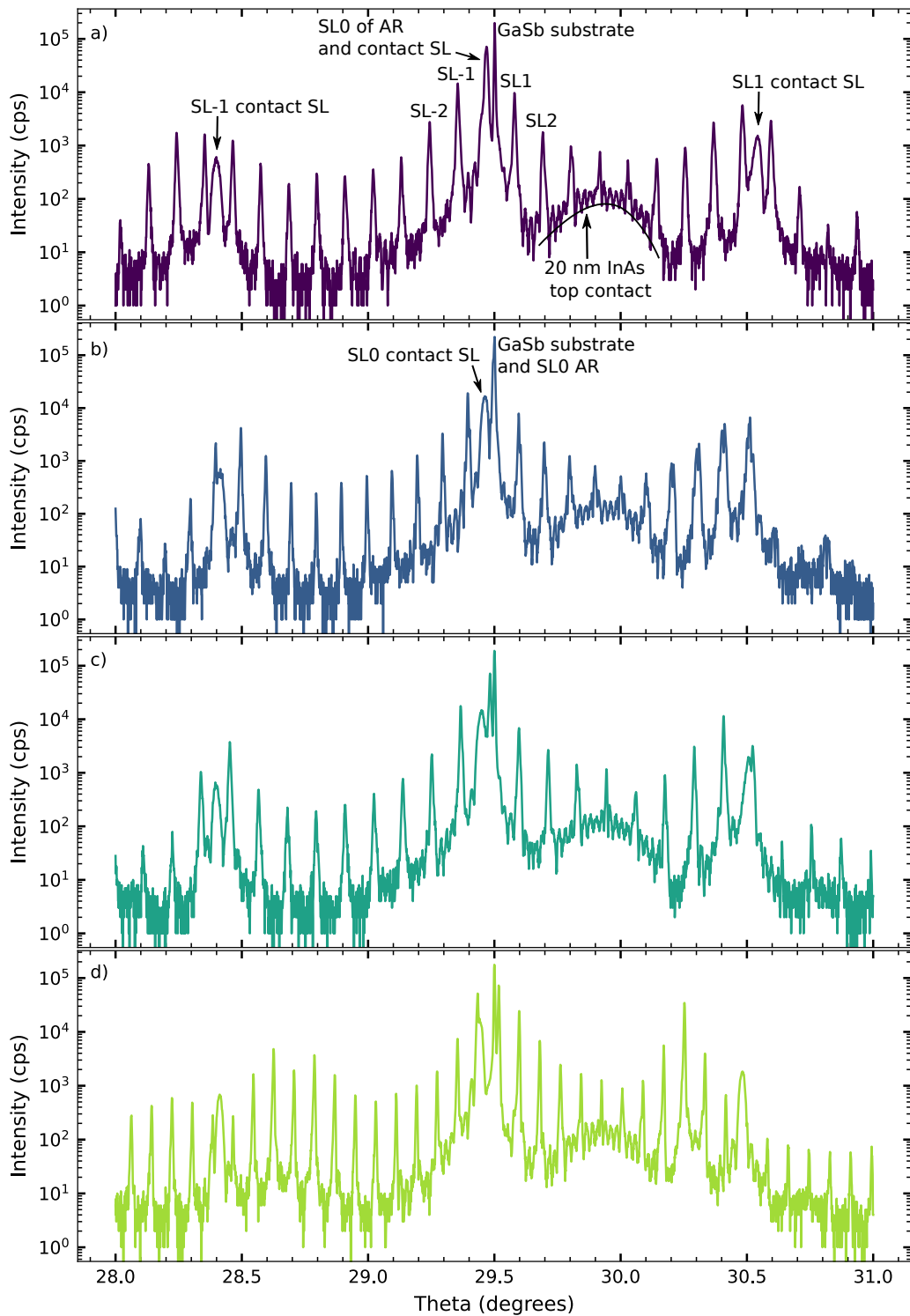
Figure 4.18: $(0\,0\,4)$ ω-2θ HR-XRD scans of the grown QCDs at a) $3.65\,\mu$m, b) $4.3\,\mu$m, c) 4.3b μm, and d) $5.5\,\mu$m. In a) and b) the peaks are labeled for clarity. SL0 is the 0th-order superlattice peak and the higher orders are labeled with progressing numbers. AR is the active region of the QCD.
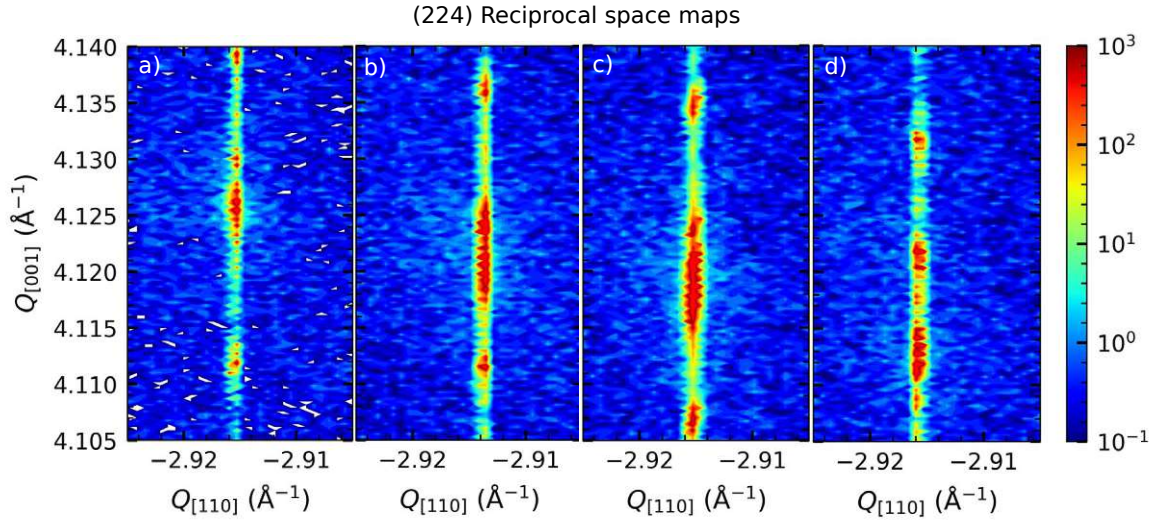
Figure 4.19: (2 2 4) reciprocal space maps of the grown QCDs at a) 3.65 μm, b) 4.3 μm, c) 4.3b μm, and d) 5.5 μm. All samples show straight vertical intensity contours, indicating fully strain-compensated structures. No interface roughness-, or growth fluctuations related broadening of the intensity maxima is apparent. Mosaic spread, which would result in a tilt of the intensity maxima is also not observed.

resulting in a tilt of the intensity maxima is observed. The performed scans each needed 15 h each, still, the resolution is limited because slices in reciprocal space were measured. The observed contour pattern is attributed to image processing, due to a not-perfect grid in the reciprocal space.

The strain balancing or the mismatch of the grown film to the substrate can be calculated from the mismatch of the zero-th-order SL-peak to the substrate peak.

	3.65 μm QCD	4.3 μm QCD	4.3b μm QCD	5.5 μm QCD
SL0 mismatch SL contact	0.0958 %	0.1068 %	0.1489 %	0.1958 %
SL0 mismatch active region	0.0958 %	not resolvable	0.0517 %	0.0509 %
FWHM grown SL contact/calculation (arcsec)	43.6/77.5	92.8/82.8	62.7/82.8	33.7/79.3
FWHM grown active region/calculation (arcsec)	25.1/20.3	22.1/19.1	22.5/19.1	20.1/17.0
RMS surface roughness (nm)	0.207	0.195	0.214	0.285

Table 4.2: HR-XRD and AFM results of the grown QCD designs. A comparison to the calculation of the structure is given. The RMS surface roughness is given of a 10×10 μm AFM scan.

Table 4.2 shows the mismatch of the contact SL and the active region zero-th-order peaks to the GaSb substrate for the grown QCDs. The mismatch was purposefully moved towards compressive strain (Sb-rich, the left side of the substrate, lower θ) rather than tensile strain (As-rich), because compressive strain leads to fewer defects than tensile strain. The contact SL calibrations, with a thickness of 400 nm showed, excellent strain balancing. The peak moved to Sb-rich (left, lower θ) conditions for the thicker structure in the final device.
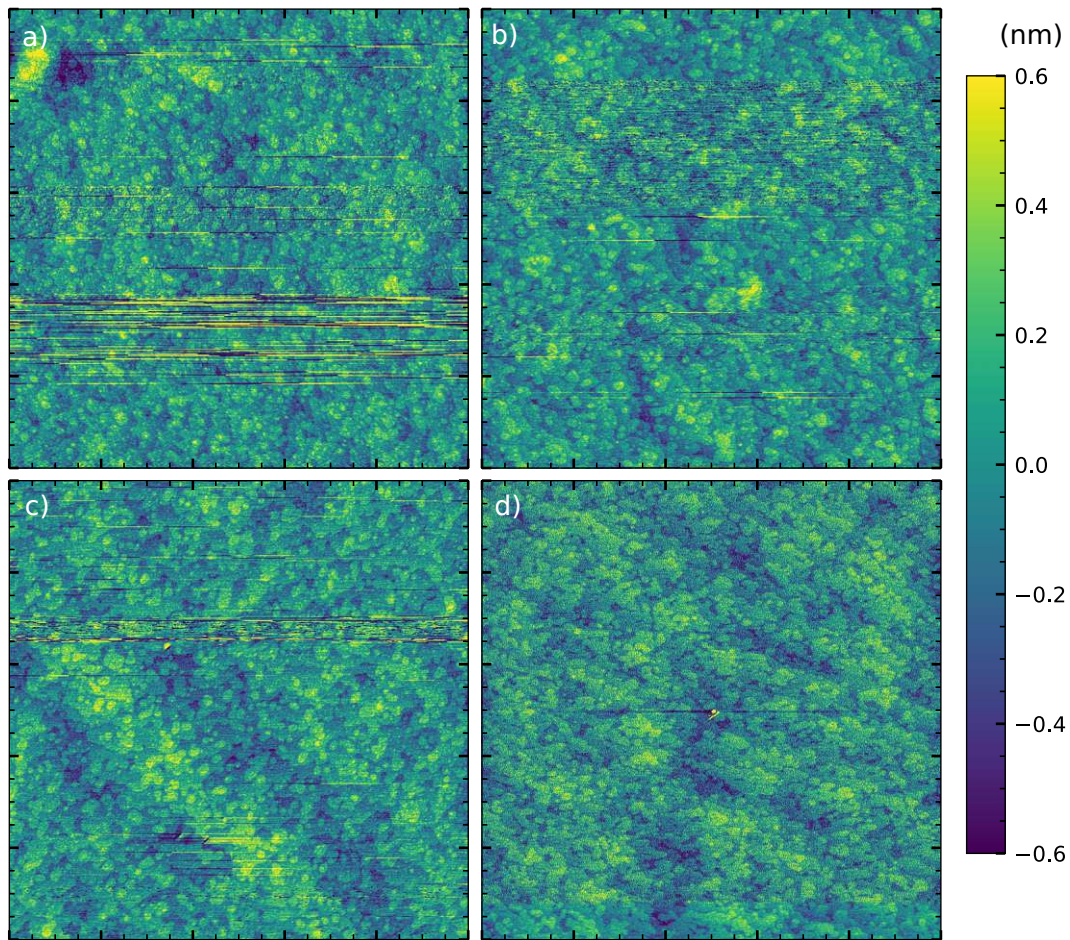
Figure 4.20: $10 \times 10\,\mu m$ AFM scans of the grown QCDs at a) $3.65\,\mu m$, b) $4.3\,\mu m$, c) $4.3b\,\mu m$, and d) $5.5\,\mu m$ on GaSb.

From the SL-peaks the FWHM are measured, see table 4.2. For comparison, the FWHM of the GaSb substrate peak in a $(0\,0\,4)$ HR-XRD-scan resulted in $20.7\,arcsec$. The sharp SL-peaks indicate, sharp interfaces, and low interface diffusion, which is difficult to achieve with two layers with alternating group V composite, due to the As-for-Sb exchange.

Fig. 4.20 shows the $10 \times 10\,\mu m$ AFM scans of the QCDs, in which step-flow growth is observed. The RMS surface roughness for the devices is given in table 4.2. There is no tilting between the mismatched layers, which is corroborated by the AFM measurements not having oriented surface steps, see Fig. 4.20.

4.4.3 Fabrication

The QCDs on GaSb were fabricated into a double-pass 45°-facet geometry, see section 2.5.3, for the optical characterization. Fig. 4.21 depicts a schematic of the
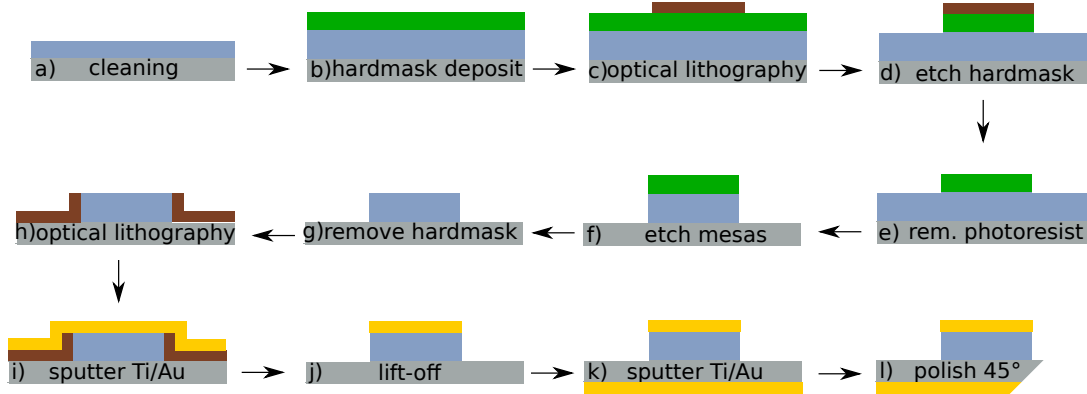
Figure 4.21: Sketches of the device scheme that depict each conducted fabrication step. The gray layer is the substrate. The blue layer is the active region. The Si_3N_4 hardmask/passivation is drawn in green. The photoresist is depicted in dark red and the Ti/Au contacts in yellow.

fabrication process, where a few steps overlap with the fabrication of the top-side illuminated QCD. For a detailed discussion of those steps refer to section 4.3.4. The objective of this fabrication process was to use time-proven device geometries. After a) the cleaning procedure, b) a Si_3N_4 hardmask was deposited with the PECVD and in the next step c) defined using optical lithography, where $150{\times}150\,\mu$m mesas were fabricated. The hardmask was dry-etched d) in an ICP-RIE chamber with a CHF_3 and O_2 process. e) the photoresist was removed, and f) the mesas were defined in the ICP-RIE chamber using a Cl/Ar- process. This process yielded the desired smooth, slightly positive sloped sidewalls. Multiple etch steps were needed, while the etch rate was controlled by a stylus profiler to etch to the desired depth. g) the hardmask was removed. Next, h) optical lithography was performed for the top contacts. Ti/Au was deposited i) using sputtering, and j) a lift-off was performed. The bottom contact was the backside of the substrate, for this k) Ti/Au was deposited in a separate sputtering step. Next, l), the wafer edge was polished into a 45°-facet.

4.4.4 Optical characterization and analysis of the results

The QCDs were optically characterized with an FTIR and a Globar source, as described in section 2.6. Because the GaSb substrate is transparent in the desired absorption range of the QCDs, the devices were illuminated under an angle of 45° through a polished bottom facet. This is the standard characterization technique for QCDs and quantum well infrared photodetectors (QWIPs), which allows the comparison of these QCDs to literature.

For each of the QCDs, 3–4 devices were measured in ambient conditions. Fig. 4.22 shows the absorption spectra of the measured QCDs. The reproducibility depends on
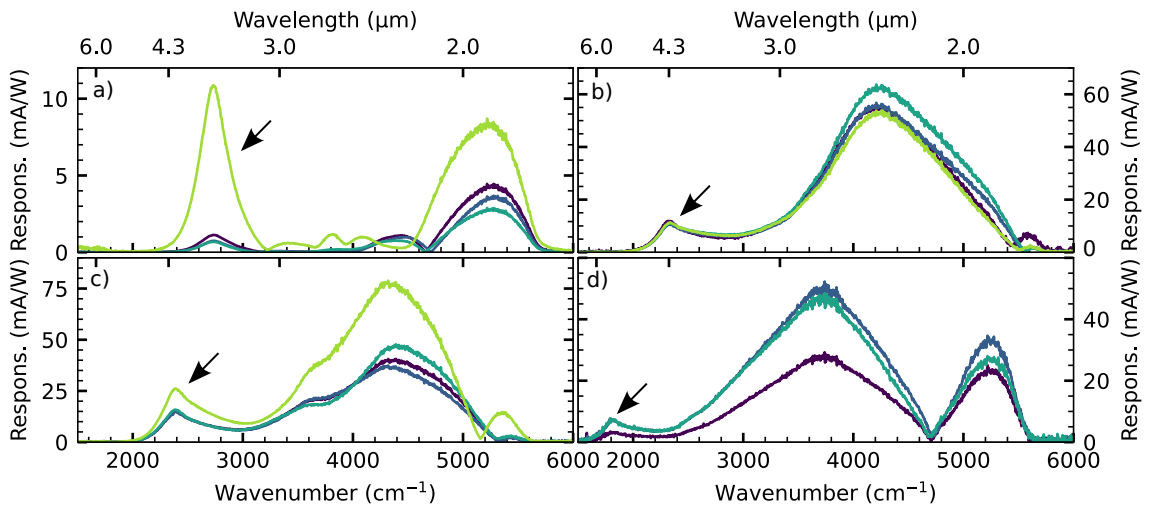
Figure 4.22: Responsivity measurements at ambient conditions of 3–5 mesas $150 \times 150\,\mu m$ in size for each device. The arrow marks the absorption corresponding to the designed QCD absorption. The broadband signal corresponds to interband absorptions. The spectra correspond to the following designs: a) $3.65\,\mu m$, b) $4.3\,\mu m$, c)$4.3b\,\mu m$, and d)$5.5\,\mu m$.

the facet quality over the length of the sample. The measured mesas were processed in a row. The mesas in Fig. 4.22 a) and c) with apparent responsivity deviations from the other mesas were closest to the sample corner. The peak room temperature responsivities and detectivities at the designed QCD absorption wavelengths, calculated with eq. 2.34 of the devices are $10.85\,mA/W$ and 1.17×10^8 Jones for the QCD at $3.65\,\mu m$, $12.5\,mA/W$ and 3.81×10^7 Jones for the QCD at $4.3\,\mu m$, $26.0\,mA/W$ and 1.41×10^8 Jones for the QCD at $4.3b\,\mu m$, and $8.3\,mA/W$ and 1.73×10^7 Jones for the QCD at $5.5\,\mu m$. The observed photoresponse is at the designed absorption wavelength for all QCDs and is marked with a black arrow, respectively. The higher energy signal is a broadband photoresponse due to interband absorption that cuts off at the GaSb substrate bandgap absorption.

Polarization-dependent measurements were conducted to gain insight into the nature of the signal at the designed QCD absorption wavelength, see Fig. 4.23. As discussed in section 2.2.2, intersubband transitions only allow absorption for the electric field component in the growth direction. Interband absorption also shows a polarization dependency, but the intensity difference between TE and TM light is not so prominent [129].

It is striking that the signal at the designed absorption wavelength is not vanishing for either polarization, although it is losing intensity with light polarized perpendicular to the growth direction. From the responsivity measurements with an unpolarized
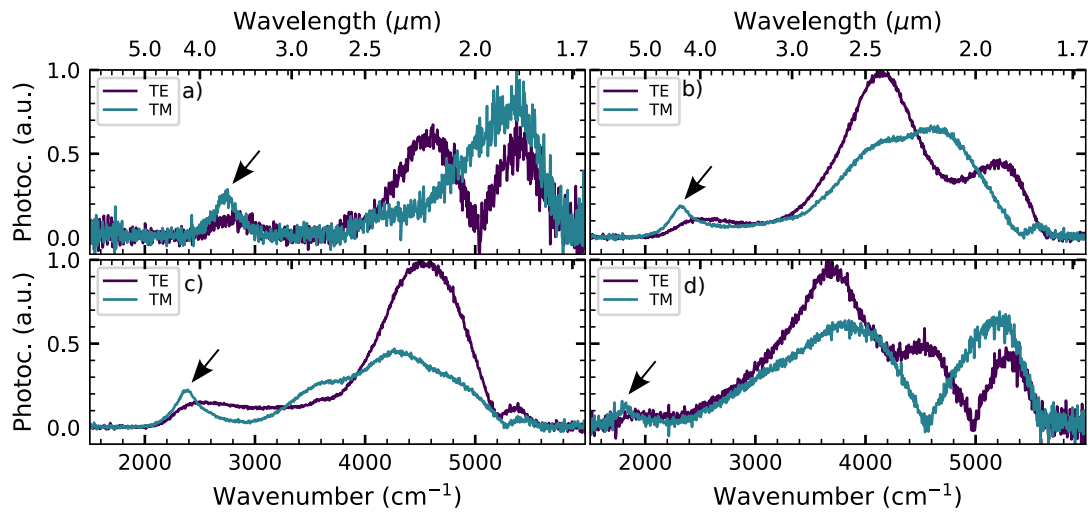
Figure 4.23: Polarization dependent photocurrent measurements for the designs: a) 3.65 µm, b) 4.3 µm, c)4.3b µm, and d)5.5 µm. It is apparent that the absorption attributed to the QCD signal does not completely disappear with the TE polarized light, but becomes lower in intensity and changes form. This indicates that the QCD signals are mixed with an interband absorption.

source, see Fig. 4.22 and the TM polarized spectra, the percentage of the intersubband QCD signal can be calculated. With this peak room temperature responsivity, purely attributed to the QCD intersubband transition is 8.02 mA/W for the QCD at 3.65 µm, 8.75 mA/W for the QCD at 4.3 µm, 16.12 mA/W for the QCD at 4.3b µm, and 5.89 mA/W for the QCD at 5.5 µm.

Additionally, it is striking, that the shape of the entire spectrum changes depending on the polarization. This is attributed to the competition between the QCD intersubband and the interband absorptions. The exact mechanisms are a subject of further research.

In the following, it is attempted to explain the obtained spectra with the help of the band structures, see Fig 4.24. As noted in section 4.3.1, a type-II band structure alignment is observed for the InAs/AlSb material system, where the band gap between the AlSb valence band and the InAs conduction band is 0.14 eV, which corresponds to a low energy separation, corresponding to the mid-infrared spectral region. Interestingly, the cut-on of the interband signal, marked with a black arrow in Fig. 4.24 a) corresponds to the energy separation of the lowest ground state in the InAs conduction band to the AlSb valence band, see also the black arrow in Fig. 4.24 b). It is expected that interband absorption occurs over the entire extractor of the QCD extractor, see grey arrows in Fig. 4.24 b). The shoulder in the interband signal, marked with a green arrow, corresponds to the transition involving the lowest
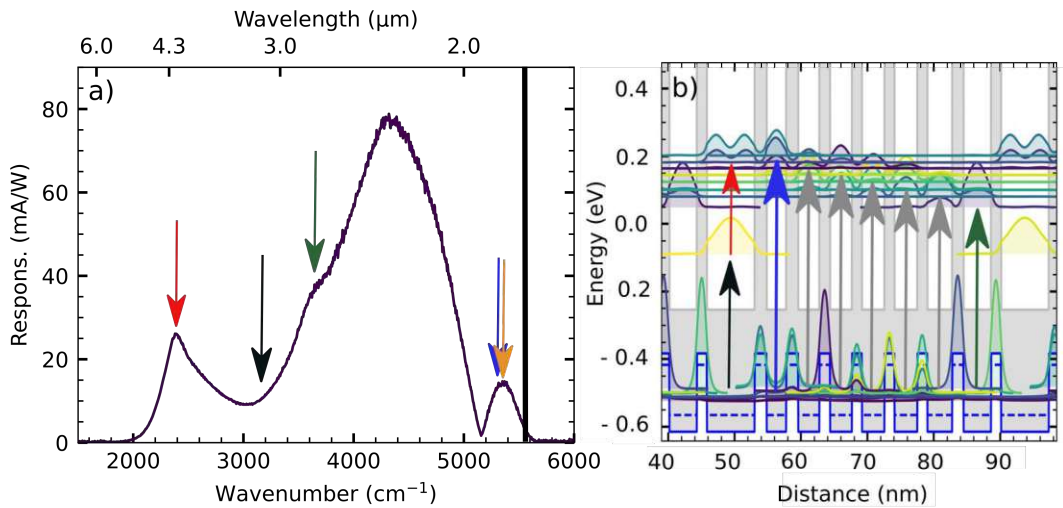
Figure 4.24: The absorption spectrum of the QCD designs is explained with the help of the design at 4.3b µm a). It is compared to its band structure design b). The arrows indicate the corresponding absorption energies from the spectrum in the band structure design. The cut-on (black arrow) of the pure interband signal occurs at the energy corresponding to the energy separation of the AlSb valence band states to the InAs ground state in the widest well, being the smallest energy separation for an interband transition. The green and blue arrows correspond to the lowest and highest transition in the extractor. The orange arrow marks possible transition energies due to the contact superlattice. The black vertical line marks the cut-off due to the GaSb substrate absorption.
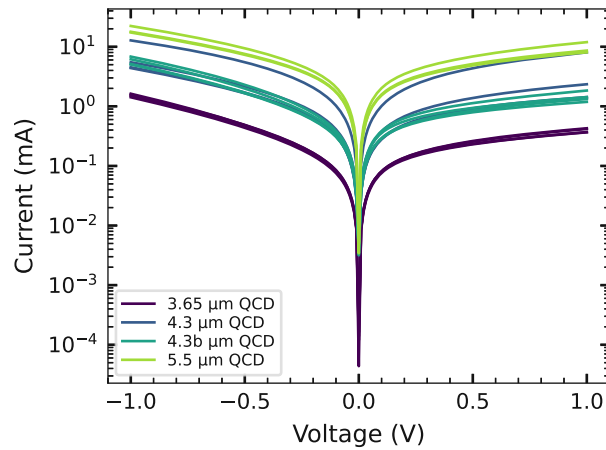
Figure 4.25: I-V measurements in illuminated conditions of the grown QCD designs on GaSb: 3.65 µm, 4.3 µm, 4.3b µm, and 5.5 µm.

extractor ground state. The smaller peak in the spectrum, which is marked with a blue and orange arrow, corresponds to a transition involving the highest extractor state but also to the separation energy of the ground states in the contact superlattice to the AlSb valence band states. Due to the formed miniband in the AlSb valence

band, the transition energies are expected to broaden.

The observed cut-off in the spectra is attributed to the onset of the GaSb substrate absorption, marked by a black vertical line in Fig. 4.24, as well as the already low intensity of the Globar in this region. It is important to note that the used ZnSe lenses are optimized for the mid-infrared spectral region.

Fig. 4.25 depicts the I-V characteristics measured in illuminated conditions of the detectors. The difference in current corresponds to the difference in the width of the doped optical well.

Engineering the absorption spectrum

By knowing the origin of the broadband interband signal, engineering the absorption through the modification of the layer thicknesses is possible. For example, making the barriers around the optical transition well thinner moves the valence band states in the AlSb layers down, and thus the cut-on of the broadband interband signal to higher energies. For the QCD design at 4.3b µm, the barrier before the optical well was thinned from 1.8 nm to 1.5 nm, which is a minor change, due to the already thin barriers and the increased splitting of the states in the wells, but it should break up the valence band miniband a little bit. The resulting absorption spectrum is plotted in Fig. 4.24. When compared to the original structure, only the interband signal changed in width. At this time it is not clear if the change in barrier width is the only source of the change in the spectrum, as this is a topic of further research.

Bias dependent measurements

With the origin of the broadband interband signal in mind, it was found of interest to perform bias-dependent measurements, because no preferred direction of carrier flow in the valence band miniband in the band structures is visible.

Measurements with applied biases in the range of -0.03– +0.03 V with 0.01 V steps were performed, see Fig. 4.26. While the location of the signal at the designed QCD absorption wavelength does not change, there is a strong dependency on the bias for the broadband interband signal spectrum. The intensity increases for positive biases (also the QCD signal) and the absorption spectrum changes for negative biases. In Fig. 4.26 it is observed that by applying the correct negative bias, the broadband interband signal can be moved away from the QCD signal, where positive biases do not change the shape of the spectrum significantly but rather increase the intensity.
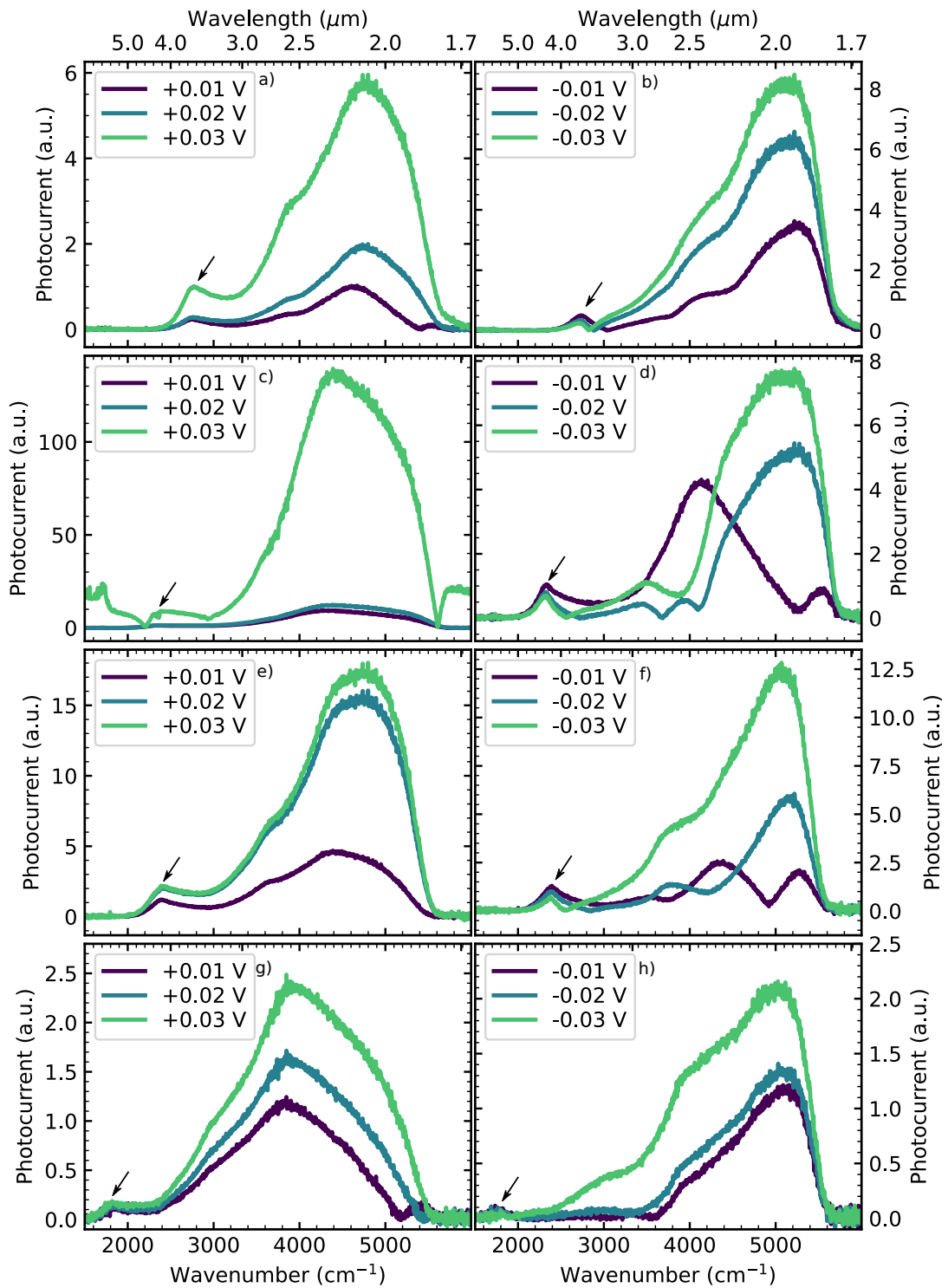
Figure 4.26: Bias-dependent photocurrent measurements at ambient conditions. Measurements of the designs at positive: a), c), e), and g) and negative voltages: b), d), f), and h) of the QCD designs at: a), b) 3.65 μm, c), d) 4.3 μm, e), f) 4.3b μm, and g), h) 5.5 μm. It is apparent that while with positive voltages the intensity of the spectrum increases, with negative voltages the interband spectrum changes and can be moved away from the QCD signal.

Comparison to InAs/AlAs$_{0.16}$Sb$_{0.84}$ QCDs grown on InAs

Earlier in this chapter an InAs/AlAs$_{0.16}$Sb$_{0.84}$ QCD at 2.7 µm was discussed. Fig. 4.9 b) shows the full absorption spectrum, revealing that this QCD also exhibits a broadband interband absorption. In contrast to the QCDs on GaSb, the absorption at 2.7 µm purely corresponds to an intersubband signal, see Fig. 4.11. Similar to the QCDs grown on GaSb, the cut-on of the broadband interband signal corresponds to the lowest interband transition in the band structure and ends with the highest transition in the extractor.

In earlier work, an InAs/AlAs$_{0.16}$Sb$_{0.84}$ QCD on an InAs substrate was designed and characterized [80]. Although it detects at a similar wavelength as the QCDs designed on GaSb in this work, namely 4.84 µm, the signal corresponds only to an intersubband transition without an interband signal. In the case of this QCD, the broadband intersubband absorption was partly blocked by the InAs substrate but is still perceptible in unpublished measurements [128].

The common factor of those two QCDs grown on InAs (2.7 µm and 4.84 µm) is that they are designed with thicker barriers. This reduces the extraction efficiency, as discussed in section 4.4.1, but also increases the carrier confinement, and decreases the level splitting, thus producing less broadening in the absorption spectrum. This could be a possible reason why the interband absorption is more separated from the QCD signal.

Anomalous temperature effect in low-doped weakly-coupled superlattices

The focus of this chapter is to discuss an anomalous temperature effect occurring in superlattices similarly low-doped as THz quantum cascade lasers (QCLs) and discuss what these results mean for the contact layer design of THz QCLs. Superlattices were one of the first heterostructures to be studied after the development of MBEs in the 1970s [130]. Theoreticians predicted interesting properties, such as Bloch oscillations [131] and Wannier Stark ladders [44]. Initial efforts were dedicated to the experimental observation of these theoretical predictions. Soon enough, superlattices were divided into weakly- and strongly-coupled, based on if their wavefunctions only extend to the neighboring well or over multiple wells. This chapter concentrates on the former. A thorough review of the properties of weakly and strongly coupled superlattices can be found in Ref. [47]. The results presented in this chapter are mostly based on the manuscript submitted for publication [132].

5.1 Motivation

Recent work on 3-well THz QCLs (see section 2.13) showed that an increase in the energy separation of the ground and first excited state in the extractor well can enhance the temperature performance, while up to that point, the longitudinal optical (LO)-phonon energy of the well material (for GaAs: 36 meV) was utilized for fast transitions [133]. With increased energy separation thermal backfilling is reduced, while the depopulation of the lower laser state is still sufficient to generate population

inversion [134–136]. Based on the results of an optimized structure published in [134] that operated in a thermoelectric cooler setup [137], because it was lasing up to 196 K, a 3-well THz QCL with an energy separation in the extractor well of 42 meV was grown, see Fig. 5.1 b) for the band structure. This QCL had a rather low sheet doping of 1.4×10^{10} cm^{-2} compared to conventional THz QCLs ($\approx 3 \times 10^{10}$ cm^{-2}). In Fig. 5.1 the temperature-dependent threshold current density J_{th} is plotted over the temperature. Typically the temperature dependency of J_{th} follows an exponential increase [14], which can be fitted with the equation:

$$J_{\text{th}}(T) = J_0 \exp(T/T_0) \tag{5.1}$$

Where J_0 is the current density at T_0, and T_0 the characteristic temperature, which is extracted from the fit. In Fig. 5.1 a) on the other hand J_{th} shows an anomalous decrease between 80–100 K.

A known effect that leads to a 1/T reduction of conductivity with increasing temperature is thermal saturation [48, 138]. This effect occurs for low doping when the miniband width Δ of the superlattice is $\Delta < k_B T$. The theory is described by the Boltzmann transport equation and holds for single bands, which is not the case for the THz QCL or the superlattice structures studied in the following. A reduction of current density with increasing temperature was also reported in [139, 140].

In the following, the anomalous temperature effect, observed for the THz QCL is further investigated with various weakly coupled superlattice structures. These structures utilize the same carrier transport mechanism as THz QCLs, namely sequential resonant tunneling. Performing this study with superlattice structures has two major benefits: Since superlattice structures have been investigated since the 1970s a vast knowledge of their properties exists in literature. Second, due to their easier structure, they are easier to interpret. With these superlattices, it can be investigated if this anomalous decrease of J_{th} observed for some THz QCLs is of transport-dependent nature or is resulting from defects or impurities. The goal of this study is a further design improvement of THz QCLs due to a deeper understanding of their carrier transport. To be able to compare the grown superlattice structures with THz QCLs, the superlattices have contact layers identical to conventional THz QCLs, and the same fabrication techniques for the finished devices were used (eg. double-metal (DM) contacts). Most importantly, the superlattices were doped in the same order of magnitude as conventional THz QCLs, for which the doping is in the 3–5×10^{10} cm^{-2}. Although superlattices were extensively studied, there is a lack of publications for similarly low-doped superlattices as THz QCLs.
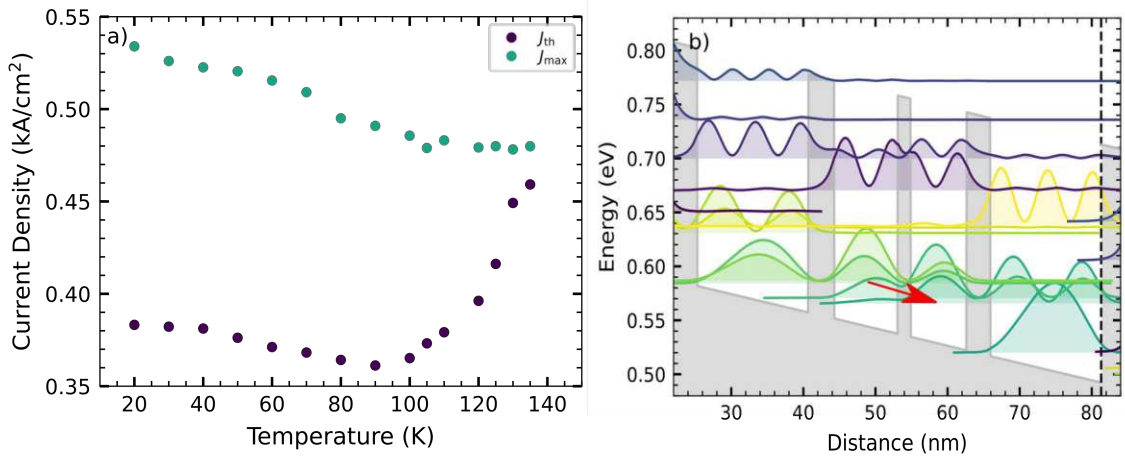
Figure 5.1: a) The threshold current density J_{th} and maximum current density J_{max} of a three well THz QCL fabricated with DM Au-Au contacts are plotted versus the temperature. It is apparent that with an increasing temperature J_{th} first decreases before it shows the expected exponential increase. The dynamic range of the laser $J_{\text{max}} - J_{\text{th}}$ at each temperature of the THz QCL can be calculated. Figure adapted from [132]. b) The band structure of the three-well THz QCL is shown. The red arrow indicates the optical active wells.

5.2 Grown structures and experimental method

Over the period of this Ph.D. three batches (B1, B2, B3) of weakly-coupled $\text{Al}_{0.24}\text{Ga}_{0.76}\text{As}/\text{GaAs}$ superlattice structures were grown by molecular beam epitaxy (MBE), spread over three growth campaigns, see table 5.1 for a detailed summary.

Sample	ΔE (meV)	Well (nm) GaAs	Si:GaAs	GaAs	AlGaAs (nm)	Doping (cm^{-3})	Si:GaAs Top/Bottom Contact (nm) & Doping (cm^{-3})	Contact	Anomalous Temp. Effect
B1S1	32	4.0	5.0	10.35	4.2	2×10^{16}	100 / 100 & 5×10^{18}	Ti/Au DM	no
B1S2	36	3.5	5.0	9.5	4.5	2×10^{16}	100 / 100 & 5×10^{18}	Ti/Au DM	yes
B1S3	40	3.0	5.0	8.85	4.8	2×10^{16}	100 / 100 & 5×10^{18}	Ti/Au DM	yes
B1S4	44	2.5	5.0	8.35	5.05	2×10^{16}	100 /100 & 5×10^{18}	Ti/Au DM	yes
B1S5	48	2.0	5.0	8.0	5.25	2×10^{16}	100 / 100 & 5×10^{18}	Ti/Au DM	yes
B2S1	44	2.5	5.0	8.35	5.05	2×10^{16}	100 / 250 & 5×10^{18}	Ge/Au/Ni/Au	yes
B2S2	44	2.5	5.0	8.35	3.5	2×10^{16}	100 / 250 & 5×10^{18}	Ge/Au/Ni/Au	no
B2S3	44	2.5	5.0	8.35	5.05	4×10^{16}	100 / 250 & 5×10^{18}	Ge/Au/Ni/Au	no
B2S4	44	2.5	5.0	8.35	4.3	2×10^{16}	100 / 250 & 5×10^{18}	Ge/Au/Ni/Au	yes
B3S1	36	3.5	5.0	9.5	4.5	2×10^{16}	100 / 250 & 5×10^{18}	Ti/Au	no
B3S2	36	3.5	5.0	9.5	4.5 (35% Al)	2×10^{16}	100 / 250 & 5×10^{18}	Ti/Au	yes
B3S3	36	2.0	5.0	11.0	4.5	2×10^{16}	100 / 250 & 5×10^{18}	Ti/Au	no
B3S4	36	5.0	5.0	8.0	4.5	2×10^{16}	100 / 250 & 5×10^{18}	Ti/Au	no
B3S5	36	3.5	5.0	9.5	4.5	1×10^{16}	100 / 250 & 5×10^{18}	Ti/Au	yes
B3S6	44	2.5	5.0	8.35	5.05	2×10^{16}	100 / 250 & 5×10^{18}	Ti/Au	yes
B3S6b	44	2.5	5.0	8.35	5.05	2×10^{16}	100 / 250 & 5×10^{18}	Ge/Au/Ni/Au	yes
B3S7	44	2.5	5.0	8.35	5.05	2×10^{16}	100, 50 / 50, 100 & 5×10^{18}, 5×10^{17}	Ti/Au	no

Table 5.1: Detailed summary of the grown superlattice structures and the grown/processed contacts. For each structure, 45 periods of the well and barrier were grown. B denotes batch and MBE growth campaign number. The well widths are listed from left to right in the growth direction. The table is adapted from the supplemental material of [132].
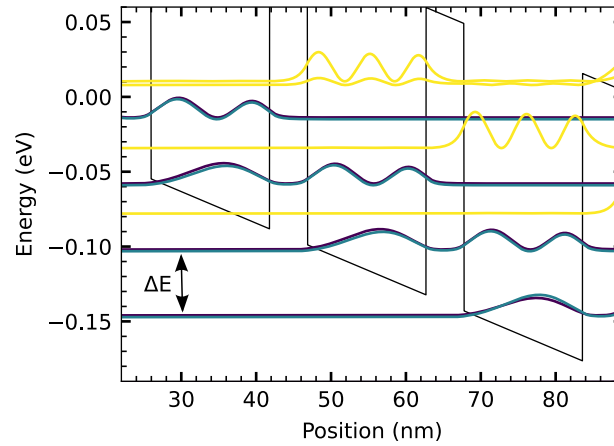
Figure 5.2: Three periods of a typical band structure of a superlattice. ΔE is the energy separation between the ground and the first excited state at the alignment electrical field. Figure adapted from [132].

One period of the superlattices consists of one well and one barrier. A total of 45 periods were grown between highly doped contact layers for all grown samples. The used GaAs substrate (semi-insulating or highly doped), the thickness and doping of the contact layers, and the fabricated contacts (Au-Au DM: Schottky barrier, or Ge/Au/Ni/Au: ohmic contact) varied per batch. Therefore, a reference sample of a previous batch was regrown as a part of each new batch. Within a batch, the well and barrier thicknesses, the doping concentration, the dopant position, and the grown contact layers were additionally varied. Like this, a thorough study could be conducted. Fig.5.2 depicts three periods of a typical band structure of the superlattice samples, ΔE is the energy separation of ground and first excited state at the alignment electrical field. A 5 nm thick layer in each quantum well is doped. All superlattice structures were fabricated into $150 \times 150\,\mu m$ mesas by reactive ion etching using SiCH$_4$ yielding vertical, slightly positively sloped sidewalls.

In the first batch B1 five structures were grown, where the GaAs well thickness was varied. The variation of the well thickness modifies the energy difference between the ground and the first excited electron state in the quantum well. The energy difference ΔE between the first two energy levels at the alignment electrical field is varied between 32–48 meV. This range includes the GaAs LO phonon energy of 36 meV. The barrier thicknesses were varied to match an energy splitting of 1.1 meV for states in neighboring wells at the alignment electrical field. These structures were grown to study the effect of level separation on the current transport. The superlattices of B1 were grown between 100 nm-thick GaAs contact layers doped $5 \times 10^{18}\,cm^{-3}$ ($5 \times 10^{13}\,cm^{-2}$) on semi-insulating GaAs substrates (carrier concen-

tration: 6.5×10^6 cm^{-3}). The grown devices were fabricated in the double metal configuration with Ti/Au contacts (top: 10/400 nm bottom: 10/1800 nm) that form a Schottky barrier with GaAs.

For the second batch (B2) four structures were grown. This time the barrier width and the doping were varied, while the well width and therefore ΔE was kept a constant ΔE= 44 meV. This was done to study the current transport in terms of tunneling efficiency. The structures were grown between 5×10^{18} cm^{-3} doped GaAs contact layers (top: 100 nm, bottom: 250 nm) on 2.8×10^{18} cm^{-3} n-plus GaAs substrates. For B2 ohmic contacts were fabricated with evaporated Ge/Au/Ni/Au (15/30/14/330 nm), which were then rapidly thermally annealed to 440 °C for 30 s. The bottom contact was fabricated on the backside of the substrate.

For the third batch (B3) five structures were grown, ΔE was either 36 or 44 meV. This time the doping, the dopant position, and the contact layers were varied. The doping positions was varied to gain insight of possible effects due to Si diffusion into the barriers. The contact layers were varied to gain insight to their influence on the current transport of the superlattice structure. The grown devices were fabricated with Ti/Au contacts (10/360 nm), with the bottom contact being on the backside of the 2.8×10^{18} cm^{-3} n-plus GaAs substrate.

To characterize the transport behavior of the grown superlattices, temperature-dependent current-voltage (I-V) characteristics in dark and in some cases also in light conditions were recorded. For this, the temperature was varied in 5 K steps between 5–140 K and up to room temperature in 20 K steps. Four-point measurements were taken with a Keithley Model 2450 SourceMeter source meter unit (SMU) and a Keithley Model DAQ6510 data acquisition system in a closed-cycle He cryostat. The temperature was controlled with a LakeShore 335 temperature controller.

5.3 Results

In the following, the observed effects of the temperature-dependent I-V measurements are discussed.

5.3.1 Plateau formation and negative differential resistance segments

Fig.5.3 shows a typical I-V measurement of a superlattice structure, which was measured to a current compliance of $\pm$ 250 mA at a voltage of approx. $\pm$5 V, depending on the temperature.
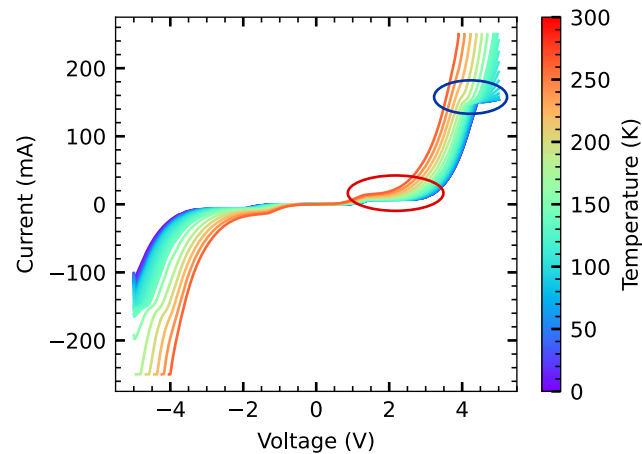
Figure 5.3: Three periods of a typical band structure of a superlattice. ΔE is the energy separation between the ground and the first excited state at the alignment electrical field. Figure adapted from [132].

The I-V curve is symmetric for positive and negative voltages. It exhibits plateaus, which are encircled for the positive current direction. Additionally, equally spaced negative differential resistance (NDR) segments occur in the superlattice samples of B1 for the structures with $\Delta E \geq 36\,\text{meV}$, see Fig.5.4.

This effect is explained by the formation of a high and low electric field domain in [45, 46], which are separated by a charge accumulation layer [141, 142]. It can be understood as follows: When applying an electric field to a superlattice by applying a bias, the structure does not homogeneously adapt to the electric field but a low and high electric field domain forms, which moves along the superlattice when the electric field increases. This leads to a sequential alignment of the ground state of one well to the first excited state of its neighboring well, as the domain boundary, being a charge accumulation layer, moves along the superlattice structure.

From this effect, several conclusions can be made. Due to the sequential alignment of the wells one after each other and the charge accumulation layer at the domain boundary, the number of NDR segments in the plateau approximately corresponds to the number of grown periods. The separation of the ground state to the first excited state at the given voltage can be calculated from the voltage distance of the NDR segments to one another. This separation additionally gives the electric field change at the domain boundary, and from that the charge density at the domain boundary can be calculated using the Poisson equation [142]. The fluctuations in doping can be calculated from the variation in amplitude of the NDR oscillations [142].

The second plateau at higher current and voltage observed in Fig.5.3 is occurring due to the sequential alignment of the first excited state to the second excited state
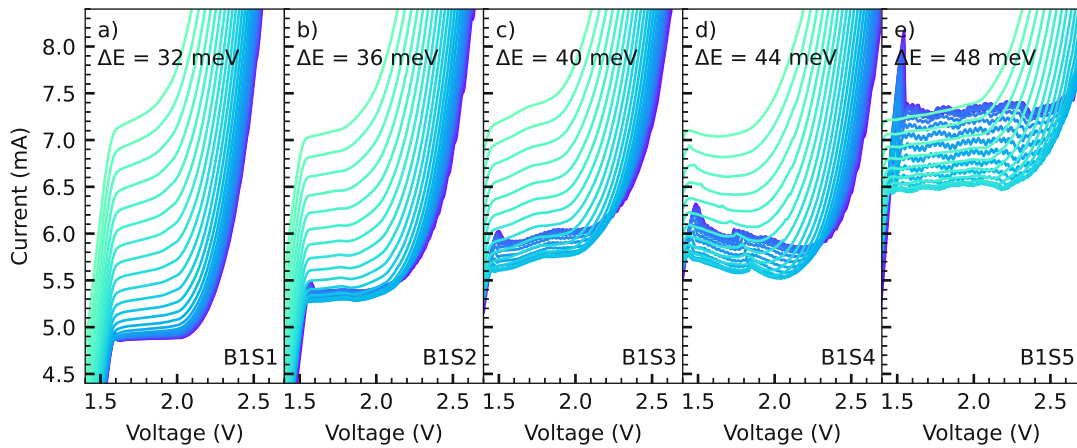
Figure 5.4: Comparison of samples of batch 1 with different ΔE. Zoom-in on the first plateau for the structures B1S1, B1S2, B1S3, B1S4, and B1S5. Equally spaced NDR segments are visible, as well as an inflection point in the average current in the plateau over the temperature. Batch 1 was processed in the double metal configuration and designed with increasing ΔE (ΔE= 32–48 meV). The I-Vs are measured in temperature steps of 5 K from 5–140 K. For the color scale please refer to Fig.5.3. Data from [132].

in two neighboring quantum wells.

Therefore, the voltage range between the two plateaus corresponds to the dynamic range of the designed superlattice structure, which marks the voltage range between the alignment to the misalignment of the first wells.

5.3.2 Observation of an anomalous temperature effect with increasing ΔE

An observation made in the initial batch B1 is that the structures with $\Delta E \geq 36$ meV, like the THz QCL in the motivation, show the unexpected temperature-dependent behavior of the current-flow through the superlattice, see Fig.5.4. The current measured at the first plateau initially decreases with increasing temperature starting from 5 K until it reaches a minimum between 75–110 K depending on the structure before it increases again with elevating temperature. It is also striking that the temperature where the minimum is reached increases with increasing ΔE.

Based on these observations the anomalous temperature effect was further investigated in this work with the help of the superlattice structures grown in the batches B2 and B3.
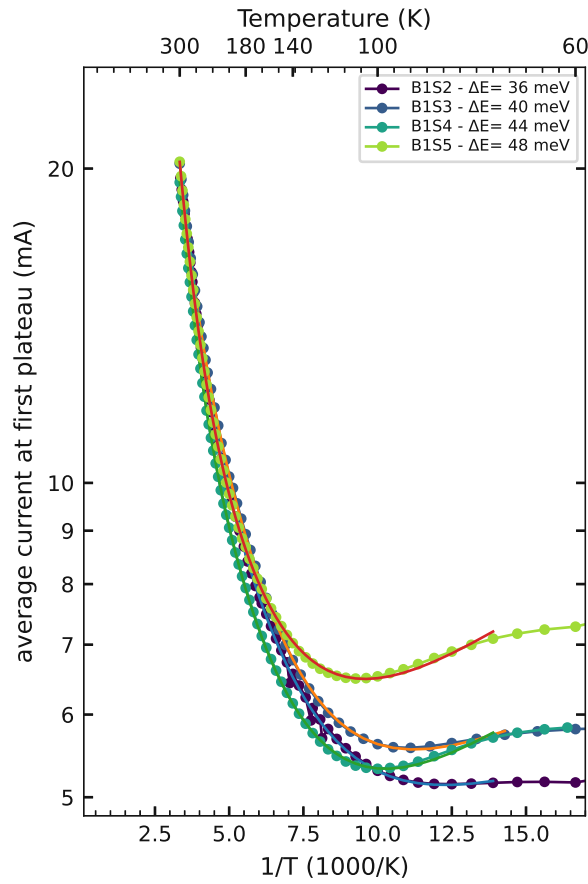
Figure 5.5: Arrhenius plot of the average current at the first plateau of the samples of B1 plotted over the temperature. The solid lines correspond to the fits, where each fit was performed with three energies by adding three lines.

5.3.3 Defect or impurity relation and I-V measurements bright conditions

The initial effort was dedicated to finding out if the observation was defect or impurity related because traps and impurities usually have a temperature-dependent activation energy [94].

For this reason, Arrhenius plots were made, see Fig.5.5. The curves for each sample can be fitted with three lines, each corresponding to different activation energies, see table 5.2, attributed to the following:

E_a matches closely to the energy from the ground state to the conduction band offset (CBO) edge of $GaAs/Al_{0.24}Ga_{0.76}As$ minus the energy of the first excited state of approx. 174 meV. The second activation energy E_b matches the LO-phonon energy of GaAs being 36 meV. The third activation energy E_c is negative and it is attributed to the activation energy causing the anomalous temperature effect. This would

Sample	ΔE (meV)	E_a (meV)	E_b (meV)	E_c (meV)
B1S2	36	159.78	38.02	-1.64
B1S3	40	172.35	39.50	-2.46
B1S4	44	156.95	38.64	-3.69
B1S5	48	146.01	39.64	-3.64

Table 5.2: The activation energies corresponding to the fits of Fig.5.5 are given for every sample.
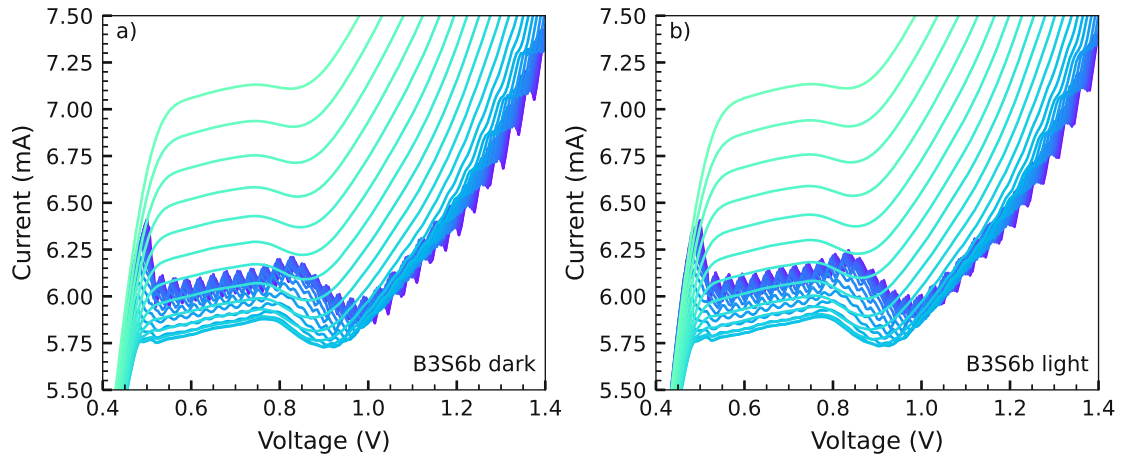
Figure 5.6: a) Temperature dependent I-V measurement of B3S4b in dark conditions processed with ohmic contacts. b) Measurement performed in bright conditions. During the I-V measurements, a red LED was turned on. It is apparent that there is almost no visible change between the two measurements.

correspond to a shallow acceptor, but in the literature search, no fitting energies were found. Common energies of GaAs traps can be found in [94]. As for the barriers, the AlGaAs barriers with an Al fraction of $0.2 \geq x \geq 0.4$ are known to generate donor-complex (DX) centers, which form as a result of Si dopant diffusion from the GaAs wells to the AlGaAs [143], see section 3.3.2. DX centers have an activation energy of around 135 meV and are frozen out below 150 K [94].

Any form of trap could also be activated with energy in the form of light, therefore I-V measurements in bright conditions with a red LED were performed on B3S4b with ohmic contacts, see Fig.5.6. If the anomalous temperature effect was trap or impurity related one would expect a decrease of the temperature where the lowest current is occurring or a complete disappearance of the effect, which is not the case. Instead, there is almost no difference visible between the dark and light measurements. At 10 K the light measurement has a current increase of 0.8% in the first plateau compared to the dark measurement.
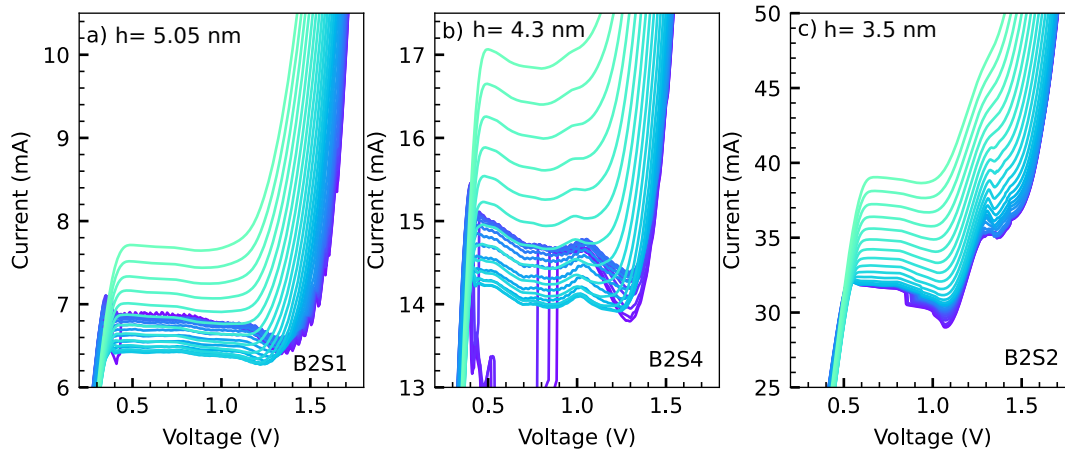
Figure 5.7: Comparison of samples of batch 2 with different barrier widths. Zoom-in on the first plateau for the structures B2S1, B2S3, and B2S4. B2S3 and B2S4 were grown with declining barrier thicknesses of 4.3 nm and 3.5 nm respectively. The I-Vs are measured in temperature steps of 5 K from 5–140 K. For the color scale please refer to Fig.5.3. Data partly from [132].

5.3.4 Effects of barrier thicknesses and barrier height

In the samples of B2, the barrier thickness was varied, additionally, the samples were processed with ohmic contacts in contrast to the double-metal Ti-Au Schottky contacts of B1, see section 5.2, to investigate the influence of the fabricated contacts. Fig.5.7 a) depicts a regrowth of B1S4 as a reference. Fig.5.7 b) and c) show the same design with a decreased barrier thickness of 4.3 nm (B2S4) and 3.5 nm (B2S2). B2S4 is moved to higher currents compared to B2S1, but the plateau shape and the temperature inflection are comparable. This changes for B2S2 where the temperature inflection effect is completely gone. Consistently with the even thinner barriers the plateau moves to even higher currents, the plateau is deformed, and the second plateau disappears in the I-V. This indicates less carrier confinement in the structure, but the occurrence of the plateau indicates that a high and low electric field domain still exists [141].

Note, that also in B1 the barrier thicknesses are varying from 4.2 nm for B1S1 with $\Delta E= 32$ meV to 5.25 nm for B1S5 with $\Delta E= 48$ meV. This is done to match the energy splitting to 1.1 meV for all structures of B1. Because B2S2 with 4.3 nm barriers shows the same anomalous temperature effect as B2S1 with a barrier width of 5.05 nm, we believe that the variation in barrier width of the samples of B1 can be neglected.

Fig.5.8 shows the temperature-dependent I-V measurement of B3S6 with $\Delta E= 36$ meV and 35% Al in the barriers instead of 24% Al, while the well and barrier
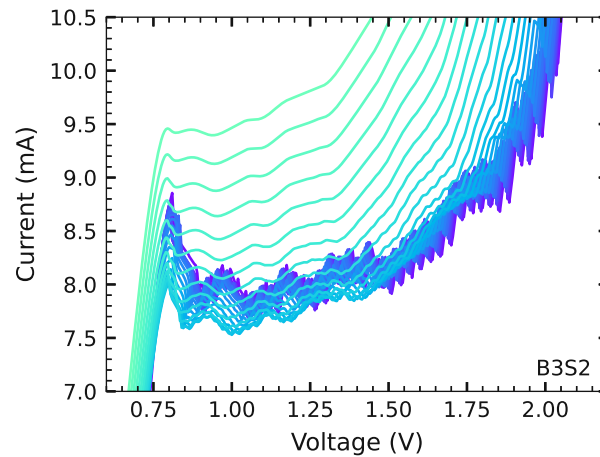
Figure 5.8: Zoom-in on the first plateau for the structure B3S2. It is a regrowth of B3S1 with 35 % Al instead of 24 % Al. The I-Vs are measured in temperature steps of 5 K from 5–140 K. For the color scale please refer to Fig. 5.3.

thicknesses stayed the same. In comparison to Fig. 5.4 b) the anomalous temperature effect increased.

5.3.5 Effects of the dopant position inside the well

In batch B3 the dopant position inside the well was varied, while the thickness of the well and barrier material stayed constant. This was done to investigate effects from possible dopant diffusion into the AlGaAs barriers that then could generate DX centers, as discussed in subsection 5.3.3.

Again, a reference regrowth of B1S2 was grown (B3S1) this time with Ti-Au fabricated contacts, where the bottom contact is at the back side of the n+ doped GaAs substrate. Note, that B3S1 does not exhibit an anomalous temperature effect, this is in contrast to its reference B1S2 where the anomalous temperature effect just starts to emerge. This can be attributed to slight growth deviations or the difference in growth campaigns and is the reason why the reference structures are grown. Then for B3S3, the dopant position was moved closer to the left barrier (in growth direction - from 3.5 nm to 2.0 nm away). For B3S4 the dopant position was moved further away from the left barrier (in growth direction - from 3.5 nm to 5 nm away). The temperature-dependent I-V measurements are plotted in Fig. 5.9. It is apparent that when moving the dopant position to the left the initial peak increases in amplitude, while it decreases when the dopant position is moved to the right. However, there is no influence on the anomalous temperature effect and also no on the plateau formation.

Note, that the dopant position also varies for the samples of B1, see Fig. 5.4. With
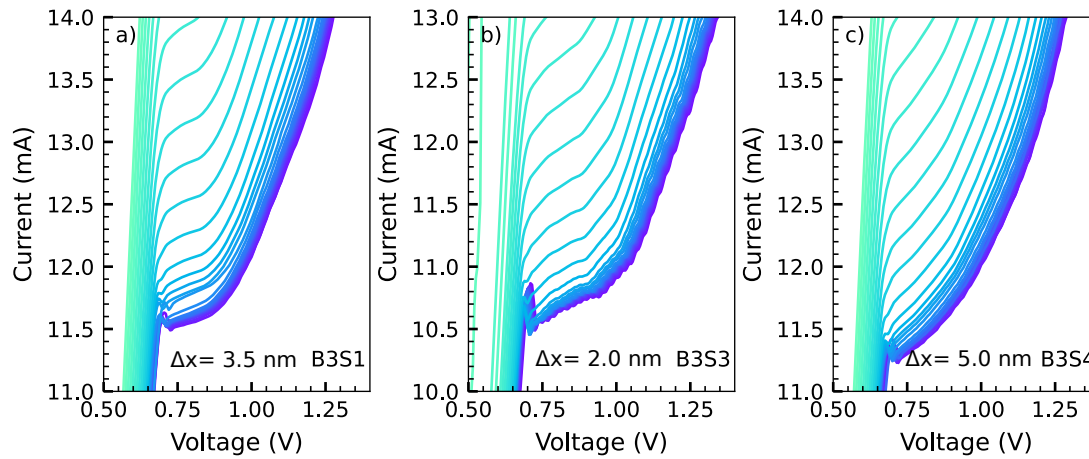
Figure 5.9: Comparison of samples with different dopant position inside the well. Zoom-in on the first plateau for the structures B3S1, B3S3, and B3S4, with $\Delta E=$ 36 meV. For B3S3 and B3S4 the dopant position inside the well was moved from 3.5 nm from the left barrier in the growth direction to 2.0 nm and 5.0 nm away respectively. The I-Vs are measured in temperature steps of 5 K from 5–140 K. For the color scale please refer to Fig.5.3. Data partly from [132].

increasing ΔE the dopant position is increasingly closer to the barrier grown before, compare table 5.1. The same effect of the increased amplitude of the initial peak is observed.

5.3.6 Effects of doping concentration

For sample B2S3 and sample B3S5, the doping concentration within the 5 nm doped region inside the well was varied. Excluding the doping concentration, B2S3 is a regrowth of B1S4 with $\Delta E=$ 44 meV, which showed the anomalous temperature effect. Except for the doping, B3S5 is a regrowth of B3S1 with $\Delta E=$ 36 meV, which did not show an anomalous temperature effect. For B2S3 the doping was doubled to 4×10^{16} cm^{-3} and for B3S5 it was halved to 1×10^{16} cm^{-3}. The results are plotted in Fig.5.10. Fig.5.10 a) shows the temperature-dependent I-V curves of B3S5 where the doping was halved. When comparing it to its reference regrowth B3S1, see Fig.5.9 a) it is apparent that the anomalous temperature effect is now observed, while it was not before in B3S1. When doubling the doping in B2S3 the anomalous temperature disappears in comparison to the reference B2S1, see Fig. 5.7 b). On the other hand, the NDR segments indicating a charge accumulation layer at the boundary between high- and low-field domain increase in amplitude.

Note, that the NDR segments in the second plateau are prominent and strong confinement is visible, which is not observed in any other structure. A further effect
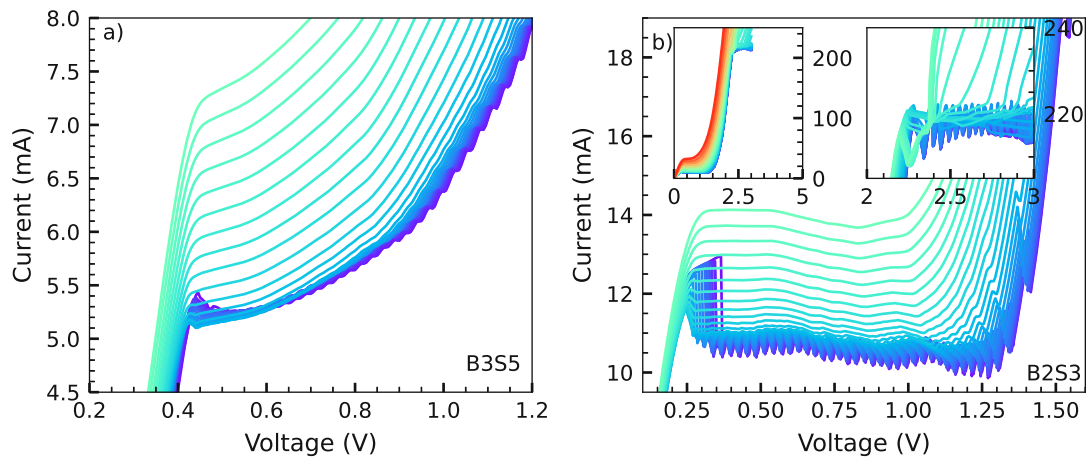
Figure 5.10: Comparison of structures with different amounts of doping inside the well. Zoom-in on the first plateau for the structures B3S5 (ΔE= 36 meV), and B2S3 (ΔE= 44 meV), where the doping was halved and doubled from the initial, respectively. Note, that initial growths of structures with ΔE= 36 meV did not show an anomalous temperature effect, but structures with ΔE= 44 meV did. a) has half the doping (1×10^{16} cm^{-3}) NDR segments and an initial anomalous temperature effect are visible, while it is not visible for b) with double the doping 4×10^{16} cm^{-3}. Instead, the NDR segments increase in amplitude, even for the second plateau in the inset, where strong confinement is still visible, which is not the case for a). For the color scale please refer to Fig.5.3. Data partly from [132].
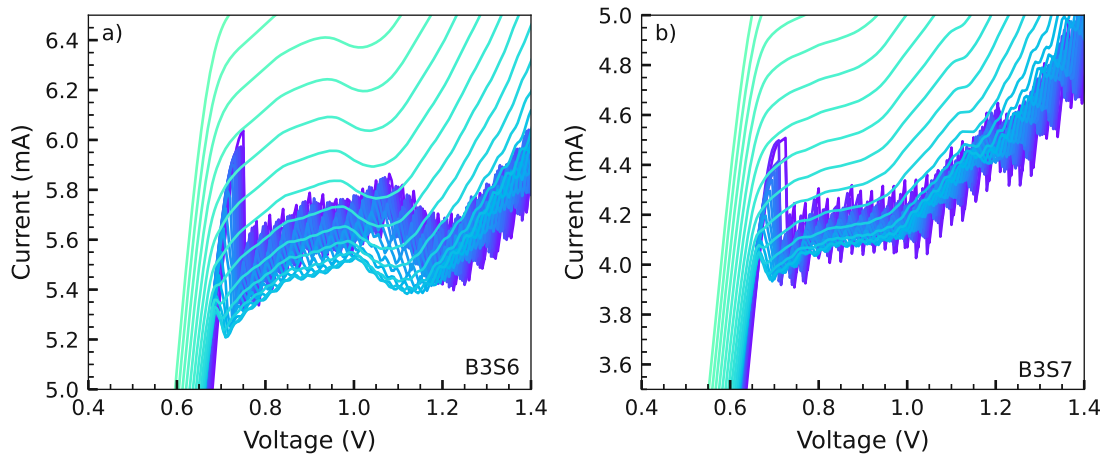
Figure 5.11: Comparison of samples with different contact layers. a) is the reference regrowth B3S6 of the $\Delta E= 44\,\text{meV}$ structure B1S4 with $100\,\text{nm}$ top and $250\,\text{nm}$ bottom contacts doped $5\times10^{18}\,\text{cm}^{-3}$. b) B3S7 is also a regrowth of B1S4, but $50\,\text{nm}$ spacer layers doped $5\times10^{17}\,\text{cm}^{-3}$ were included between the $100\,\text{nm}$ thick $5\times10^{18}\,\text{cm}^{-3}$ doped top and bottom contact and the low doped superlattice. Including the spacer layers results in a significant reduction of the anomalous temperature effect. Data partly from [132].

is an increase in the amplitude of the initial peak at the first plateau.

5.3.7 Effects of grown contact layers

The grown contact layer thickness varied between $100 - 250\,\text{nm}$ for the different batches, the thicknesses also varied between the bottom and top contact, but the contact layer doping stayed the same at $5\times10^{18}\,\text{cm}^{-3}$. For the last sample of batch 3, B3S7, lower doped spacer layers ($5\times10^{17}\,\text{cm}^{-3}$, $50\,\text{nm}$ thick) were included between the highly doped contact layers ($5\times10^{18}\,\text{cm}^{-3}$, $100\,\text{nm}$ thick) and the superlattice. Additionally, a reference regrowth of B1S4 was grown, namely B3S6, which exhibits the anomalous temperature effect as expected from previous results, see Fig. 5.11 a). The results for B3S7 are plotted in Fig.5.11 b). It is visible that in comparison to its reference B3S6, the anomalous temperature effect significantly decreases. The current at the first plateau remains constant below $100\,\text{K}$, before it increases with temperature, so there is no inflection point. The NDR segments are still present.

5.3.8 Summary of the experimental results

The systematic experimental study of the superlattice structures is summarized. From the comparison of the reference regrowths, which were done as the first sample of every subsequent batch it can be concluded that the anomalous temperature effect

and its inflection point do not depend on the fabricated contact (Schottky contact or ohmic contact). Furthermore, there is no effect from moving the dopant position in the well closer or further away from the previously grown barrier, see Fig. 5.9. This means that in the temperature-dependent I-V curves there was further no evidence of the formation of DX centers, which form due to dopant diffusion into the AlGaAs barriers. Bright temperature-dependent I-V measurements, see Fig. 5.6, where the cryostat was illuminated with a red LED during the measurements did not alter the anomalous temperature effect, indicating that the anomalous temperature effect does not occur due to some form of temperature activated trap or impurity. Furthermore, Arrhenius plots, see Fig. 5.5 yielded an in comparison to GaAs traps in literature smaller activation energy, which also excludes traps being the cause.

What affects the anomalous temperature effect is ΔE, as observed for the samples of B1, see Fig.5.4. The inflection point of the anomalous temperature effect shifts to higher temperatures with increasing ΔE. The anomalous temperature effect is also affected by the doping concentration in the wells. The effect increases when reducing the doping ($1{\times}10^{16}\,\mathrm{cm^{-3}}$), see Fig.5.10 a), and it disappears for higher doping in the wells ($> 2{\times}10^{16}\,\mathrm{cm^{-3}}$), see Fig.5.10 b). In the latter case, the NDR segments strongly increase in amplitude. Additionally, the anomalous temperature effect disappears below a certain barrier thickness, see Fig. 5.7 c), but it is significantly increases when increasing the Al content in the barriers, see Fig. 5.8. This can be understood by the reduced/ increased carrier confinement of the structure. This is supported by the second plateau disappearing in the structure with thinner barriers, see Fig. 5.7 c). Furthermore, the anomalous temperature effect is significantly reduced with the inclusion of low-doped spacer layers between the highly-doped contacts and the low-doped superlattice, see Fig. 5.11. This points out that the cause of the anomalous temperature effect cannot be intrinsic to the superlattice.

These results highlight that the anomalous temperature effect is clearly dependent on the available carriers in the structure as well as the grown contact layers. As discussed before, the cause does not lie in traps, but the results strongly point towards band bending effects due to the high difference in doping between the highly doped contact layers and the low doped superlattice. Because of this, Schrödinger-Poisson simulations using CLAUS (a group-intern simulation tool) and multi-scattering Büttiker (MSB) simulations from the nextnano software [144] are conducted in the following.
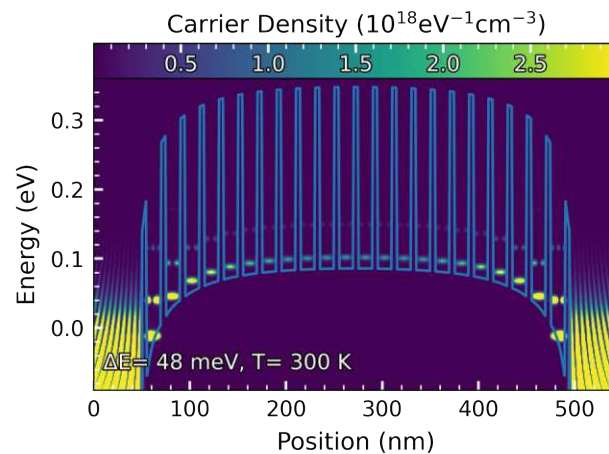
Figure 5.12: Typical MSB simulation of a reference superlattice structure with 22 periods at 0 V bias.

5.4 Multi-scattering Büttiker (MSB) simulations

To gain an understanding of the temperature-dependent mechanics of the anomalous temperature effect, MSB simulations were conducted. This simulation tool is explicitly developed for calculating the transport in QCLs and resonant tunneling diodes by the company nextnano GmbH and is included in the nextnano software [144].

5.4.1 Introduction

MSB simulations use a generalized Büttiker probe model [145, 146], which takes individual scattering mechanisms such as LO- phonon, acoustic- phonon as well as interface roughness scattering into account. The model is fed by self-energies derived from the nonequilibrium Green's function method but sidesteps in the self-consistent calculation of lesser self-energies, which are replaced by a quasi-equilibrium expression. This makes MSB simulations orders of magnitudes more efficient than the fully self-consistent non-equilibrium Green's functions (NEGF) method [147]. A detailed discussion of this model goes over the scope of this chapter, the reader is referred to [148]. The effectiveness of this model (especially important due to the limited simulation-power capacity during the time these simulations were conducted) but still including relevant mechanisms are the main reasons why this simulation tool was employed.

Representative structures were simulated using the nextnano MSB simulation tool to make the simulation time more feasible. Simulations were performed with 22 periods (instead of 45) of the superlattice structure between 50 nm thick 5×10^{18} cm^{-3} doped contacts (for the real grown thickness, please refer to table 5.1.). The doping
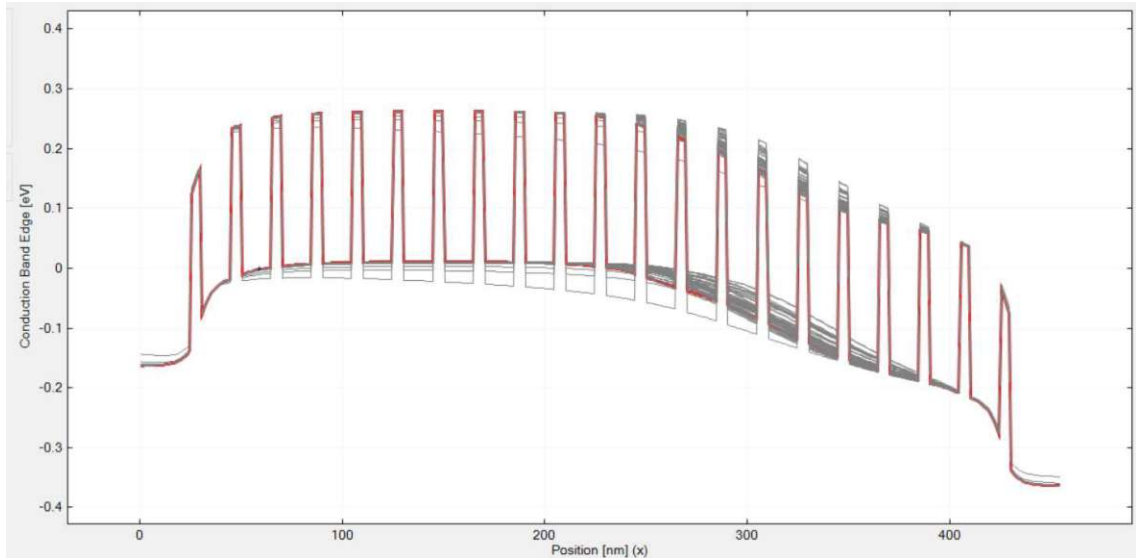
Figure 5.13: MSB simulations performed at $150\,\mathrm{K}$ and a bias of $0.2\,\mathrm{V}$ of an exemplary superlattice, laid over each other, the band structure plotted in red is the last simulation, showing a multi-stable regime in the high-field domain.

inside the superlattice has been averaged over the entire well. In Fig. 5.12 a typical MSB simulation of a superlattice structure at $300\,\mathrm{K}$ at $0\,\mathrm{V}$ bias is plotted. Notice the strong band bending of the superlattice near the highly doped contact layers.

5.4.2 Temperature and bias dependent convergence

The nextnano MSB code consists of a chain of interlinked iterations, which have to converge separately. The program starts with a self-consistent iteration to calculate the retarded Green's functions. It proceeds with the calculations of the Green's functions and the probe calculation. After this, an inner Poisson iteration is conducted, from this a corrector factor is calculated, which is referred to as the outer Poisson iteration. This scheme repeats itself until the outer Poisson iteration converges or the maximum iteration number is reached, which also accounts for the inner iterations. Convergence means that a predefined Delta value, set by the user, is reached. For these simulations, the Delta values were taken from sample files nextnano provided. There was mostly no problem in the convergence of the retarded Green's functions (Delta = $3\times10^{-7}\,\mathrm{1/nm/eV}$) and the inner Poisson iterations (Delta = $3\times10^{7}\,\mathrm{1/cm^3}$) the outer Poisson iteration (Delta = $1\times10^{-4}\,\mathrm{V}$) had problems to converge for low temperatures and/or applied bias. The outer Poisson final Delta was around $1\times10^{-3}\,\mathrm{V}$ for simulations that did not converge.

Fig. 5.13 shows the band structure solution of an exemplary simulation that did not converge. It is visible that no good convergence was reached in the high-field domain,
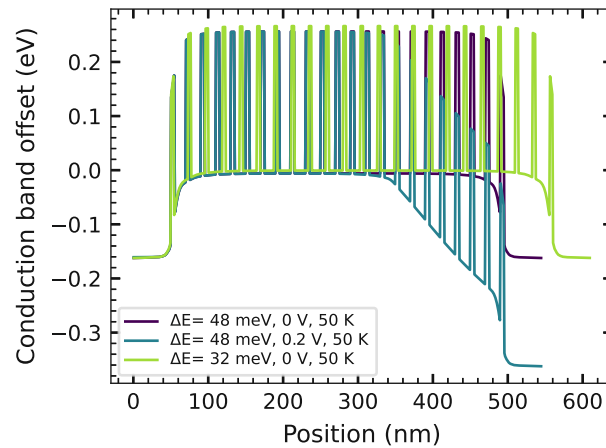
Figure 5.14: Comparison of the band bending of different structures, with and without applied bias at 50 K. The given ΔE corresponds to the energy separation at alignement bias.

but that the solution oscillated between maximum values while the low-field domain converged nicely. In literature multistabilities are observed in the I-V measurements, see [52]. Depending on the starting voltage, different stable current points are reached. Therefore, it is not clear if the simulation did not converge due to computational reasons or because multi-stable regimes exists.

5.4.3 Multi-scattering Büttiker (MSB) simulation results

An explanation of the temperature dependency of the anomalous effect can be given using the MSB simulations. First, a detour has to be taken to determine the dependency of the observed band bending. For this, simulations of samples with different barrier widths, ΔE, or applied bias were conducted.

Fig. 5.14 compares the simulated band structure of these samples at 50 K. It is apparent that the initial band bending is independent of the structure because it mainly depends on the doping difference between the contact layers and the superlattice. Furthermore, band bending is temperature dependent, due to the temperature dependency of the carrier distribution. For the biased structure, the initial band bending is the same, because a low- and high-field domain form, see section 2.3.2. With increasing bias, the high-field domain moves along the entire structure. In the I-V, a plateau forms during this process, meaning that the current stays constant. The initial band bending is unaffected over the length of the plateau in the I-V, which means that for the understanding of the anomalous temperature effect, MSB simulations at 0 V bias are sufficient. Fig. 5.14 plots a structure with $\Delta E =$ 32 meV, which does not show the anomalous temperature effect. Nevertheless, this

structure exhibits the same band bending as structures that do show the anomalous temperature effect. This result shows that all grown superlattice structures exhibit the same band bending of the first few periods independent of if the anomalous temperature effect was observed or not. The answer to the question of what causes the effect can be found when understanding the temperature dependency.

Fig. 5.15 shows the average current at the first plateau plotted over the temperature for sample B1S5 with $\Delta E = 48$ meV. The current first decreases and shows a minimum at 110 K before it increases again with temperature. MSB simulations at three temperature points give a possible explanation: At 50 K the ground state of the first well is miss-aligned with the ground state of the second well due to band bending. The current is limited by this misalignment and decreases as the misalignment increases due to increasing band bending with increasing temperature. At 90 K the first excited state of the first well becomes populated and can finally contribute to the current flow, but it is not perfectly aligned to the ground state of the second well yet. From this point on, the current increases again with increasing temperature. Fig. 5.15 shows that the first excited state of the first well is perfectly aligned to the ground state at 250 K (which is already the case starting from 150 K) and that the population increased. This understanding gives a possible explanation of why the anomalous temperature effect is not observed for smaller energy separation like $\Delta E = 32$ meV. Here the first excited state of the first well is already perfectly aligned to the ground state of the next well at a temperature of 50 K because the levels are closer together, see Fig. 5.16. This figure shows the case for $\Delta E = 32$ meV in comparison to $\Delta E = 48$ meV for two different temperatures.

As noted before, the band bending is dependent on the doping difference and although it is the trigger for the anomalous temperature effect, it is also present in samples where no anomalous temperature effect was observed. In these cases, its effects are overshadowed by less carrier confinement (too thin barriers) or by the concentration of carriers (double doping in the wells). The simulations also predict how the band bending can be decreased. Namely, by the inclusion of a low - or preferably - undoped spacer layer between the highly doped contacts and the superlattice. Fig. 5.16 f) and g) show the band bending dependency on the spacer layers for two different temperatures. It is observed that for a 25 nm spacer layer the first well remains in good alignment with the ground state of the second well with increasing temperature and thus no reduction in the current flow through the structure occurs.

Finally, simulations with an applied bias show the formation of a low- and high-field domain, as predicted in literature, see Fig. 5.17.
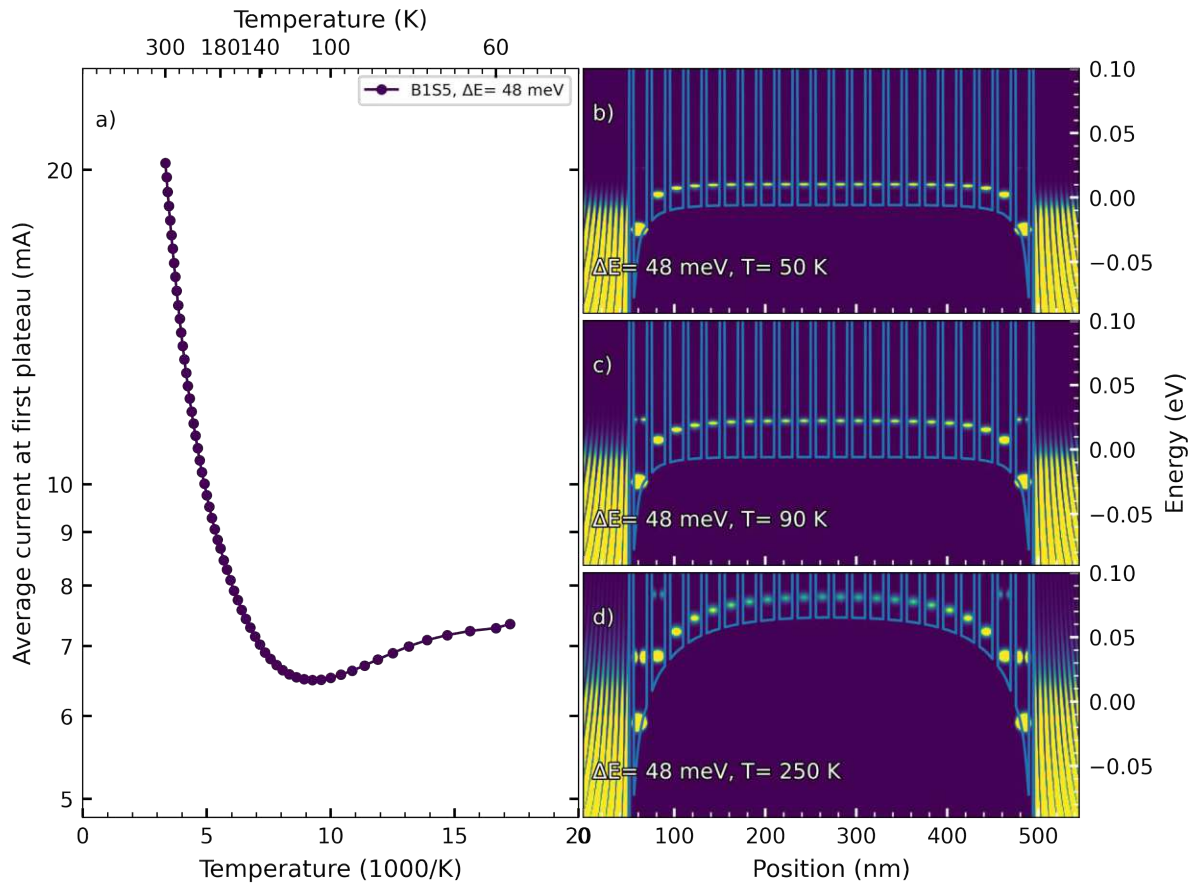
Figure 5.15: Investigation of the temperature dependency of the anomalous temperature effect. a) Experimental results of the average current at the first plateau plotted over the temperature for sample B1S5. b)-d) MSB simulations of the band structure and the carrier distributions for $\Delta E = 48\,\text{meV}$ and b) $50\,\text{K}$, c) $90\,\text{K}$, and d) $250\,\text{K}$. Note, that in b) at $50\,\text{K}$ the first excited state in the first well is not occupied, while slight occupation is visible at $90\,\text{K}$ in c). At d) $250\,\text{K}$ the first excited state is fully occupied and perfectly aligned to the ground state of the second well, which promotes current transport. The simulations in b)–d) fit together with the experimental results in a).
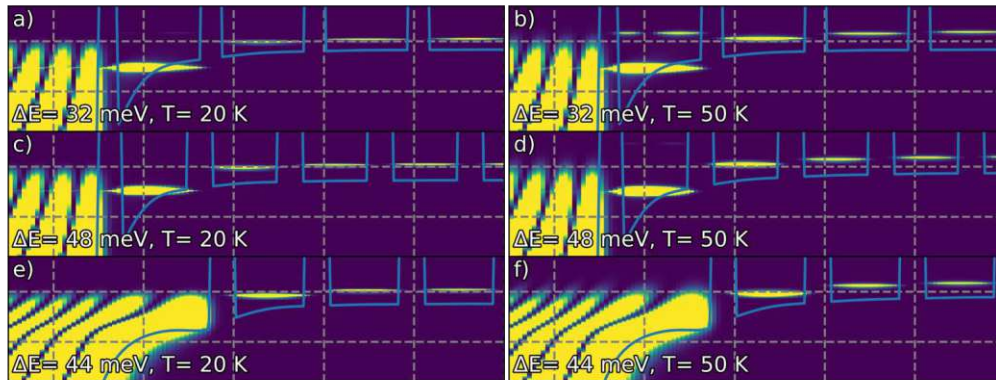
Figure 5.16: Investigation of the temperature dependency of structures with different ΔE and the inclusion of a spacer layer. a) and b) simulation with $\Delta E=$ 32 meV at 0 V, at 20 and 50 K. d) and e) show the case for $\Delta E=$ 48 meV at 20 and 50 K. f) and g) show the influence of the inclusion of a 25 nm-thick 5×10^{17} cm^{-3} doped spacer layer between the contact layer and the superlattice. The band bending of the first well is greatly reduced. The temperature influence on the level alignment decreased between 20 and 50 K.
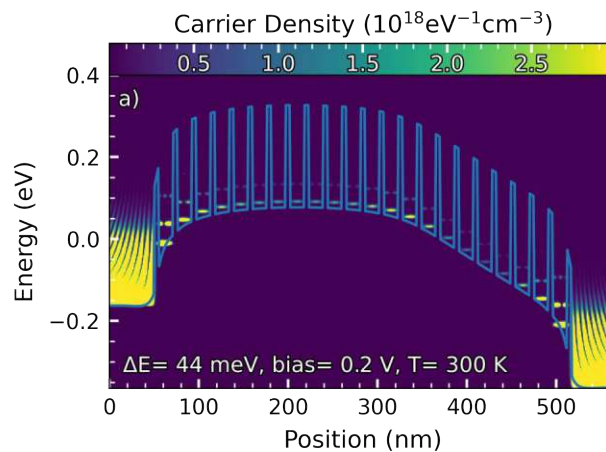
Figure 5.17: MSB simulation of a structure with $\Delta E=$ 44 meV at 300 K with an applied bias of 0.2 V. Note, that a low- and high-field domain form, but the initial band bending is still present. Also, a slight charge accumulation layer is visible at the domain boundary.

5.5 Summary and conclusion

In conclusion, the systematic study of low-doped GaAs/AlGaAs superlattice structures over three growth campaigns indicates no correlation between the anomalous temperature effect and the fabricated contacts (Schottky or Ohmic). There is also no indication of this effect occurring due to traps, impurities, or the diffusion of the Si dopants into the AlGaAs barriers, which is causing DX centers. On the other hand, the effect is dependent on the doping concentration, while lower doping ($> 2 \times 10^{16}\,\mathrm{cm^{-3}}$) increases the anomalous temperature effect and higher doping ($4 \times 10^{16}\,\mathrm{cm^{-3}}$) makes it disappear, see Fig.5.10. With the simulation results from section 5.4 a possible explanation is given by the increased availability of carriers to overcome the levels misalignment caused by the band bending at the first periods of the superlattice structure due to three orders of magnitude difference in doping to the highly doped contact layers. This also strongly increases the charge accumulation layer at the domain boundary causing an increased amplitude of the NDR segments occurring at the plateaus. The anomalous temperature effect is also dependent on the barrier thickness, it disappears for barrier thicknesses $\leq 3.5\,\mathrm{nm}$, due to reduced carrier confinement, which is also indicated by the absence of NDR segments in the plateau. Although for both cases the anomalous temperature effect disappears, it is important to mention, that the band bending does not disappear, but its effects are overshadowed by the concentration of carriers. Finally, the effect also shows a strong dependency on the grown contact layers. The simulation results in section 5.4 display strong band bending of the first periods of the superlattice. For this reason, a lower doped ($5 \times 10^{17}\,\mathrm{cm^{-3}}$) spacer layer between the highly doped contact layers ($5 \times 10^{18}\,\mathrm{cm^{-3}}$) was included, which reduces band bending in this region. Indeed the anomalous temperature effect significantly decreases, see Fig.5.11.

MSB simulations of reference structures with 22 periods of the superlattices between $50\,\mathrm{nm}$-thick $5 \times 10^{18}\,\mathrm{cm^{-3}}$ doped contacts and an applied bias of $0.2\,\mathrm{V}$ agree with the literature with the formation of a low field domain separated by a charge accumulation layer from a high field domain. Strong band bending of the superlattice at the contacts is also observed, which agrees with Schrödinger-Poisson simulations at $0\,\mathrm{V}$ applied bias.

The temperature dependency of the anomalous temperature effect are explained with the results from the MSB simulations of section 5.4. Two main effects are observed from the simulations: The band bending increases with temperature as well as the population in the excited states. From the experimental results the observation was made that the inflection point of the anomalous temperature effect correlates with ΔE, see Fig.5.4. There is no anomalous temperature effect at $\Delta E = 32\,\mathrm{meV}$

but starting from $\Delta E = 36\,\mathrm{meV}$ the inflection point moves to higher temperatures with increasing ΔE. The observations from simulations and experiments coalesce in the following way: The simulations show strong band bending mainly of the first few quantum wells and especially between the first two quantum wells neighboring the highly doped contacts. Because the band bending increases with temperature the states of the first well move down relative to the states in the second quantum well. Additionally, higher states are more populated with increasing temperatures. At some point an alignment of the first excited state of the first quantum well occurs with the ground state of the second quantum well, enabling a more efficient current transport. The temperature at which this alignment occurs is strongly dependent on the separation between the ground state and the first excited state, in other words, ΔE. The simulations show that this alignment occurs for a $\Delta E = 32\,\mathrm{meV}$, already at $50\,\mathrm{K}$, while it happens at $150\,\mathrm{K}$ for a $\Delta E = 48\,\mathrm{K}$, see Fig.5.16. Following these results, the temperature at the inflection point, where the least current flow occurs, corresponds to the worst alignment of the states between the first two quantum wells. The simulations also show that a way to resolve this issue is by including a low-doped (undoped) spacer layer between the superlattice and the highly doped contacts, which drastically decreases the band bending. Based on this study the influence of band bending on the effectiveness of the active region design of THz QCLs is not negligible and the addition of spacer layers is recommended.

CHAPTER 6

Conclusions and outlook

This thesis concentrates on zinc-blende III-V semiconductor devices, which are used for lasers and detectors in the mid-infrared. Over the duration of this Ph.D. thesis, a multitude of devices were grown with molecular beam epitaxy (MBE), fabricated in the cleanroom, and characterized in the optical lab. The devices that this thesis emphasizes are quantum cascade detectors (QCDs), quantum cascade lasers (QCLs), and basic superlattices.

The beauty of MBE is its diversity in research and industry. Heterostructures, to study intrinsic material parameters or highly optimized devices can be produced. New materials can be studied or mature materials can be grown with the utmost film quality and monolayer precision.

In this thesis, comprehensive research into the design and growth of such devices is performed. Mature and novel materials were grown and intersubband physics and novel effects occurring in heterostructures were studied. In particular, QCDs were expanded to the novel InAs/Al(As)Sb material system, grown on InAs and GaSb substrates. This material system offers a low effective electron mass, beneficial for a high optical transition strength and thus increased responsivity, and a large conduction band offset (CBO), which allows for a wide tunability in the design of the absorption wavelengths from mid-infrared (MIR) towards the short-infrared. A high CBO also reduces the noise, benefiting the detectivity. The entire growth process was optimized to grow high-quality InAs/Al(As)Sb, including the thermal optimal oxide removal temperature, group-V fluxes, shutter sequences for sharp interfaces, and eliminating group-V interdiffusion between the InAs/Al(As)Sb layers. QCDs

were designed and grown with intersubband absorption wavelengths ranging from 2.7–5.5 µm, demonstrating the wide range and expanding the application range by increasing the maturity of short-infrared QCDs. The absorption wavelengths of the grown devices fit the simulation when using an effective electron mass for InAs of $0.0235\,m_0$. This is not the value of $0.026\,m_0$, but within the range of values from literature in reference [126].

On GaSb substrates, InAs/AlSb QCDs were grown strain-balanced, due to the lattice mismatch and critical film thicknesses of InAs and AlSb on GaSb of approximately 35 nm. InAs and AlSb have opposing strains on GaSb and the necessary strain balancing ratio of InAs:AlSb is, therefore, approximately 1:1. A design of a QCD structure with this layer thickness constraint would yield immense losses in the detector figures of merit. In this thesis, the growth of QCDs was developed with an InAs:AlSb ratio of 3:1, with the help of sub-monolayer strain-balancing InSb layers. This gives back the freedom of a lattice-matched material system in device design and, as a result, optimized QCD designs were grown. Indeed, (224) reciprocal space map (RSM) high-resolution X-ray diffraction (HR-XRD) scans showed the achievement of perfectly strain-compensated grown QCD structures. This method of strain-balancing InAs/AlSb heterostructures could also be extended to other intersubband devices.

On GaSb substrates four complete QCDs structures were grown, with detection wavelengths ranging from 3.65–5.5 µm. The room-temperature responsivity measured in the 45° facet double-pass configuration, attributed to the QCD intersubband transition ranged from 5.89 mA/W for the QCD at 5.5 µm to 16.12 mA/W for a QCD detecting at 4.3 µm. This is compared to the 10 mA/W of an optimized QCD design at 4.3 µm grown in the mature InGaAs/InAlAs material system, lattice-matched to InP [68]. The increase in responsivity for the device grown in the InAs/AlSb material system is attributed to the lower effective electron mass of this system.

The extension to smaller wavelengths / higher transition energies is not possible in material systems like lattice-matched InGaAs/InAlAs, due to the magnitude of the CBO. In the $InAs/AlAs_{0.16}Sb_{0.84}$ material system lattice-matched to InAs, a QCD was realized with an absorption energy corresponding to the design of 2.7 µm. This energy lies above the bandgap energy of the InAs substrate of 0.417 eV (2.97 µm) [25]. Such a device was realized with a sub-wavelength surface diffraction grating, allowing for top-side illumination, which is usually forbidden for QCDs, due to the intersubband selection rule, circumventing the strong absorption of the substrate.

The InAs/Al(As)Sb material system offers a type-II band alignment, where the

conduction band edge of InAs is below the valence band edge of AlSb. The effective bandgap for interband transitions from the AlSb valence band to states in the InAs conduction band, therefore, matches the energy of the near-infrared region and strong broadband interband signals are observed along with the QCD signal in spectra of those devices, with a spectral range from 1.2–3 µm. These are quite high cut-on energies in the near-infrared, due to the high ground states in the extraction ladder. The interband spectral range was influenced by the QCD design and showed a strong bias dependence, while the QCD signal was not influenced. What is unusual is that these interband transitions are transitions from a valence-miniband to single conduction band states in the QCD active region. These near-infrared interband transitions are only possible in low-bandgap type-II material systems and are possibly also occurring with higher transition energies and with less efficiency in other material systems with higher bandgap. With this explanation of the origin of the interband signal the QCD optical transition needs to take place (except in the last period) to measure a photocurrent.

Based on this explanation, in the future, it would be of interest to obtain a spectrum where the QCD transition is hindered for example by a long-pass filter. Additionally, it would be interesting to evaluate the speed of those transitions and how an applied bias can influence it, because, in contrast to the states in the condition band, the valence-miniband has no preferred carrier transport direction. Bias-dependent measurements should also be measured polarization-dependent to gain more insight into the mechanism of the interband signal. It would be of interest to see how design variations, e.g., thicker barriers or different thicknesses of barriers, which could lead to the break up of the miniband, would influence the interband absorption spectrum and tune the cut-on of the signal. Furthermore, it would be of interest how n-type doping of the wells in the extractor, which are undoped in the QCDs of this thesis, would influence the observed interband signal. By doing this, the different forms of loss mechanisms in interband structures could be studied.

As mentioned, MBE is a versatile tool, with which heterostructures can be grown to study material and intersubband device physics. QCLs are one of the most important coherent, powerful, compact light sources in the mid-infrared to the THz region. Until now, no room-temperature operation in the THz regime has been achieved. On the quest for high-temperature THz QCLs, an anomalous temperature behavior of the threshold current that occurs in some devices was investigated, the threshold current first decreases before it increases again with temperature in contrast to most QCLs with an exponential increase in the threshold current with temperature. A systematic study with more straightforward and, thus, easier-to-interpret superlattice structures

was conducted to investigate this effect. These superlattice structures were similarly low-doped as THz QCLs, with comparable growth conditions and fabricated contacts, which showed the same anomalous temperature effect in their current-voltage (I-V) characteristics. The study showed no correlation between the anomalous temperature effect and Schottky or Ohmic fabricated contacts, traps, impurities, or diffusion of Si dopants into the AlGaAs barriers, which cause donor-complex (DX)-centers. This research found a dependency on the energy level separation and the doping concentration in the quantum wells, where the anomalous temperature effect increased with lower doping in the superlattice, and disappeared with higher doping. The inverse temperature dependency was found for the increasing barrier thicknesses. Schrödinger-Poisson simulations showed strong band bending at the first few periods, following the highly-doped contact layers. Based on multi-scattering Büttiker (MSB) simulation results, it was concluded that the anomalous temperature effect disappears, due to the increased availability of carriers with higher doping and less confinement. The temperature dependence of the anomalous temperature effect was explained with the help of MSB simulations, demonstrating the temperature dependence of the band bending and carrier occupation, in correlation with the energy level separation of the superlattice structure. To confirm the assumption that the anomalous temperature effect stems from band bending, which acts as a bottleneck for carrier transport, a superlattice structure with lower-doped spacer layers between the highly-doped contact layers and the low-doped superlattice was grown. The anomalous effect significantly decreased, in agreement with the simulation. The strong band bending, due to the high doping difference was observed in simulations regardless of the occurrence of the temperature effect. This is also true for THz QCLs, which have the same difference in doping of the contact superlattice and the active region. These results emphasize the importance of the contact layers in optimizing the active region. This study shows that the influence of band bending on the effectiveness of the active region design of THz QCLs is not negligible. Based on the results, it is recommended to include undoped GaAs spacer layers between the highly doped contact layers and the low-doped active region in future THz QCL designs.

Bibliography

[1] Z. Liu, C. Zheng, T. Zhang, Y. Li, Q. Ren, C. Chen, W. Ye, Y. Zhang, Y. Wang and F. K. Tittel. *Midinfrared sensor system based on tunable laser absorption spectroscopy for dissolved carbon dioxide analysis in the south china sea: System-level integration and deployment.* Analytical Chemistry 92 (12): 8178–8185 (2020). doi: 10.1021/acs.analchem.0c00327 – cited on page 1.

[2] S. Primpke, M. Godejohann and G. Gerdts. *Rapid identification and quantification of microplastics in the environment by quantum cascade laser-based hyperspectral infrared chemical imaging.* Environmental Science &amp Technology 54 (24): 15893–15903 (2020). doi: 10.1021/acs.est.0c05722 – cited on page 1.

[3] G. W. Santoni, B. C. Daube, E. A. Kort, R. Jiménez, S. Park, J. V. Pittman, E. Gottlieb, B. Xiang, M. S. Zahniser, D. D. Nelson, J. B. McManus, J. Peischl, T. B. Ryerson, J. S. Holloway, A. E. Andrews, C. Sweeney, B. Hall, E. J. Hintsa, F. L. Moore, J. W. Elkins, D. F. Hurst, B. B. Stephens, J. Bent and S. C. Wofsy. *Evaluation of the airborne quantum cascade laser spectrometer (QCLS) measurements of the carbon and greenhouse gas suite – CO_2, CH_4, N_2O, and CO and HIPPO campaigns.* Atmospheric Measurement Techniques 7 (6): 1509–1526 (2014). doi: 10.5194/amt-7-1509-2014 – cited on page 1.

[4] D. D. Nelson, B. McManus, S. Urbanski, S. Herndon and M. S. Zahniser. *High precision measurements of atmospheric nitrous oxide and methane using thermoelectrically cooled mid-infrared quantum cascade lasers and detectors.* Spectrochimica Acta Part A: Molecular and Biomolecular Spectroscopy 60 (14): 3325–3335 (2004). doi: https://doi.org/10.1016/j.saa.2004.01.033 – cited on page 1.

[5] B. Jean and T. Bende. *Mid-IR Laser Applications in Medicine*, 530–565. Springer Berlin Heidelberg, Berlin, Heidelberg (2003). doi: 10.1007/3-540-36491-9$_1$2 – cited on page 1.

[6] A. Schwaighofer, M. Brandstetter and B. Lendl. *Quantum cascade lasers (QCLs) in biomedical spectroscopy.* Chemical Society Reviews 46 (19): 5903–5924 (2017). doi: 10.1039/c7cs00403f – cited on page 1.

[7] U. Willer, M. Saraji, A. Khorsandi, P. Geiser and W. Schade. *Near- and mid-infrared laser monitoring of industrial processes, environment and security applications.* Optics and Lasers in Engineering 44 (7): 699–710 (2006). doi: 10.1016/j.optlaseng.2005.04.015 – cited on page 1.

[8] J. Darmo, V. Tamosiunas, G. Fasching, J. Kröll, K. Unterrainer, M. Beck, M. Giovannini, J. Faist, C. Kremser and P. Debbage. *Imaging with a terahertz quantum cascade laser.* Opt Express 12 (9): 1879–1884 (2004). doi: 10.1364/OPEX.12.001879 – cited on page 1.

[9] R. Martini and E. Whittaker. *Quantum cascade laser-based free space optical communications.* Journal of Optical and Fiber Communications Reports 2 (4): 279–292 (2005). doi: 10.1007/s10297-005-0052-2 – cited on page 1.

[10] G. Marschick, M. David, E. Arigliani, N. Opačak, B. Schwarz, M. Giparakis, A. Delga, M. Lagree, T. Poletti, V. Trinite, A. Evirgen, B. Gerard, G. Ramer, R. Maulini, J. Butet, S. Blaser, A. M. Andrews, G. Strasser and B. Hinkov. *High-responsivity operation of quantum cascade detectors at 9 μm.* Optics Express 30 (22): 40188–40195 (2022). doi: 10.1364/OE.470615 – cited on page 1.

[11] B. Schwarz. *Monolithic integration of mid-infrared photonics.* Ph.d. thesis, TU Wien, Institute of Solid State Electronics (2015) – cited on pages 2, 16, and 20.

[12] B. Schwarz, P. Reininger, D. Ristanić, H. Detz, A. M. Andrews, W. Schrenk and G. Strasser. *Monolithically integrated mid-infrared lab-on-a-chip using plasmonics and quantum cascade structures.* Nature Communications 5: 4085 (2014). doi: 10.1038/ncomms5085 – cited on pages 2 and 30.

[13] C. Gmachl, F. Capasso, D. L. Sivco and A. Y. Cho. *Recent progress in quantum cascade lasers and applications.* Reports on progress in physics 64 (11): 1533 (2001) – cited on pages 2 and 24.

[14] B. Wen and D. Ban. *High-temperature terahertz quantum cascade lasers.* Progress in Quantum Electronics 80: 100363 (2021). doi: 10.1016/j.pquantelec.2021.100363 – cited on pages 2 and 102.

[15] A. Delga. *Quantum cascade detectors: A review.* Mid-infrared Optoelectronics 337–377 (2020) – cited on pages 2, 24, 26, 30, and 31.

[16] F. R. Giorgetta, E. Baumann, M. Graf, Q. Yang, C. Manz, K. Kohler, H. E. Beere, D. A. Ritchie, E. Linfield, A. G. Davies, Y. Fedoryshyn, H. Jackel, M. Fischer, J. Faist and D. Hofstetter. *Quantum cascade detectors.* IEEE Journal of Quantum Electronics 45 (8): 1039–1052 (2009). doi: 10.1109/jqe.2009.2017929 – cited on pages 2, 24, 26, 27, 28, and 73.

[17] A. Rogalski, P. Martyniuk and M. Kopytko. *InAs/GaSb type-II superlattice infrared detectors: Future prospect.* Applied Physics Reviews 4 (3): 031304 (2017). doi: 10.1063/1.4999077 – cited on page 2.

[18] P. Martyniuk, M. Kopytko and A. Rogalski. *Barrier infrared detectors.* Opto-Electronics Review 22 (2) (2014). doi: 10.2478/s11772-014-0187-x – cited on page 2.

[19] Y. Chen, X. Chai, Z. Xie, Z. Deng, N. Zhang, Y. Zhou, Z. Xu, J. Chen and B. Chen. *High-speed mid-infrared interband cascade photodetector based on InAs/GaAsSb type-II superlattice.* Journal of Lightwave Technology 38 (4): 939–945 (2020). doi: 10.1109/jlt.2019.2950607 – cited on page 2.

[20] A. Rogalski. *HgCdTe infrared detector material: history, status and outlook.* Reports on Progress in Physics 68 (10): 2267–2336 (2005). doi: 10.1088/0034-4885/68/10/r01 – cited on page 2.

[21] *Hamamatsu webpage.* https://www.hamamatsu.com/jp/en/product/optical-sensors/photodiodes.html. Accessed: 2023-08-22 – cited on page 2.

[22] *Nanoplus webpage.* https://nanoplus.com/. Accessed: 2023-08-22 –

[23] *Vigo photonics webpage.* https://vigophotonics.com/. Accessed: 2023-08-22 – cited on page 2.

[24] G. Bastard. *Wave mechanics applied to semiconductor heterostructures* (1990) – cited on pages 5, 6, 7, 8, 9, 17, and 18.

[25] I. Vurgaftman, M. P. Lumb and J. R. Meyer. *Bands and Photons in III-V Semiconductor Quantum Structures*, volume 25. Oxford University Press (2020) – cited on pages 5, 12, 26, 30, 38, 39, 74, and 126.

[26] J. Faist. *Quantum Cascade Lasers*. Oxford University Press, Oxford (2013). ISBN: 978-0-19-852824-1 – cited on pages 7, 9, 11, 17, 18, 19, and 21.

[27] R. Gross and A. Marx. *Festkörperphysik*. De Gruyter Studium. De Gruyter, Berlin, 3. auflage edition (2018) – cited on pages 5, 13, 15, 35, 37, and 53.

[28] R. E. Hummel. *Electronic Properties of Materials*. Springer Berlin Heidelberg (2001). doi: 10.1007/978-3-642-86538-1 – cited on page 6.

[29] J. R. Chelikowsky and M. L. Cohen. *Nonlocal pseudopotential calculations for the electronic structure of eleven diamond and zinc-blende semiconductors*. Physical Review B 14 (2): 556–582 (1976). doi: 10.1103/physrevb.14.556 – cited on page 7.

[30] H. M. Knötig. *Interband cascade lasers and detectors: From active region design to devices*. Ph.d. thesis, TU Wien, Institute of Solid State Electronics (2022) – cited on page 9.

[31] H. Detz. *Epitaxy of InGaAs/GaAsSb heterostructures for intersubband optoelectronics*. Ph.d. thesis, TU Wien, Institute of Solid State Electronics (2011) – cited on pages 10 and 54.

[32] G. Bauer. *Optical characterization of epitaxial semiconductor layers*. Springer, Berlin [u.a.] (1996) – cited on pages 11, 63, 64, 65, 66, 67, 68, and 69.

[33] J. Singh. *Electronic and optoelectronic properties of semiconductor structures*. Cambridge University Press (2007) – cited on pages 12, 19, 20, 35, and 36.

[34] H. Lüth. *Surfaces and interfaces of solid materials*. Springer science & business media (1998) – cited on pages 13, 14, and 15.

[35] W. Mönch. *Semiconductor surfaces and interfaces*. Springer, Berlin [u.a.], 3., rev. ed., softcover version edition (2013) – cited on pages 13, 14, 15, and 53.

[36] R. Ferreira and G. Bastard. *Evaluation of some scattering times for electrons in unbiased and biased single- and multiple-quantum-well structures*. Physical Review B 40 (2): 1074–1086 (1989). doi: 10.1103/physrevb.40.1074 – cited on pages 19 and 21.

[37] P. Harrison and A. Valavanis. *Quantum wells, wires and dots: theoretical and computational physics of semiconductor nanostructures.* John Wiley & Sons (2016) – cited on page 21.

[38] C. Deutsch, H. Detz, M. Krall, M. Brandstetter, T. Zederbauer, A. M. Andrews, W. Schrenk, G. Strasser and K. Unterrainer. *Dopant migration effects in terahertz quantum cascade lasers.* Applied Physics Letters 102 (20): 201102 (2013). doi: 10.1063/1.4805040 – cited on pages 21 and 43.

[39] J. Faist, F. Capasso, C. Sirtori, D. L. Sivco, A. L. Hutchinson, S. N. G. Chu and A. Y. Cho. *Narrowing of the intersubband electroluminescent spectrum in coupled-quantum-well heterostructures.* Applied physics letters 65 (1): 94–96 (1994) – cited on page 21.

[40] G. Bastard. *Energy levels and alloy scattering in InP-In GaAs heterojunctions.* Applied Physics Letters 43 (6): 591–593 (1983). doi: 10.1063/1.94435 – cited on page 21.

[41] A. Bismuto, R. Terazzi, M. Beck and J. Faist. *Influence of the growth temperature on the performances of strain-balanced quantum cascade lasers.* Applied Physics Letters 98 (9) (2011) – cited on page 22.

[42] L. Esaki and R. Tsu. *Superlattice and negative differential conductivity in semiconductors.* IBM Journal of Research and Development 14 (1): 61–65 (1970). doi: 10.1147/rd.141.0061 – cited on page 22.

[43] J. Feldmann, K. Leo, J. Shah, D. A. B. Miller, J. E. Cunningham, T. Meier, G. von Plessen, A. Schulze, P. Thomas and S. Schmitt-Rink. *Optical investigation of bloch oscillations in a semiconductor superlattice.* Physical Review B 46 (11): 7252–7255 (1992). doi: 10.1103/physrevb.46.7252 – cited on page 22.

[44] M. Helm, W. Hilber, G. Strasser, R. D. Meester, F. M. Peeters and A. Wacker. *Continuum wannier-stark ladders strongly coupled by zener resonances in semiconductor superlattices.* Physical Review Letters 82 (15): 3120–3123 (1999). doi: 10.1103/physrevlett.82.3120 – cited on pages 22 and 101.

[45] M. Patra, G. Schwarz and E. Schöll. *Bifurcation analysis of stationary and oscillating domains in semiconductor superlattices with doping fluctuations.* Physical Review B 57 (3): 1824–1833 (1998). doi: 10.1103/physrevb.57.1824 – cited on pages 22 and 106.

[46] L. Esaki and L. L. Chang. *New transport phenomenon in a semiconductor "superlattice"*. Physical Review Letters 33 (8): 495–498 (1974). doi: 10.1103/PhysRevLett.33.495 – cited on pages 22 and 106.

[47] L. L. Bonilla and H. T. Grahn. *Non-linear dynamics of semiconductor superlattices*. Reports on Progress in Physics 68 (3): 577–683 (2005). doi: 10.1088/0034-4885/68/3/r03 – cited on pages 22, 23, and 101.

[48] A. Sibille, J. Palmier, M. Hadjazi, H. Wang, G. Etemadi, E. Dutisseuil and F. Mollot. *Limits of semiclassical transport in narrow miniband GaAs/AlAs superlattices*. Superlattices and Microstructures 13 (2): 247 (1993). doi: 10.1006/spmi.1993.1049 – cited on pages 22 and 102.

[49] A. Wacker and A.-P. Jauho. *Quantum transport: The link between standard approaches in superlattices.* Physical Review Letters 80 (2): 369–372 (1998). doi: 10.1103/physrevlett.80.369 – cited on page 23.

[50] R. Tsu and G. Döhler. *Hopping conduction in a "superlattice"*. Physical Review B 12 (2): 680–686 (1975). doi: 10.1103/physrevb.12.680 – cited on page 23.

[51] A. Carpio, L. L. Bonilla, A. Wacker and E. Schöll. *Wave fronts may move upstream in semiconductor superlattices.* Physical Review E 61 (5): 4866–4876 (2000). doi: 10.1103/physreve.61.4866 – cited on page 23.

[52] J. Kastrup, H. T. Grahn, K. Ploog, F. Prengel, A. Wacker and E. Schöll. *Multistability of the current-voltage characteristics in doped GaAs-AlAs superlattices.* Applied Physics Letters 65 (14): 1808–1810 (1994). doi: 10.1063/1.112850 – cited on pages 24 and 118.

[53] L. H. Li, L. Chen, J. R. Freeman, M. Salih, P. Dean, A. G. Davies and E. H. Linfield. *Multi-watt high-power THz frequency quantum cascade lasers.* Electronics Letters 53 (12): 799–800 (2017). doi: 10.1049/el.2017.0662 – cited on page 24.

[54] M. Jaidl. *Towards broadband terahertz quantum cascade ring laser frequency combs.* Ph.d. thesis, TU Wien, Photonics Institute (2022) – cited on page 25.

[55] B. Williams. *Terahertz quantum-cascade lasers.* Nat Photonics 1 (9): 517–515 (2007). doi: 10.1038/nphoton.2007.166 – cited on page 24.

[56] D. Hofstetter, F. Giorgetta, E. Baumann, Q. Yang, C. Manz and K. Köhler. *Mid-infrared quantum cascade detectors for applications in spectroscopy and*

pyrometry. Applied Physics B: Lasers and Optics 100 (2): 313–320 (2010). doi: 10.1007/s00340-010-3965-2 – cited on page 24.

[57] J. Hillbrand, L. M. Krüger, S. Dal Cin, H. Knötig, J. Heidrich, A. M. Andrews, G. Strasser, U. Keller and B. Schwarz. *High-speed quantum cascade detector characterized with a mid-infrared femtosecond oscillator.* Optics Express 29 (4): 5774–5781 (2021) – cited on pages 24 and 30.

[58] H. Schneider and H. C. Liu. *Quantum Well Infrared Photodetectors.* Springer Berlin Heidelberg (2006). doi: 10.1007/978-3-540-36324-8 – cited on pages 26, 27, and 31.

[59] G. A. Reider. *Photonik : Eine Einführung in die Grundlagen.* Springer Berlin Heidelberg Imprint: Springer Vieweg, Berlin Heidelberg, 4th ed. edition (2022) – cited on page 29.

[60] D. Hofstetter, M. Beck and J. Faist. *Quantum-cascade-laser structures as photodetectors.* Applied Physics Letters 81 (15): 2683–2685 (2002) – cited on page 30.

[61] L. Gendron, M. Carras, A. Huynh, V. Ortiz, C. Koeniguer and V. Berger. *Quantum cascade photodetector.* Applied physics letters 85 (14): 2824–2826 (2004) – cited on page 30.

[62] A. Vardi, G. Bahir, F. Guillot, C. Bougerol, E. Monroy, S. E. Schacham, M. Tchernycheva and F. H. Julien. *Near infrared quantum cascade detector in GaN/AlGaN/AlN heterostructures.* Applied Physics Letters 92 (1): 011112 (2008). doi: 10.1063/1.2830704 – cited on page 30.

[63] S.-Q. Zhai, J.-Q. Liu, X.-J. Wang, N. Zhuo, F.-Q. Liu, Z.-G. Wang, X.-H. Liu, N. Li and W. Lu. *19 µm quantum cascade infrared photodetectors.* Applied Physics Letters 102 (19): 191120 (2013). doi: 10.1063/1.4807030 – cited on page 30.

[64] M. Krall, M. Martl, D. Bachmann, C. Deutsch, A. M. Andrews, W. Schrenk, G. Strasser and K. Unterrainer. *Coupled cavity terahertz quantum cascade lasers with integrated emission monitoring.* Optics Express 23 (3): 3581–3588 (2015). doi: 10.1364/OE.23.003581 – cited on page 30.

[65] A. Buffaz, M. Carras, L. Doyennette, A. Nedelcu, X. Marcadet and V. Berger. *Quantum cascade detectors for very long wave infrared detection.* Applied

Physics Letters 96 (17) (2010). doi: 10.1063/1.3409139. Cited by: 40 – cited on page 30.

[66] M. Graf, N. Hoyler, M. Giovannini, J. Faist and D. Hofstetter. *InP-based quantum cascade detectors in the mid-infrared.* Applied Physics Letters 88 (24) (2006). doi: 10.1063/1.2210088. Cited by: 73; All Open Access, Green Open Access – cited on page 30.

[67] A. P. Ravikumar, J. De Jesus, M. C. Tamargo and C. F. Gmachl. *High performance, room temperature, broadband II-VI quantum cascade detector.* Applied Physics Letters 107 (14): 061113 (2015). doi: 10.1063/1.4932538 – cited on page 30.

[68] A. Harrer, B. Schwarz, S. Schuler, P. Reininger, A. Wirthmüller, H. Detz, D. MacFarland, T. Zederbauer, A. M. Andrews, M. Rothermund, H. Oppermann, W. Schrenk and G. Strasser. *4.3 µm quantum cascade detector in pixel configuration.* Opt Express 24 (15): 17041 (2016). doi: 10.1364/OE.24.017041 – cited on pages 30, 73, 77, and 126.

[69] P. Reininger, B. Schwarz, A. Harrer, T. Zederbauer, H. Detz, A. M. Andrews, R. Gansch, W. Schrenk and G. Strasser. *Photonic crystal slab quantum cascade detector.* Applied Physics Letters 103 (24): 241103 (2013). doi: 10.1063/1.4846035 – cited on page 30.

[70] S.-Q. Zhai, J.-Q. Liu, F.-Q. Liu and Z.-G. Wang. *A normal incident quantum cascade detector enhanced by surface plasmons.* Applied Physics Letters 100 (18): 181104 (2012). doi: 10.1063/1.4710523 – cited on page 30.

[71] B. Schwarz, P. Reininger, A. Harrer, D. MacFarland, H. Detz, A. M. Andrews, W. Schrenk and G. Strasser. *The limit of quantum cascade detectors: A single period device.* Applied Physics Letters 111 (6): 061107 (2017). doi: 10.1063/1.4985711 – cited on page 30.

[72] A. Harrer, R. Szedlak, B. Schwarz, H. Moser, T. Zederbauer, D. MacFarland, H. Detz, A. M. Andrews, W. Schrenk, B. Lendl and G. Strasser. *Mid-infrared surface transmitting and detecting quantum cascade device for gas-sensing.* Scientific Reports 6: 21795 (2016). doi: 10.1038/srep21795 – cited on page 30.

[73] P. Dean, A. Valavanis, J. Keeley, K. Bertling, Y. L. Lim, R. Alhathlool, A. D. Burnett, L. H. Li, S. P. Khanna, D. Indjin, T. Taimre, A. D. Rakić, E. H. Linfield and A. G. Davies. *Terahertz imaging using quantum cascade lasers—*

a review of systems and applications. Journal of Physics D: Applied Physics 47 (37): 374008 (2014). doi: 10.1088/0022-3727/47/37/374008 – cited on page 30.

[74] P. D. Grant, S. R. Laframboise, R. Dudek, M. Graf, A. Bezinger and H. C. Liu. *Terahertz free space communications demonstration with quantum cascade laser and quantum well photodetector.* Electronics Letters 45 (18): 952–954 (2009). doi: 10.1049/el.2009.1586 – cited on page 30.

[75] D. Palaferri, Y. Todorov, A. Bigioli, A. Mottaghizadeh, D. Gacemi, A. Calabrese, A. Vasanelli, L. Li, A. G. Davies, E. H. Linfield, F. Kapsalidis, M. Beck, J. Faist and C. Sirtori. *Room-temperature nine-µm-wavelength photodetectors and GHz-frequency heterodyne receivers.* Nature 556 (7699): 85–88 (2018). doi: 10.1038/nature25790 – cited on page 30.

[76] N. H. Pinkowski, Y. Ding, C. L. Strand, R. K. Hanson, R. Horvath and M. Geiser. *Dual-comb spectroscopy for high-temperature reaction kinetics.* Measurement Science and Technology 31 (5): 055501 (2020). doi: 10.1088/1361-6501/ab6ecc – cited on page 30.

[77] G. Villares, A. Hugi, S. Blaser and J. Faist. *Dual-comb spectroscopy based on quantum-cascade-laser frequency combs.* Nature Communications 5: 5192 (2014). doi: 10.1038/ncomms6192 – cited on page 30.

[78] B. Schwarz, P. Reininger, H. Detz, T. Zederbauer, A. M. Andrews, S. Kalchmair, W. Schrenk, O. Baumgartner, H. Kosina and G. Strasser. *A bi-functional quantum cascade device for same-frequency lasing and detection.* Applied Physics Letters 101 (19): 191109 (2012). doi: 10.1063/1.4767128 – cited on page 30.

[79] A. P. Ravikumar, T. A. Garcia, J. D. Jesus, M. C. Tamargo and C. F. Gmachl. *High detectivity short-wavelength II-VI quantum cascade detector.* Applied Physics Letters 105 (6) (2014). doi: 10.1063/1.4893359 – cited on pages 31 and 74.

[80] P. Reininger, T. Zederbauer, B. Schwarz, H. Detz, D. MacFarland, A. M. Andrews, W. Schrenk and G. Strasser. *InAs/AlAsSb based quantum cascade detector.* Applied Physics Letters 107 (8): 081107 (2015). doi: 10.1063/1.4929501 – cited on pages 31 and 100.

[81] M. Giparakis, H. Knötig, H. Detz, M. Beiser, W. Schrenk, B. Schwarz, G. Strasser and A. M. Andrews. *2.7 µm quantum cascade detector: Above band*

gap energy intersubband detection. Applied Physics Letters 120 (7): 071104 (2022). doi: 10.1063/5.0076856 – cited on pages 31, 76, 77, 80, and 88.

[82] U. Keller, K. Li, M. Rodwell and D. Bloom. *Noise characterization of femtosecond fiber raman soliton lasers.* IEEE Journal of Quantum Electronics 25 (3): 280–288 (1989). doi: 10.1109/3.18541 – cited on page 31.

[83] X. Nie, H. Zhen, G. Huang, Y. Yin, S. Li, P. Chen, X. Zhou, Y. Mei and W. Lu. *Strongly polarized quantum well infrared photodetector with metallic cavity for narrowband wavelength selective detection.* Applied Physics Letters 116 (16): 161107 (2020). doi: 10.1063/5.0002012 – cited on page 31.

[84] S. Kalchmair, R. Gansch, S. I. Ahn, A. M. Andrews, H. Detz, T. Zederbauer, E. Mujagić, P. Reininger, G. Lasser, W. Schrenk and G. Strasser. *Detectivity enhancement in quantum well infrared photodetectors utilizing a photonic crystal slab resonator.* Opt Express 20 (5): 5622 (2012). doi: 10.1364/OE.20.005622 – cited on page 31.

[85] D. Z. Ting, A. Soibel, A. Khoshakhlagh, S. A. Keo, S. B. Rafol, A. M. Fisher, B. J. Pepper, E. M. Luong, C. J. Hill and S. D. Gunapala. *Advances in III-V semiconductor infrared absorbers and detectors.* Infrared Physics & Technology 97: 210–216 (2019). doi: https://doi.org/10.1016/j.infrared.2018.12.034 – cited on page 31.

[86] A. Dehzangi, R. McClintock, A. Haddadi, D. Wu, R. Chevallier and M. Razeghi. *Type–II superlattices base visible/extended short–wavelength infrared photodetectors with a bandstructure–engineered photo–generated carrier extractor.* Scientific Reports 9 (1): 5003 (2019). doi: 10.1038/s41598-019-41494-6 – cited on page 31.

[87] Z. Xie, J. Huang, X. Chai, Z. Deng, Y. Chen, Q. Lu, Z. Xu, J. Chen, Y. Zhou and B. Chen. *High-speed mid-wave infrared interband cascade photodetector at room temperature.* Opt Express 28 (24): 36915–36923 (2020). doi: 10.1364/OE.409868 – cited on page 31.

[88] A. Harrer. *Quantum cascade intersubband devices for mid-infrared sensing.* Ph.d. thesis, TU Wien, Institute of Solid State Electronics (2017) – cited on page 34.

[89] C. T. Foxon and B. A. Joyce. *Growth and characterization of semiconductors.* chapter 3, 35–64. Institute of Physics Publishing, 2 edition (1991) – cited on pages 38, 50, and 51.

[90] J. E. Ayers, T. Kujofsa, P. Rago and J. E. Raphael. *Heteroepitaxy of semiconductors : theory, growth, and characterization.* CRC Press, Boca Raton, second edition edition (2017) – cited on pages 40, 51, 53, 60, and 61.

[91] E. Kuramochi and Y. Takanashi. *Strain effects in InGaSb/AlGaSb quantum wells grown by molecular beam epitaxy.* Journal of Applied Physics 77 (11): 5706–5711 (1995). doi: 10.1063/1.359213 – cited on pages 41 and 75.

[92] A. Braun, K. M. Briggs and P. Böni. *Analytical solution to Matthews' and Blakeslee's critical dislocation formation thickness of epitaxially grown thin films.* Journal of crystal growth 241 (1-2): 231–234 (2002) – cited on page 42.

[93] T. Zederbauer. *Mixed group-V compound semiconductors for intersubband devices.* Ph.d. thesis, TU Wien, Institute of Solid State Electronics (2017) – cited on pages 42, 44, 54, and 71.

[94] E. F. Schubert. *Doping in III-V semiconductors.* MRS Online Proceedings Library (OPL) 340: 273 (1994). doi: 10.1557/PROC-340-273 – cited on pages 42, 43, 108, and 109.

[95] R. B. Beall, J. B. Clegg, J. Castagne, J. J. Harris, R. Murray and R. C. Newman. *Post-growth diffusion of si in delta -doped GaAs grown by MBE.* Semiconductor Science and Technology 4 (12): 1171–1175 (1989). doi: 10.1088/0268-1242/4/12/021 – cited on page 43.

[96] D. V. Lang, R. A. Logan and M. Jaros. *Trapping characteristics and a donor-complex (DX) model for the persistent-photoconductivity trapping center in Te-doped$Al_xGa_{1-x}As$.* Physical Review B 19 (2): 1015–1030 (1979). doi: 10.1103/physrevb.19.1015 – cited on page 43.

[97] E. F. Schubert and K. Ploog. *Shallow and deep donors in direct-gap n-type $Al_xGa_{1x}As$:Si grown by molecular-beam epitaxy.* Physical Review B 30 (12): 7021–7029 (1984). doi: 10.1103/physrevb.30.7021 – cited on page 43.

[98] R. J. Nelson. *Long-lifetime photoconductivity effect in n-type GaAlAs.* Applied Physics Letters 31 (5): 351–353 (1977). doi: 10.1063/1.89696 – cited on page 43.

[99] R. Farrow. *Molecular Beam Epitaxy: Applications to Key Materials.* Materials science and process technology series : Electronic materials and process technology. Elsevier Science (1995) – cited on pages 43, 45, 48, and 49.

[100] M. Herman and H. Sitter. *Molecular Beam Epitaxy: Fundamentals and Current Status.* Springer Series in Materials Science. Springer Berlin Heidelberg (2012) – cited on pages 45, 46, and 47.

[101] W. M. Haynes. *CRC handbook of chemistry and physics.* CRC press (2014) – cited on page 47.

[102] S. R. Johnson. *Semiconductor substrate temperature measurement by diffuse reflectance spectroscopy in molecular beam epitaxy.* Journal of Vacuum Science & Technology B: Microelectronics and Nanometer Structures 11 (3): 1007 (1993). doi: 10.1116/1.586857 – cited on page 48.

[103] D. J. Chadi. *Atomic structure of GaAs(100)-(2×1) and (2×4) reconstructed surfaces.* Journal of Vacuum Science & Technology A: Vacuum, Surfaces, and Films 5 (4): 834–837 (1987). doi: 10.1116/1.574366 – cited on page 54.

[104] Q. Xie, J. E. Van Nostrand, J. L. Brown and C. E. Stutz. *Arsenic for antimony exchange on GaSb, its impacts on surface morphology, and interface structure.* Journal of Applied Physics 86 (1): 329–337 (1999). doi: 10.1063/1.370733 – cited on page 54.

[105] M. Losurdo, P. Capezzuto, G. Bruno, A. S. Brown, T. Brown and G. May. *Fundamental reactions controlling anion exchange during mixed anion heterojunction formation: Chemistry of As-for-Sb and Sb-for-As exchange reactions.* Journal of Applied Physics 100 (1): 013531 (2006). doi: 10.1063/1.2216049 – cited on page 54.

[106] B. R. Bennett, W. J. Moore, M. J. Yang and B. V. Shanabrook. *Transport properties of Be- and Si-doped AlSb.* Journal of Applied Physics 87 (11): 7876–7879 (2000). doi: 10.1063/1.373470 – cited on page 56.

[107] H. Ye, L. Li, R. T. Hinkey, R. Q. Yang, T. D. Mishima, J. C. Keay, M. B. Santos and M. B. Johnson. *MBE growth optimization of InAs (001) homoepitaxy.* Journal of Vacuum Science & Technology B, Nanotechnology and Microelectronics: Materials, Processing, Measurement, and Phenomena 31 (3): 03C135 (2013). doi: 10.1116/1.4804397 – cited on page 56.

[108] G. Tuttle, H. Kroemer and J. H. English. *Effects of interface layer sequencing on the transport properties of InAs/AlSb quantum wells: Evidence for antisite donors at the InAs/AlSb interface.* Journal of Applied Physics 67 (6): 3032–3037 (1990). doi: 10.1063/1.345426 – cited on pages 57 and 89.

[109] J. Nicolaï, B. Warot-Fonrose, C. Gatel, R. Teissier, A. N. Baranov, C. Magen and A. Ponchet. *Formation of strained interfaces in AlSb/InAs multilayers grown by molecular beam epitaxy for quantum cascade lasers.* Journal of Applied Physics 118 (3): 035305 (2015). doi: 10.1063/1.4926786 –

[110] X. Marcadet, C. Becker, M. Garcia, I. Prévot, C. Renard and C. Sirtori. *Material engineering for InAs/GaSb/AlSb quantum cascade light emitting devices.* Journal of Crystal Growth 251 (1-4): 723–728 (2003). doi: 10.1016/s0022-0248(02)02319-9 – cited on page 57.

[111] B. R. Bennett, B. V. Shanabrook and E. R. Glaser. *Interface control in InAs/AlSb superlattices.* Applied Physics Letters 65 (5): 598–600 (1994). doi: 10.1063/1.112955 – cited on page 57.

[112] L. Tirado-Mejía, J. Villada, M. de los Ríos, J. Peñafiel, G. Fonthal, D. Espinosa-Arbeláez, H. Ariza-Calderón and M. Rodríguez-García. *Optical and structural characterization of GaSb and Te-doped GaSb single crystals.* Physica B: Condensed Matter 403 (21): 4027–4032 (2008). doi: https://doi.org/10.1016/j.physb.2008.07.049 – cited on page 59.

[113] A. Baraldi, C. Ghezzi, R. Magnanini, A. Parisini, L. Tarricone, A. Bosacchi, S. Franchi, V. Avanzini and P. Allegri. *Preparation of GaSb by molecular beam epitaxy and electrical and photoluminescence characterization.* Materials Science and Engineering: B 28 (1): 174–178 (1994). doi: https://doi.org/10.1016/0921-5107(94)90041-8 – cited on page 59.

[114] A. Bignazzi, A. Bosacchi and R. Magnanini. *Photoluminescence study of heavy doping effects in Te-doped GaSb.* Journal of Applied Physics 81 (11): 7540–7547 (1997). doi: 10.1063/1.365297 – cited on page 59.

[115] A. Ichimiya and P. I. Cohen. *Reflection high-energy electron diffraction.* Cambridge University Press, Cambridge (2004) – cited on pages 60 and 61.

[116] V. P. LaBella, M. R. Krause, Z. Ding and P. M. Thibado. *Arsenic-rich GaAs(0 0 1) surface structure.* Surface Science Reports 60 (1-4): 1–53 (2005). doi: 10.1016/j.surfrep.2005.10.001 – cited on page 62.

[117] C. Dupas and M. Lahmani. *Nanoscience: Nanotechnologies and nanophysics.* Springer Science & Business Media (2007) – cited on page 70.

[118] J. S. Smith, L. C. Chiu, S. Margalit, A. Yariv and A. Y. Cho. *A new infrared detector using electron emission from multiple quantum wells.* Journal of

Vacuum Science & Technology B: Microelectronics Processing and Phenomena 1 (2): 376–378 (1983). doi: 10.1116/1.582560 – cited on page 73.

[119] L. Chiu, J. Smith, S. Margalit, A. Yariv and A. Cho. *Application of internal photoemission from quantum-well and heterojunction superlattices to infrared photodetectors.* Infrared Physics 23 (2): 93–97 (1983). doi: 10.1016/0020-0891(83)90018-0 – cited on page 73.

[120] M. P. Semtsiv, M. Wienold, S. Dressler and W. T. Masselink. *Short-wavelength (λ= 3.3 μm) InP-based strain-compensated quantum-cascade laser.* Applied Physics Letters 89 (21): 211124 (2006). doi: 10.1063/1.2397020 – cited on pages 73 and 74.

[121] Özgür, Y. I. Alivov, C. Liu, A. Teke, M. A. Reshchikov, S. Doğan, V. Avrutin, S.-J. Cho and H. Morkoç. *A comprehensive review of ZnO materials and devices.* Journal of Applied Physics 98 (4): 041301 (2005). doi: 10.1063/1.1992666 – cited on page 74.

[122] M. Tchernycheva, L. Nevou, L. Doyennette, F. H. Julien, E. Warde, F. Guillot, E. Monroy, E. Bellet-Amalric, T. Remmele and M. Albrecht. *Systematic experimental and theoretical investigation of intersubband absorption InGaN/AlN quantum wells.* Physical Review B 73 (12): 125347 (2006). doi: 10.1103/physrevb.73.125347 – cited on page 74.

[123] A. Redondo-Cubero, A. Hierro, J.-M. Chauveau, K. Lorenz, G. Tabares, N. Franco, E. Alves and E. Muñoz. *Single phase a-plane MgZnO epilayers for UV optoelectronics: substitutional behaviour of Mg at large contents.* CrystEngComm 14 (5): 1637–1640 (2012). doi: 10.1039/c2ce06315h – cited on page 74.

[124] T. J. Anderson, M. J. Tadjer, J. K. Hite, J. D. Greenlee, A. D. Koehler, K. D. Hobart and F. J. Kub. *Effect of reduced extended defect density in MOCVD grown AlGaN/GaN HEMTs on native GaN substrates.* IEEE Electron Device Letters 37 (1): 28–30 (2016). doi: 10.1109/led.2015.2502221 – cited on page 74.

[125] F. R. Giorgetta, E. Baumann, D. Hofstetter, C. Manz, Q. Yang, K. Köhler and M. Graf. *InGaAs/AlAsSb quantum cascade detectors operating in the near infrared.* Applied Physics Letters 91 (11): 111115 (2007). doi: 10.1063/1.2784289 – cited on page 74.

[126] I. Vurgaftman, J. R. Meyer and L. R. Ram-Mohan. *Band parameters for III–V compound semiconductors and their alloys.* Journal of Applied Physics 89 (11): 5815–5875 (2001). doi: 10.1063/1.1368156 – cited on pages 74 and 126.

[127] M. P. Semtsiv, M. Wienold, S. Dressler and W. T. Masselink. *Short-wavelength (λ 3.05 μm) InP-based strain-compensated quantum-cascade laser.* Applied Physics Letters 90 (5): 051111 (2007). doi: 10.1063/1.2437108 – cited on page 74.

[128] P. Reininger. *Quantum cascade photodetectors: combining optical and electronic engineering.* Ph.d. thesis, TU Wien, Institute of Solid State Electronics (2015) – cited on pages 79 and 100.

[129] M. Motyka, M. Dyksik, K. Ryczko, R. Weih, M. Dallner, S. Höfling, M. Kamp, G. Sek and J. Misiewicz. *Type-II quantum wells with tensile-strained GaAsSb layers for interband cascade lasers with tailored valence band mixing.* Applied Physics Letters 108 (10): 101905 (2016). doi: 10.1063/1.4943193 – cited on page 95.

[130] L. Esaki and R. Tsu. *Superlattice and negative differential conductivity in semiconductors.* IBM Journal of Research and Development 14 (1): 61–65 (1970). doi: 10.1147/rd.141.0061 – cited on page 101.

[131] J. Feldmann, K. Leo, J. Shah, D. A. B. Miller, J. E. Cunningham, T. Meier, G. von Plessen, A. Schulze, P. Thomas and S. Schmitt-Rink. *Optical investigation of bloch oscillations in a semiconductor superlattice.* Physical Review B 46 (11): 7252–7255 (1992). doi: 10.1103/physrevb.46.7252 – cited on page 101.

[132] M. Giparakis, M. A. Kainz, M. C. Ertl, B. Limbacher, M. Jaidl, M. Beiser, S. Isceri, H. Detz, W. Schrenk, B. Schwarz, G. Strasser, G. Bastard, K. Unterrainer and A. M. Andrews. *Anomalous temperature effect in weakly-coupled superlattices - a glance into thz quantum cascade laser carrier transport.* Manuscript submitted for publication (2023) – cited on pages 101, 103, 104, 106, 107, 110, 112, 113, and 114.

[133] B. S. Williams, H. Callebaut, S. Kumar, Q. Hu and J. L. Reno. *3.4-THz quantum cascade laser based on longitudinal-optical-phonon scattering for depopulation.* Applied Physics Letters 82 (7): 1015–1017 (2003). doi: 10.1063/1.1554479 – cited on page 101.

[134] M. A. Kainz, S. Schönhuber, A. M. Andrews, H. Detz, B. Limbacher, G. Strasser and K. Unterrainer. *Barrier height tuning of THz quantum cascade lasers for*

high temperature operation. ACS Photonics 5 (11): 4687–4693 (2018). doi: 10.1021/acsphotonics.8b01280 – cited on page 102.

[135] A. N. Baranov, H. Nguyen-Van, Z. Loghmari, M. Bahriz and R. Teissier. *Terahertz quantum cascade laser with non-resonant extraction.* AIP Advances 9 (5): 055214 (2019). doi: 10.1063/1.5092855 –

[136] M. Franckié, L. Bosco, M. Beck, C. Bonzon, E. Mavrona, G. Scalari, A. Wacker and J. Faist. *Two-well quantum cascade laser optimization by non-equilibrium Green's function modelling.* Applied Physics Letters 112 (2): 021104 (2018). doi: 10.1063/1.5004640 – cited on page 102.

[137] M. Kainz, M. Semtsiv, G. Tsianos, S. Kurlov, W. Masselink, S. Schönhuber, H. Detz, W. Schrenk, K. Unterrainer, G. Strasser and A. Andrews. *Thermoelectric-cooled terahertz quantum cascade lasers.* Optics Express 27 (15): 20688–20693 (2019). doi: 10.1364/OE.27.020688 – cited on page 102.

[138] G. Brozak, M. Helm, F. DeRosa, C. H. Perry, M. Koza, R. Bhat and S. J. Allen. *Thermal saturation of band transport in a superlattice.* Physical Review Letters 64 (26): 3163–3166 (1990). doi: 10.1103/physrevlett.64.3163 – cited on page 102.

[139] F. Capasso, K. Mohammed and A. Y. Cho. *Sequential resonant tunneling through a multiquantum well superlattice.* Applied Physics Letters 48 (7): 478–480 (1986). doi: 10.1063/1.97007 – cited on page 102.

[140] C.-Y. Li, B.-Q. Sun, D.-S. Jiang and J.-N. Wang. *Analysis of the temperature-induced transition to current self-oscillations in doped GaAs/AlAs superlattices.* Semiconductor Science and Technology 16 (4): 239–242 (2001). doi: 10.1088/0268-1242/16/4/309 – cited on page 102.

[141] H. T. Grahn, R. J. Haug, W. Müller and K. Ploog. *Electric-field domains in semiconductor superlattices: A novel system for tunneling between 2D systems.* Physical Review Letters 67 (12): 1618–1621 (1991). doi: 10.1103/physrevlett.67.1618 – cited on pages 106 and 110.

[142] M. Rogozia, S. W. Teitsworth, H. T. Grahn and K. H. Ploog. *Relocation dynamics of domain boundaries in semiconductor superlattices.* Physical Review B 65 (20): 205303 (2002). doi: 10.1103/physrevb.65.205303 – cited on page 106.

[143] M. Rogozia, P. Krispin and H. T. Grahn. *Giant resistance changes in (Al,Ga)As contact layers of GaAs/AlAs superlattices due to deep donors.* Journal of

Applied Physics 90 (9): 4560–4564 (2001). doi: 10.1063/1.1407853 – cited on page 109.

[144] P. Greck, S. Birner, B. Huber and P. Vogl. *Efficient method for the calculation of dissipative quantum transport in quantum cascade lasers.* Optics Express 23 (5): 6587 (2015). doi: 10.1364/oe.23.006587 – cited on pages 115 and 116.

[145] M. Büttiker. *Role of quantum coherence in series resistors.* Physical Review B 33 (5): 3020–3026 (1986). doi: 10.1103/physrevb.33.3020 – cited on page 116.

[146] M. Büttiker. *Symmetry of electrical conduction.* IBM Journal of Research and Development 32 (3): 317–334 (1988). doi: 10.1147/rd.323.0317 – cited on page 116.

[147] S. Datta. *Nanoscale device modeling: the green's function method.* Superlattices and Microstructures 28 (4): 253–278 (2000). doi: 10.1006/spmi.2000.0920 – cited on page 116.

[148] P. Greck. *Efficient calculation of dissipative quantum transport properties in semiconductor nanostructures.* Ph.d. thesis, Technische Univ. Muenchen (2012) – cited on page 116.

Abbreviations

AFM   atomic force microscopy
CBO   conduction band offset
DM   double-metal
DX   donor-complex
EBL   electron beam lithography
FIB   focussed ion beam
FWHM   full width at half maximum
FTIR   Fourier-transform infrared spectrometer
ICP   inductively-coupled plasma
ISB   intersubband
I-V   current-voltage
LO   longitudinal optical
MBE   molecular beam epitaxy
MSB   multi-scattering Büttiker
NDR   negative differential resistance
NEGF   non-equilibrium Green's functions
PECVD   plasma enhanced chemical vapor deposition
QCD   quantum cascade detector
QCL   quantum cascade laser
QWIP   quantum well infrared photodetector
RHEED   reflection high energy electron diffraction
RMS   root mean square
RSM   reciprocal space map
RIE   reactive ion etching
SEM   scanning electron microscope
SL   superlattice
SMU   source meter unit
UHV   ultra high vacuum
HR-XRD   high-resolution X-ray diffraction

Journal publications

J1 M. Giparakis, B. Schwarz, W. Schrenk, S. Isceri, G. Strasser, A. M. Andrews; GaSb-based quantum cascade detectors. in preparation (2023)

J2 M. Giparakis, M. A. Kainz, M. C. Ertl, B. Limbacher, M. Jaidl, M. Beiser, S. Isceri, H. Detz, W. Schrenk, B. Schwarz, G. Strasser, G. Bastard, K. Unterrainer, A. M. Andrews; Anomalous temperature effect in weakly-coupled superlattices - a glance into THz quantum cascade laser carrier transport. submitted for publication (2023).

J3 A. Lalwani, M. Giparakis, K. Arora, A. Maharaj, A. Levy, G. Strasser, A. M. Andrews, H. Köck, D. G. Senesky; Effect of geometry on the frequency limit of GaAs/AlGaAs 2-Dimensional Electron Gas (2DEG) Hall effect sensors. arXiv:2306.07474 (2023). https://doi.org/10.48550/arXiv.2306.07474

J4 M. Jaidl, M. Beiser, M. Giparakis, M. Alexander Kainz, D. Theiner, B. Limbacher, M. C. Ertl, A. M. Andrews, G. Strasser, J. Darmo, K. Unterrainer; Ultrabroadband Heterogeneous THz Quantum Cascade Laser. ACS Photonics (2023) 10 (1), 111-115. https://doi.org/10.1021/acsphotonics.2c01202

J5 G. Marschick, M. David, E. Arigliani, N. Opačak, B. Schwarz, M. Giparakis, A. Delga, M. Lagree, T. Poletti, V. Trinite, A. Evirgen, B. Gerard, G. Ramer, R. Maulini, J. Butet, S. Blaser, A. M. Andrews, G. Strasser, and B. Hinkov; "High-responsivity operation of quantum cascade detectors at 9 μm," Opt. Express 30, 40188-40195 (2022). https://doi.org/10.1364/OE.470615

J6 L. Mennel, A. J. Molina-Mendoza, M. Paur, D. K. Polyushkin, D. Kwak, M. Giparakis, M. Beiser, A. M. Andrews, T. Mueller; A photosensor employing data-driven binning for ultrafast image recognition. Sci. Rep. 12, 14441 (2022). https://doi.org/10.1038/s41598-022-18821-5

J7 E. Bakali, W. Artner, M. Beiser, J. Bernardi, H. Detz, G. Eguchi, A. Foelske, M. Giparakis, C. Herzig, A. Limbeck, H. Nguyen, L. Prochaska, A. Prokofiev, M. Sauer, S. Schwarz, W. Schrenk, G. Strasser, R. Svagera, M. Taupin, A.S. Thirsfeld, M. Waas, X. Yan, D.A. Zocco, A.M. Andrews, S. Paschen; A Knudsen cell approach for the molecular beam epitaxy of the heavy fermion compound $YbRh_2Si_2$, J. Cryst. Growth 595 (2022) 126804, 0022-0248. https://doi.org/10.1016/j.jcrysgro.2022.126804.

J8 M. Giparakis, H. Knötig, H. Detz, M. Beiser, W. Schrenk, B. Schwarz, G. Strasser, A. M. Andrews; 2.7 µm quantum cascade detector: Above band gap energy intersubband detection. Appl. Phys. Lett. (2022); 120 (7): 071104. https://doi.org/10.1063/5.0076856

J9 M. Jaidl, N. Opačak, M. A. Kainz, D. Theiner, B. Limbacher, M. Beiser, M. Giparakis, A. M. Andrews, G. Strasser, B. Schwarz, J. Darmo, K. Unterrainer; Silicon integrated terahertz quantum cascade ring laser frequency comb. Appl. Phys. Lett. 28 February (2022); 120 (9): 091106. https://doi.org/10.1063/5.0078749

J10 M. Jaidl, N. Opačak, M. A. Kainz, S. Schönhuber, D. Theiner, B. Limbacher, M. Beiser, M. Giparakis, A. M. Andrews, G. Strasser, B. Schwarz, J. Darmo, and K. Unterrainer; Comb operation in terahertz quantum cascade ring lasers, Optica 8, 780-787 (2021). https://doi.org/10.1364/OPTICA.420674

Oral talks

O1 M. Giparakis, S. Isceri, W. Schrenk, B. Schwarz, G. Strasser, and A.M. Andrews; InAs/AlSb Quantum Cascade Detectors Strain-Balanced to GaSb substrates, IEEE Rapid, Miramar Beach, Florida, USA, Sept 11–13, 2023

O2 M. Giparakis, M. A. Kainz, M. C. Ertl, B. Limbacher, M. Jaidl, M. Beiser, S. Isceri, H. Detz, W. Schrenk, B. Schwarz, G. Strasser, G. Bastard, K. Unterrainer, A. M. Andrews; Anomalous temperature dependency of current-voltage curves in low-doped weakly-coupled superlattices, The International "Infrared and Terahertz quantum workshop" (ITQW), Erice, Italy, Jun 25–30 2023

O3 M. Jaidl, N. Opačak, D. Theiner, M. Ertl, B. Limbacher, M. Beiser, M. Giparakis, A.M. Andrews, G. Strasser, B.Schwarz, K. Unterrainer; Terahertz quantum cascade ring lasers: comb operation and integration on Si-substrates, Photonics West, San Francisco, USA, Jan 28–Feb 2, 2023

O4 M. Giparakis, H. Knoetig, S. Isceri, M. Beiser, H. Detz, W. Schrenk, B. Schwarz, G. Strasser, A.M. Andrews; MBE Growth and Characterization of an $InAs/AlAs_{0.16}Sb_{0.84}$ quantum cascade detector at $2.7\,\mu m$, North American Conference on Molecular Beam Epitaxy (NAMBE), Reheboth Beach, USA, Sep 18–22, 2022

O5 M. Giparakis, H. Knoetig, M. Beiser, H. Detz, B. Schwarz, W. Schrenk, G. Strasser, A.M. Andrews; Short-Wavelength InAs-based Quantum Cascade Detector Operating at $2.7\,\mu m$, IEEE Rapid, Miramar Beach, USA, Sep 12–14, 2022

O6 M. Jaidl, N. Opačak, M. A. Kainz, D. Theiner, B. Limbacher, M. Beiser, M. Giparakis, A. M. Andrews, G. Strasser, B. Schwarz, J. Darmo, and K. Unterrainer. Silicon Integrated Terahertz Quantum Cascade Ring Laser Frequency Comb. 47th 138 International Conference on Infrared, Millimeter and Terahertz Waves (IRMMWTHz), pages 1–1, Delft, Netherlands, Aug 28– Sept 2, 2022

O7 M. Jaidl, N. Opačak, M.A. Kainz, D. Theiner, B. Limbacher, M. Beiser, M. Giparakis, A.M. Andrews, G. Strasser, B. Schwarz, J. Darmo, K. Unterrainer; Silicon Integrated Terahertz Quantum Cascade Ring Laser Frequency Comb, IQCLSW2022, Zürich Monte Verita, Switzerland, Aug 23–28, 2022

O8 M. Ertl, M. Jaidl, B. Limbacher, D. Theiner, M. Kainz, M. Giparakis, M. Beiser, A.M. Andrews, G. Strasser, J. Darmo, K. Unterrainer; Epi-down Bonded Quantum Cascade Patch Antenna Array Laser, 9th International Conference on Optical Terahertz Science and Technology (OTST 2022), Budapest, Hungary, Jun 19–24 2022

O9 M. Jaidl, N. Opačak, M. A. Kainz, D. Theiner, B. Limbacher, M. Beiser, M. Giparakis, A. M. Andrews, G. Strasser, B. Schwarz, J. Darmo, and K. Unterrainer. Silicon Integrated Terahertz Quantum Cascade Ring Laser Frequency Comb, [9th] International Conference on Optical Terahertz Science and Technology (OTST 2022), Budapest, Hungary, Jun 19–24 2022

O10 M. Giparakis, H. Knoetig, H. Detz, M. Beiser, W. Schrenk, B. Schwarz, G. Strasser, A.M. Andrews; Top-Side Illuminated InAS/AlAsSb Quantum Cascade

Detector at 2.7 μm, Conference on Lasers and Electro-Optics, San Jose, USA, May 15–20, 2022

O11 M. Jaidl, N. Opačak, M. A. Kainz, D. Theiner, B. Limbacher, M. Beiser, M. Giparakis, A. M. Andrews, G. Strasser, B. Schwarz, J. Darmo, and K. Unterrainer. Silicon Integrated Terahertz Quantum Cascade Ring Laser Frequency Comb, Conference on Lasers and Electro-Optics, San Jose, USA, May 15–20, 2022

O12 S. Isceri, M. Giparakis, E. Bakali, M. Beiser, H. Detz, W. Schrenk, G. Strasser, M. Waas, R. Svagera, S. Bühler-Paschen; Single crystal growth of $YbRh_2Si_2$, DGKK/DEMBE 2022, Bremen, Germany. May 16–18, 2022

O13 A.M. Andrews, M. Giparakis, H. Knötig, S. Isceri, M. Beiser, W. Schrenk, B. Schwarz, G. Strasser; Above band gap energy InAs/AlAsSb quantum cascade detector, Workshop on Compound Semiconductor Materials and Devices (WOCSEMMAD) 2022, Destin Beach, FL, USA, Feb 20–22, 2022

O14 M. Jaidl, N. Opačak, M. A. Kainz, S. Schönhuber, D. Theiner, B. Limbacher, M. Beiser, M. Giparakis, A. M. Andrews, G. Strasser, B. Schwarz, and J. Darmo. Comb Operation In Terahertz Quantum Cascade Ring Lasers. Joint Annual Meeting of the Austrian Physical Society & Swiss Physical Society, Innsbruck, Austria, Oct 30– Sept 3, 2021

O15 M. Beiser, M. Giparakis, H. Knötig, H. Detz, M. Giparakis, B. Schwarz, A.M. Andrews, G. Strasser; Strain Balancing for InAs Based ICL growth, MBE XXI, Mexico, ONLINE, Sep 6–9, 2021

O16 M. A. Kainz, M. Jaidl, B. Limbacher, D. Theiner, M. Giparakis, M. Beiser, A. M. Andrews, G. Strasser, and K. Unterrainer. Terahertz Amplifier with Optical Threshold. Conference on Lasers and Electro-Optics Europe and European Quantum Electronics Conference (2021), number cc 6 5, Virtual, Jun 20–24, 2021

O17 M. Jaidl, N. Opačak, M. A. Kainz, S. Schönhuber, D. Theiner, B. Limbacher, M. Beiser, M. Giparakis, A. M. Andrews, G. Strasser, B. Schwarz, J. Darmo, and K. Unterrainer. Comb Operation in Terahertz Quantum Cascade Ring Lasers. In Conference on Lasers and Electro-Optics Europe and European Quantum Electronics Conference (2021), number cc 8 2, Virtual, Jun 20–24, 2021

O18 M. Jaidl, N. Opačak, M. A. Kainz, S. Schönhuber, D. Theiner, B. Limbacher, M. Beiser, M. Giparakis, A. M. Andrews, G. Strasser, B. Schwarz, J. Darmo, and K. Unterrainer. Comb Formation In Ultrathin Terahertz Quantum Cascade Ring Lasers. In Conference on Lasers and Electro-Optics (2021), number JTh3A.78, Virtual, May 9–14, 2021

O19 M. Giparakis, M.A. Kainz, S. Schönhuber, B. Limbacher, H. Detz, M. Beiser, W. Schrenk, A.M. Andrews, G. Strasser, G. Bastard, K. Unterrainer; Selective Emission of a THz QCL using a Magnetic Field, DEMBE 2019, Würzburg, Germany, Oct 7–8, 2019

O20 M. A. Kainz, M. Jaidl, B. Limbacher, D. Theiner, M. Giparakis, M. Beiser, A. M. Andrews, G. Strasser, and K. Unterrainer. Terahertz Quantum Cascade Amplifier with Optical Threshold. Conference on Lasers and Electro-Optics (2021), number ATu2T.5, Virtual, Sept 15–20, 2019

O21 A.M. Andrews, M Kainz, S. Schönhuber, B. Limbacher, H. Detz, M. Beiser, M. Giparakis, W. Schrenk, G. Strasser, G. Bastard, K. Unterrainer; Laser Level Selection in Terahertz Quantum Cascade Lasers, IEEE RAPID, Miramar Beach, USA, Aug 19–21, 2019

O22 A.M. Andrews, M.A. Kainz, H. Detz, M. Beiser, M. Giparakis, W. Schrenk, S. Schönhuber, K. Unterrainer, and G. Strasser; Barrier Height selection for high temperature THz quantum cascade lasers, Euro MBE Workshop, Lenggries, Germany, Feb 18, 2019

Poster presentations

P1 S. Isceri, M. Giparakis, W. Schrenk, B. Schwarz, G. Strasser, A.M. Andrews; 4.3 µm InAs/AlSb Quantum Cascade Detector Strain-Balanced to a GaSb Substrate, North American Conference on Molecular Beam Epitaxy (NAMBE), Madison, Wisconsin, USA, Sept 17–20, 2023

P2 S. Isceri, M. Giparakis, M. Beiser, H. Detz, W. Schrenk, S. Bühler-Paschen, G. Strasser, A.M. Andrews; Epitaxy of $YbRh_2Si_2$ on $Ge(0\,0\,1)$", German MBE Workshop 2021, Göttingen, Germany, Oct 14–15, 2021

P3 M. Giparakis, H. Knötig, H. Detz, M. Beiser, B. Schwarz, W. Schrenk, G. Strasser, A.M. Andrews; Growth, design, and characterization of an

InAs/AlAsSb based QCD at 2.7 µm, German MBE Workshop, virtual, Oct 14–15, 2021

P4 M. C. Ertl, M. Jaidl, B. Limbacher, M. A. Kainz, D. Theiner, M. Beiser, M. Giparakis, A. M. Andrews, G. Strasser, J. Darmo, and K. Unterrainer. Epidown Bonded Quantum Cascade Patch Antenna Array Laser. Joint Annual Meeting of the Austrian Physical Society & Swiss Physical Society, Innsbruck, Austria, Oct 30– Sept 3, 2021

P5 M. Jaidl, N. Opacak, M. A. Kainz, S. Sch¨onhuber, D. Theiner, B. Limbacher, M. Beiser, M. Giparakis, A. M. Andrews, G. Strasser, B. Schwarz, and J. Darmo. Comb Operation In Terahertz Quantum Cascade Ring Lasers. Joint Annual Meeting of the Austrian Physical Society & Swiss Physical Society, Innsbruck, Austria, Oct 30– Sept 3, 2021

P6 M. Giparakis, H. Knötig, M. Beiser, H. Detz, W. Schrenk, B. Schwarz, G. Strasser, A. M. Andrews; InAs/AlAsSb-based quantum cascade detector at 2.7 µm, CLEO Europe & EQEC, virtual, Jun 21–25, 2021

P7 M. Giparakis, H. Knötig, M. Beiser, J. Hillbrand, H. Detz, W. Schrenk, B. Schwarz, G. Strasser, A. M. Andrews, 2.7 µm short-wavelength InAs/AlAsSb quantum cascade detector, International Quantum Cascade Laser School & Workshop (IQCLSW), virtual, Sep 7–10, 2020

P8 M. A. Kainz, M. Jaidl, S. Schönhuber, D. Theiner, M. P. Semtsiv, S. Kurlov, W.T. Masselink, M. Beiser, M. Giparakis, H. Detz, G. Strasser, K. Unterrainer, and A. M. Andrews. Thermoelectrically Cooled THz Quantum Cascade Lasers, 21st International Winterschool Mauterndorf 2020, pages 100–101, Mauterndorf, Austria, Feb 23–28, 2020

P9 M. Giparakis, M. Kainz, M. Beiser, K. Unterrainer, G. Strasser, and A. M. Andrews. Investigation of the optimum phonon depopulation energy separation in a GaAs/AlGaAs superlatice, 21st International Winterschool Mauterndorf 2020, pages 100–101, Mauterndorf, Austria, Feb 23–28, 2020

P10 M. Jaidl, M. A. Kainz, S. Sch¨onhuber, D. Theiner, A. M. Andrews, M. Beiser, M. Giparakis, G. Strasser, J. Darmo, and K. Unterrainer. Multimode Emission from a THz Quantum Cascade Ring Laser. 21st International Winterschool Mauterndorf 2020, pages 100–101, Mauterndorf, Austria, Feb 23–28, 2020

MIRIAM GIPARAKIS

EDUCATION

Doctoral program in Electrical Engineering, TU Wien *02/2019 – present*

- University/Project Assistant at the Institute of Solid State Electronics, TU Wien
- Molecular beam epitaxy (MBE) growth of III-V heterostructures
- Design and simulations related to quantum cascade detectors and -lasers
- Cleanroom fabrication and characterization of optoelectronic devices
- 8 journal- , 22 oral presentation -, 10 poster presentation contributions
- Teaching assistant: Bachelor course - Semiconductor physics
- MBE maintenance experience

Dipl.-Ing. (equiv. MSc.) in Technical Physics, TU Wien *02/2016 – 01/2019*

- Master thesis: "Development of a Modular Cylindrical Magnetron System and Design of a DC Magnetron Sputtering Device for Coating Inner Surfaces of Narrow Tubes", at the Institute of Solid State Physics, TU Wien
- Project work A: "Catalytic hydrolysis of Sodium borohydride utilizing catalyst-coated hollow micro glass-spheres"
- Project work B: "$Ce_3Pd_{20}Ge_6$: Single crystal growth and resistivity measurements"

BSc. in Technical Physics, TU Wien *10/2012 – 02/2016*

- Bachelor thesis: "Annealing behavior of thin ZrO_2 films on Pt(111) studied by STM, XPS and LEED", at the Institute of Solid State Physics, TU Wien

Matura - High-school graduation *18.06.2012*

- field of attention: foreign languages